Experimental studies of quantum contextuality and non locality on an NMR quantum information processor

Dileep Singh

A thesis submitted for the partial fulfillment of
the degree of Doctor of Philosophy

Department of Physical Sciences
Indian Institute of Science Education & Research Mohali
Knowledge city, Sector 81, SAS Nagar, Manauli PO, Mohali 140306, Punjab, India

March 2023

Declaration

The work presented in this thesis has been carried out by me under the guidance of Prof. Kavita Dorai and Prof. Arvind at the Indian Institute of Science Education and Research Mohali.

This work has not been submitted in part or in full for a degree, diploma or a fellowship to any other University or Institute. Whenever contributions of others are involved, every effort has been made to indicate this clearly, with due acknowledgement of collaborative research and discussions. This thesis is a bonafide record of original work done by me and all sources listed within have been detailed in the bibliography.

Dileep Singh

Place :
Date :

In my capacity as supervisor / co-supervisor of the candidate's PhD thesis work, I certify that the above statements by the candidate are true to the best of my knowledge.

Prof. Arvind
(Co- supervisor)
Professor
Department of Physical Sciences
IISER Mohali

Place :
Date :

Prof. Kavita Dorai
(Supervisor)
Professor
Department of Physical Sciences
IISER Mohali

Place :
Date :

Acknowledgements

First and foremost, praises and thanks to God, for His blessings, so that I have been finally able to accomplish the thesis.

I would like to express my profound gratitude to my thesis supervisor Prof. Kavita Dorai and Prof. Arvind for their relentless support, encouragement, and academic and moral steering throughout the course of my Ph.D. This thesis would not have been possible without their help and support, for which I will always be thankful to them.

I would also like to thank my doctoral committee members, Dr. Abhishek Chaudhury and Dr. Samir Kumar Biswas for their valuable suggestions during this journey. I would like to acknowledge the faculties of the Department of Physical Sciences of IISER Mohali for providing their excellent knowledge, innovative ideas, and all the discussions during my coursework.

This journey would not even have begun without the support of my father Krishna Kumar Singh, my mother Meena Singh, my elder brother Kuldeep Singh, my elder sister Soni Singh and my younger brother Digvijay Singh. I also like the other family members, my sister-in-law Renu Singh and my brother-in-law Sushil Singh. Thanks to my wonderful niece and nephew Akriti Singh and Arpit Singh for keeping the positivity alive. Even though they do not grasp the field that I work in yet stand by me and they are the backbone of all the work that I have accomplished.

I thank my wife, Kirti Singh for brightening up my every day just like the sun lights up the earth. She has been the battle buddy during the thesis work and her presence brings out the best in me. I would also like to thank her parents G.B.Singh, Hemlata Singh, and her sisters Rashmi Singh and Shikha Singh for their support during my Ph.D. work.

I am thankful to all the members of the NMR research group, who have been like my extended family of mine: Dr. Rakesh Sharma, Jyotsana Ojha, Sumit Mishra, Gaikwad Akshay Ramdas, Akanksha Gautam, Vaishali Gulati, Krishna Shinde, Gayatri Singh, and Arshdeep Singh. I would also like to acknowledge QCQI group lab members for their fruitful discussion: Dr. Jaskaran Singh, Rajendra Singh Bhati, Jorawar Singh, Dr. Chandan Kumar, and Kirpreet Singh Pannu. I am also thankful to my seniors Dr. Shurti Dogra, Dr. Harpteet Singh, Dr. Amandeep Singh, Dr. Satnam Singh, and Dr. Navdeep Gogna for their inspiration and fruitful discussion. I also acknowledge project student Omkar Bihani for his help in my research work and for being my partner in the badminton game.

I am very grateful to Mr. Balbir Singh for his technical as well as motivational advice during my thesis work. I also thank Mr. Aneesh (Bruker India), Dr B. S. Joshi (Bruker India) and Dr. Paramdip Singh Chandi for his technical support and guidance.

During my Ph.D., the experiments were performed on a 600 MHz Bruker NMR

spectrometer and I am very thankful for all the support provided by the NMR research facility, IISER Mohali to carry out my experimental work. I would like to acknowledge IISER Mohali for the research fellowship. Finally, I would also like to thank the Dean Academics and Dean R&D, and the directors of IISER Mohali.

Dileep Singh

Abstract

This thesis focuses on the experimental study of foundational concepts of quantum theory such as quantum contextuality, and nonlocality on an nuclear magnetic resonance (NMR) quantum information processor. Contextuality and nonlocality are crucial aspects of quantum mechanics, and their existence demonstrates the fundamental departure from the classical theories such as hidden variable theories. Nonlocality and quantum contextuality can be revealed via a violation of non-contextual inequalities such as the Klyachko-Can-Binicioglu-Shumovski (KCBS) inequality and Bell-type inequalities such as the Clauser-Horne-Shimony-Holt (CHSH) inequality, respectively. These fundamental ideas have emerged as a crucial tool for enhancing computation and establishing secure quantum communications. Monogamy relationships can be used to examine quantum contextuality and nonlocality simultaneously. Numerous quantum information tasks, such as secure communication, self-testing, and randomness certification, have found extensive use for monogamy of correlations.

One of the major areas of focus in experimental quantum computing is the experimental study of the above quantum correlations. This thesis aims to conduct an experimental study of quantum contextual correlations, nonlocal correlations, and monogamous relationships of these quantum correlations on an NMR quantum information processor. Different types of experimental schemes, suitable for the NMR experimental set-up, have been developed that enable the precise measurement of the relevant observables. Experimental demonstration of fully contextual quantum correlations has been successfully experimentally demonstrated on two-qubit and three-qubit states. A generalized quantum scattering circuit is presented which can be used to perform a non-invasive measurement. Further, Peres-Mermin (PM) inequality is successfully experimentally demonstrated on a three-qubit system. The monogamy relationship between contextuality and nonlocality has been successfully demonstrated on a ququart-qubit system using three NMR qubits. The theoretical protocol has also been developed to evaluate monogamy relationships of entropic non-contextuality (ENC) inequalities, and the theoretical results have been verified experimentally. Finally, experimental implementation of variational quantum algorithms is employed to predict the molecular ground-state energy of the H_2 molecule.

0. Abstract

The content of this thesis has been divided into eight chapters as described below:

Chapter 1

This chapter contains the introduction to quantum computation followed by the basics of NMR quantum processor. Further, this chapter introduces the concepts of quantum contextuality and Bell nonlocality. The latter part describes the basics of variational quantum algorithms. In the end, some concluding remarks with goals and motivations for the work undertaken in this thesis.

Chapter 2

This chapter focuses on fully contextual correlations and their experimental implementations. The violation of two fully contextual inequalities is experimentally demonstrated utilizing two-qubit and three-qubit systems. To eliminate the necessity for quantum state tomography, the expectation values of the related observables have been measured by decomposing all of the observables in terms of Pauli operators. Additionally, the behavior of each inequality has been examined by rotating the underlying state. Results suggest that the violation of both inequalities follows a nonlinear pattern with respect to the rotation angle of the underlying state.

Chapter 3

This chapter describes the generalization of the quantum scattering circuit, which is capable of performing non-invasive measurements. The quantum scattering circuits developed, can measure the n-point correlation function that is being measured sequentially without disturbing the outcome of subsequent measurements. On a three-qubit NMR quantum processor, the experimental violation of the PM inequality has been demonstrated using this quantum scattering circuit. The experimental violation of the Bell-type inequality is also demonstrated using a quantum scattering circuit.

Chapter 4

This chapter explains the experimental construction of a symmetric three-qubit entangled state, which is then utilized to violate the Bell-type inequality in the (3,2,2) scenario. Two distinct entanglement measures, namely negativity, and concurrence, are computed in order to confirm the presence of entanglement in the state. Also, a theoretical analysis is performed to show that the Bell type inequality can be used as a witness of entanglement.

Chapter 5

This chapter focuses on the experimental simulation of a monogamy relation between the contextuality and non-locality using a ququart-qubit system. Three NMR qubits are used to physically implement the ququart-qubit system, with the first two qubits combining to form a single ququart system. Additionally, it is shown experimentally that at a single point, the quantum boundary and the no-disturbance principle coincide.

Chapter 6

This chapter develops a theoretical framework for studying monogamous relationships of entropic non-contextuality (ENC) inequalities using a graph theoretic method. The monogamous relation between two ENC inequalities has been derived using the proposed theory in the context of the tripartite Bell-CHSH scenario. Further, the experimental validation of the theoretical work has been demonstrated. For both the pure state and the mixed state, the monogamy relation of the ENC inequalities has been determined.

Chapter 7

This chapter describes hybrid quantum-classical algorithms that can be used to compute the energy of molecules in their ground and excited states. The ground and the excited state energies of H_2 molecule are computed by using the variational quantum algorithms. The simulated results are then experimentally verified using a two-qubit system. Also, we developed the first simulation of the energy calculation of the H_2 molecule, which is reduced to a single qubit system, and experimentally verified the same.

Chapter 8

This chapter describes the conclusions of the thesis and some future directions.

List of Publications

1. **Dileep Singh**, Jaskaran Singh, Arvind, and Kavita Dorai, Monogamy relations of entropic non-contextual inequalities and their experimental realization. **arXiv**: 2201.02330 (2022). (Manuscript under review)

2. **Dileep Singh**, Vaishali Gulati, Arvind, and Kavita Dorai, Experimental construction of a symmetric three-qubit entangled state and its utility in testing the violation of a Bell inequality on an NMR quantum simulator. **arXiv**: 2206.12870 (2022). (Manuscript published in EPL)

3. **Dileep Singh**, Shashank Mehendale, Arvind, and Kavita Dorai, Experimental demonstration of ground and excited state energies of the H_2 molecule using VQE algorithm on an NMR quantum processor. (Manuscript under preparation).

4. **Dileep Singh**, Arvind, and Kavita Dorai, Experimental demonstration of the violation of the temporal Peres-Mermin inequality using contextual temporal correlations and noninvasive measurements. **Phys. Rev. A, 105**, 022216 (2022). doi:10.1103/PhysRevA.105.022216.

5. **Dileep Singh**, Arvind, and Kavita Dorai, Experimental simulation of a monogamy relation between quantum contextuality and nonlocality on an NMR quantum processor. **J. Magn. Reson.Open**,10-11,100058(2022). doi: https://doi.org/10.1016/j.jmro.2022.100058.

6. Amandeep Singh, **Dileep Singh**,Vaishali Gulati, Kavita Dorai and Arvind, Experimental detection of non-local correlations using a local measurement-based hierarchy on an NMR quantum processor. **Eur. Phys. J. D.**: 74(8), 168 (2020). doi:10.1140/epjd/e2020-10173-9.

7. **Dileep Singh**, Jaskaran Singh, Kavita Dorai and Arvind, Experimental demonstration of fully contextual quantum correlations on an NMR quantum information processor. **Phys. Rev. A, 100**, 022109 (2019). doi: 10.1103/PhysRevA.100.022109.

Contents

List of Figures

List of Tables

Chapter 1

Introduction

Quantum mechanics is the most successful quantitative theory ever invented. Quantum computers use the quantum properties of systems to perform computation. Technologies based on quantum information theories can perform better than classical ones in several key areas, including computation speed-up, secure communication, and quantum simulation [1]. Paul Benioff started the research area of quantum computing in 1980, by proposing the quantum mechanical model of the Turing machine [2]. At the same time, Richard Feynman was interested in the practicability of quantum computers and introduced the idea as to how quantum computers can be used in quantum simulation [3]. The first quantum algorithm was introduced by David Deutsch in 1985 [4], however, the main breakthrough came in 1994, when Peter Shor discovered a quantum algorithm having the capability of factorizing large numbers in polynomial time [5]. Another quantum algorithm, for search, was discovered by Lov Grover, the so-called Grover's search algorithm in 1996, capable of quadratic speed-up over an equivalent classical algorithm [6]. Tremendous growth has been seen in the field of quantum computation and quantum information over the years.

Quantum information processors take advantage of fundamentally novel models of computation based on quantum mechanical phenomena and can solve some problems much faster than classical computers [7, 8]. However, building a large-scale quantum computer is hampered by the enormous practical challenges in controlling quantum systems. Several systems are being utilized to implement small scale quantum processors and NMR has established itself as one of the successful platforms [8, 9, 10]. Novel NMR methods have successfully been applied to other quantum systems as well.

In this chapter, we will first introduce the basic concepts of quantum computing and quantum information theory and then the basic concepts of NMR quantum computing. In the end, we will introduce fundamental properties of quantum theory such as quantum contextuality and non-locality, that are dealt with in this thesis.

1.1 Quantum Computing and Quantum Information Processing

Quantum computing is an area of research where computation is performed using the quantum properties of physical systems [1, 8, 9]. One of the key features of quantum theory is superposition, which refers to the fact that a quantum system can exist in multiple states at the same time. To carry out particular computational operations, quantum computers make use of the superposition phenomenon, which can be substantially more efficient than classical computing. The most notable advantages of superposition can be witnessed in the search and factorization problems, where quantum algorithms employ the property of quantum superposition to execute computations polynomially and exponentially faster than classical computations. In order to find a specified item in a disordered list containing N elements, the quantum search algorithm, invented by Grover [6] is quadratically $O(\sqrt{N})$ faster than its classical counterpart. On the other hand, Peter Shor's factorization algorithm [5] is exponentially faster than the best classical algorithm. Entanglement is another important propery of quantum theory which can be utilized as a resourse to perform computational and cryptographic tasks that are impossible for classical systems [11, 12].

1.1.1 Qubits

In a classical computer, information is stored and processed using bits, which can either be '0' or '1'. It might be any system with two different and distinguishable choices, such as a light bulb that is either on or off. The bits are represented by the absence (0) or presence (1) of an electrical signal in classical computers.

A qubit (or quantum bit) is the quantum mechanical analogue of a classical bit. A qubit is a two-level quantum system, and its two basis states are typically expressed as $|0\rangle$ and $|1\rangle$. A qubit can exist in $|0\rangle$ or $|1\rangle$ states or it can also exist in superposition states (unlike classical bits). The general state of the qubit is defined as [1]:

$$|\psi\rangle = \alpha|0\rangle + \beta|1\rangle \tag{1.1}$$

where $|0\rangle$ and $|1\rangle$ represent two orthogonal basis states and $\{|0\rangle, |1\rangle\}$ is called the computational basis; α and β are complex numbers which obey the normalization condition, $|\alpha|^2 + |\beta|^2 = 1$.

The state of an N-qubit quantum register with the basis vectors of Hilbert space having dimension 2^N is given by:

$$|\psi\rangle = |\psi_1\rangle \otimes |\psi_2\rangle .... \otimes |\psi_N\rangle \tag{1.2}$$

where the state of the N-qubit quantum register is obtained by taking the tensor product of each individual qubit state.

The general state of the N-qubit quantum register can be rewritten as:

$$|\psi\rangle = \sum_{i=1}^{2^N} \alpha_i |\alpha_i\rangle \tag{1.3}$$

where $|\alpha_i\rangle$ denotes the N-qubit quantum register and $|\alpha_i|^2 = 1$.

1.1.2 Density matrix representation

Density matrix representation is used for the study of a large number or collection of systems called an ensemble. Consider a quantum system that has been prepared in the state $|\psi_1\rangle$ and we have n_1 such systems constituting a pure ensemble. Consider another ensemble made up of n_2 quantum systems, each of which is in the state $|\psi_2\rangle$. How does one describe the quantum state of the new ensemble if one mixes these two ensembles? What will happen if we now choose a quantum system from this ensemble and perform a measurement on it? If $N_T = n_1 + n_2$ is the total number of quantum systems then there exist two probabilities for the action: (i) The probability ($p_1 = \frac{n_1}{N_T}$, $p_2 = \frac{n_2}{N_T}$) with which the chosen quantum system can be either from ensemble $|\psi_1\rangle$ or $|\psi_2\rangle$, and (ii) probability with which, the chosen quantum system after measurement collapses to one of the basis states. It can be concluded that this situation does not fit the state description given in Eqn. 1.3.

The density operator [1, 9] for an ensemble is defined as:

$$\rho = \sum_i p_i |\psi_i\rangle\langle\psi_i| \tag{1.4}$$

where p_i is probability to be in the state $|\psi_i\rangle$ with $\sum_i p_i = 1$. For a pure ensemble i.e. all individuals belongs to the state $|\psi\rangle$, the density operator is defined as:

$$\rho = |\psi\rangle\langle\psi| \tag{1.5}$$

A density operator must meet the following requirements: (i) ρ must have positive eigenvalues, (ii) ρ must be hermitian i.e. $\rho^\dagger = \rho$, and (iii) Trace should be 1 i.e. $\mathrm{Tr}(\rho) = 1$. For a pure state $\mathrm{Tr}(\rho^2) = 1$, while $\mathrm{Tr}(\rho^2) < 1$ for a mixed state.

1.1.3 Quantum gates

In a classical computer, Boolean operations are performed via Boolean logic gates, such as AND, OR, NOT, NAND, and NOR gates. NAND and NOR gates are known as

the universal logic gates as any logic gate can be realized with the help of these gates. In a quantum computer, the manipulations of the quantum states are performed by quantum gates. Quantum gates are unitary operators $U(UU^\dagger = I)$ and are represented by unitary matrices corresponding to some basis. There exist a set of universal quantum gates in the sense that all unitary operations can be described via a set of quantum gates which consist of one-qubit quantum gates [U(2)] and the two-qubit exclusive-OR gate. Some important basic one and two-qubit quantum gates are given below:

Single-qubit gates

Pauli-X gate

The simplest possible single qubit gate is Pauli-X gate, also known as quantum NOT gate. It inverts the state of the logical qubit. The matrix representation of Pauli-X gate is given as:

$$X = \begin{bmatrix} 0 & 1 \\ 1 & 0 \end{bmatrix} \tag{1.6}$$

The action of Pauli-X gate on computational basis states ($|0\rangle$, $|1\rangle$) results in:

$$X|0\rangle = |1\rangle \quad \text{and} \quad X|1\rangle = |0\rangle \tag{1.7}$$

Pauli-Y gate and Pauli-Z gate

The matrix representation of Pauli-Y and Pauli-Z gates are given as:

$$Y = \begin{bmatrix} 0 & -1 \\ 1 & 0 \end{bmatrix} \qquad Z = \begin{bmatrix} 1 & 0 \\ 0 & -1 \end{bmatrix} \tag{1.8}$$

The action of Pauli-Y and Pauli-Z gates on computational basis states results in:

$$Y|0\rangle = i|1\rangle \quad \text{and} \quad Y|1\rangle = -i|0\rangle \tag{1.9}$$

$$Z|0\rangle = |0\rangle \quad \text{and} \quad Z|1\rangle = -|1\rangle \tag{1.10}$$

Hadamard gate

Another single-qubit quantum gate is the Hadamard gate (H) gate which can be decomposed as a linear combination of Pauli-X and Pauli-Z quantum gates. An important property of H gate is its self-reversibility i.e. $H^2 = 1$. The matrix representation

of H gate is

$$H = \frac{1}{\sqrt{2}} \begin{bmatrix} 1 & 1 \\ 1 & -1 \end{bmatrix} \tag{1.11}$$

The action of H gate is given by:

$$H|0\rangle = \frac{|0\rangle + |1\rangle}{\sqrt{2}} \quad \text{and} \quad H|1\rangle = \frac{|0\rangle - |1\rangle}{\sqrt{2}} \tag{1.12}$$

Two-qubit gates

Controlled-NOT gate

The controlled-NOT, also called CNOT gate is a very important two-qubit gate in quantum information processing. CNOT gate consists of a control and a target qubit and this gate performs the NOT operation on the computational basis state of the target qubit only when the control qubit is in the $|1\rangle$ state. The matrix form of the CNOT gate is:

$$\text{CNOT} = \begin{bmatrix} 1 & 0 & 0 & 0 \\ 0 & 1 & 0 & 0 \\ 0 & 0 & 0 & 1 \\ 0 & 0 & 1 & 0 \end{bmatrix} \tag{1.13}$$

It has been proved that an arbitrary two-level unitary operation on the state space of n qubits can be achieved with help of CNOT gates and single qubit gates [1].

1.1.4 Quantum measurements

To describe quantum measurements, a set of measurement operators $\{M_m\}$ are typically used, where the index m denotes the measurement results that could occur during the experiment. M_m are the operators acting on the state space. For a given state $|\psi\rangle$, the probability of getting the measurement outcome m, before the measurement, can be expressed as [1]:

$$p(m) = \langle\psi|M_m^\dagger M_m|\psi\rangle \tag{1.14}$$

After the measurement the state of the system is described as:

$$\frac{M_m|\psi\rangle}{\sqrt{\langle\psi|M_m^\dagger M_m|\psi\rangle}} \tag{1.15}$$

The condition that all measurement operators add to identity, often known as "The Completeness Condition", is an analogous representation of the sum of probabilities, or $\sum_m p(m) = 1$. The completeness condition is given as:

$$\sum_m M_m^\dagger M_m = \mathbb{I} \tag{1.16}$$

The simplest example of a measurement would be the measurement of a qubit in the computational basis. Consider the general state of a qubit $|\psi\rangle = \alpha|0\rangle + \beta|1\rangle$ and the measurement operators $M_0 = |0\rangle\langle 0|, M_1 = |1\rangle\langle 1|$ corresponding to two outcomes. It can be observed that each measurement operator is Hermitian and $M_0^2 = M_0$, $M_1^2 = M_1$. The completeness relation is: $I = M_0^\dagger M_0 + M_1^\dagger M_1 = M_0 + M_1$. After the application of measurement operators on the qubit state, the probability of getting measurement outcome 0, i.e $p(0)$, is given by:

$$p(0) = \langle\psi|M_0^\dagger M_0|\psi\rangle = \langle\psi|M_0|\psi\rangle = |\alpha|^2 \tag{1.17}$$

Similarly, $p(1)$ can be calculated as $p(1) = \langle\psi|M_1^\dagger M_1|\psi\rangle = \langle\psi|M_1|\psi\rangle = |\beta|^2$.
The post-measurement state in the two situations is given as:

$$\frac{M_0|\psi\rangle}{|\alpha|} = \frac{\alpha}{|\alpha|}|0\rangle \tag{1.18}$$

$$\frac{M_1|\psi\rangle}{|\beta|} = \frac{\beta}{|\beta|}|1\rangle \tag{1.19}$$

Projective measurements, a special class of quantum measurements, are typically involved in quantum computing and information. In projective measurements, a quantum state collapses to the eigenstate of the observable, being measured.

As discussed earlier, in quantum computing, quantum mechanical phenomena such as superposition and entanglement are employed to execute computations. Despite the mathematical conception of computational algorithms, the physical implementation of these algorithms requires a computer. In principle, classical computation can be modelled using circuits comprised of universal logic gates. Similarly, quantum computation can be processed via a quantum circuit that uses a variety of quantum gates. Specific standards have been established for the physical realization of quantum computation which are described in the next section.

1.1.5 Physical realization of quantum computation

With current technology, it is possible to build a system with a well-characterized qubit, but it is more difficult to build a system with an arbitrary number of well-characterized

qubits. The majority of quantum computation models require qubits which should be initialized in a well defined state before performing a computation. A collection of one and two-qubit gates can be used to build a universal quantum computer and decoherence times that are substantially longer than the typical gate time are preferred. The final measurement of any process that changes the quantum states of qubits is crucial for performing computations.

In 2000, David P. DiVincenzo presented the requirements for building a quantum computer, known as DiVincenzo criteria [13]. There are a total of seven requirements in the DiVincenzo criteria. The first five are primarily concerned with the machine's computational capabilities and other two concern information transmission via qubits. The first five criteria related to quantum computation are as follows:
1) A scalable physical system with a well-characterized qubit.
2) The ability to initialize the state of the qubits to a simple fiducial state.
3) Long relevant decoherence times.
4) A "universal" set of quantum gates.
5) A qubit-specific measurement capability.

Several quantum technologies have been tried for the physical implementation of a quantum information processor, although none of them totally meets the DiVincenzo requirement. A few physically implemented quantum processors are:

- Superconducting quantum computer: Qubits are realized by Josephson junctions [14, 15, 16].
- Optical quantum computer: Qubits are realized by different modes of light [17, 18, 19, 20, 21].
- Diamond-based quantum computer: Qubits are realized by nitrogen-vacancy centers in diamond [22, 23, 24].
- NMR quantum computers: Qubits are realized by nuclear spins [25, 26, 27, 28].
- Trapped ion quantum computer: Qubits are realized by trapped ions [29].

In this thesis, the NMR hardware is used as a quantum information processor.

1.2 Basics of NMR spectroscopy

NMR is one of the most established resonance techniques, along with ferromagnetic resonance and electron spin resonance. NMR has numerous applications in the fields

of materials science, petrophysics, biological, chemical, and physical sciences [9, 30]. NMR phenomena involves the study of the absorption of radio frequency waves by nuclei, subjected to a high static magnetic field [31]. A concise summary of fundamental principles of NMR with a focus on those that are important for quantum computing are described below.

1.2.1 Nuclear spins in a static magnetic field

For most nuclei with non-zero nuclear spin, the NMR phenomena can be observed where nuclear spin is the total angular momentum of the nuclei [9]. The nuclear spin operator is a vector operator, represented by $\hbar$ **I** with **I** denoting the total angular momentum of the nucleus. The atomic nuclei with non-zero nuclear spin possess a magnetic dipole moment and are related to spin angular momentum as:

$$\mu = \gamma_n \hbar \mathbf{I} \tag{1.20}$$

where the term γ_n refers to the gyromagnetic ratio, a characteristic of the nucleus. When an NMR sample is placed in a strong static magnetic field B_o (Fig. 1.1(a)), an interaction between the nuclear spins and the field occurs. The Hamiltonian describing the interaction between the spin and magnetic field is given by:

$$H = -\mu.\mathbf{B} = -\gamma_n \hbar \mathbf{I}.\mathbf{B} = -\gamma_n \hbar B_0 I_z = -\hbar \omega_n I_z \tag{1.21}$$

where I_z stands for the spin angular momentum's z-component and $\omega_n = -\gamma_n B_0$ is the frequency of precession of spins about the z-axis (Fig. 1.1(b)), known as Larmor frequency. All quantum operators operate in the subspace spanned by the magnetic quantum number $|m\rangle$ with $m = -I,\ -I+1, ..., 0, ...,\ I-1,\ I$, when the magnetic field B_0 is applied in the z-direction. The expectation values of the x and y component of the spin angular momentum i.e.$\langle I_x \rangle$ and $\langle I_y \rangle$, show oscillatory behavior with time, under the Hamiltonian. The eigenvalue of the above Hamiltonian (Eqn. 1.21) is given by:

$$E_m = -m\hbar\omega_n \tag{1.22}$$

With the energy gap of $\hbar\omega_n$, there exist equally spaced (2I + 1) energy levels where I denotes the nuclear spin. The population of each energy level is determined by the Boltzmann distribution for an ensemble of identical nuclei in thermal equilibrium. Let us consider the two level system with $I = \frac{1}{2}$ and the population of the energy level $m = \frac{1}{2}$ is described by n_+ and similarly the population of the energy level $m = -\frac{1}{2}$ is

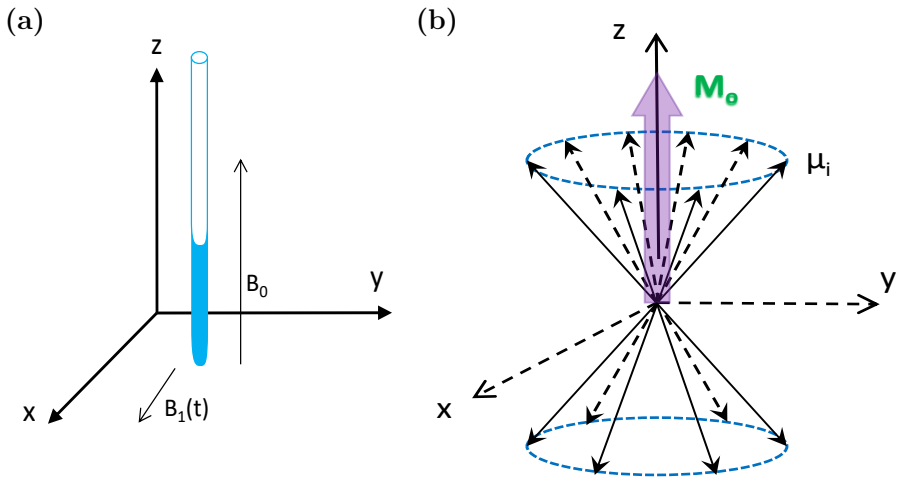

Figure 1.1: (a) Illustration of alignment of the NMR tube with sample inside. (b) Creation of bulk magnetisation M_0 when there are more spins precessing in the field's parallel direction than in its anti-parallel direction.

described by n_-. Then according to the Boltzmann distribution:

$$\frac{n_-}{n_+} = e^{-(E_{-I}-E_{+I})/k_BT} = e^{-\hbar\omega_n/k_BT} \tag{1.23}$$

where the Boltzmann constant is k_B, and the spin ensemble's absolute temperature is T. For the ensemble of protons (^{1}H) in the magnetic field of 14.1 Tesla at room temperature, the Boltzmann factor is close to the unity i.e. there exists a fractional difference of populations about 1 part in 10^5. This minor population difference leads to a net equilibrium magnetization in the z-direction (Fig. 1.1(b)) and the thermal equilibrium magnetization of n spin-1/2 nuclei is given by:

$$M_z = \frac{\mu_o \gamma^2 \hbar^2 B_o}{4k_BT} \tag{1.24}$$

where the magnetic susceptibility is represented by μ_o (and should not be confused with the magnetic moment μ).

1.2.2 Interaction of the nuclear spin with a radio frequency field

With a static magnetic field present, the unperturbed spin ensemble maintains its thermal equilibrium state. The application of oscillating magnetic fields at the suitable

Larmor frequency can produce transitions between the energy levels of spin states. For the strength of the static magnetic field of a few Tesla, the Larmor frequency is of the order of MHz, so to excite nuclear spins from their equilibrium state, a radiofrequency (RF) field is required. The excitation is achieved by applying the oscillating magnetic field, perpendicular to the static magnetic field which is given as:

$$\mathbf{B}_1(t) = 2B_1 \cos(\Omega t + \phi)\hat{x} \tag{1.25}$$

where $\hat{i}$ is the unit vector in the x-direction and Ω and ϕ are the RF field's frequency and phase, respectively. The RF field interaction Hamiltonian has the form:

$$H_{RF} = -\mu.\mathbf{B}_1(t) = -\gamma\hbar I_x[2B_1 \cos(\Omega t + \phi)] \tag{1.26}$$

When compared to the static magnetic field, the RF field's magnitude is relatively small; of the order of a few Gauss. As a result, the Hamiltonian corresponding to RF field (Eqn. 1.26) is considered as a perturbation to the interaction Hamiltonian (Eqn. 1.21). In the light of this, time-dependent perturbation theory can be used to examine the dynamics under H_{RF}. In order to understand the key features of the results, let us recast $\mathbf{B}_1(t)$ in terms of superposition of two fields rotating in the opposite directions.

$$\mathbf{B}_1(t) = B_1(\cos(\Omega t+\phi)\hat{x}+\sin(\Omega t+\phi)\hat{y})+B_1(\cos(\Omega t+\phi)\hat{x}-\sin(\Omega t+\phi)\hat{y}) \tag{1.27}$$

To make things simpler, we can assume that $\phi = 0$ and analyze Eqn. 1.27 in a coordinate system which revolves around the static magnetic field at the frequency Ω. Under this rotating frame, $\mathbf{B}_1(t)$ can be described as:

$$\mathbf{B}_1^{rot}(t) = B_1\hat{x} + B_1(\cos(2\Omega t)\hat{x} - \sin(2\Omega t)\hat{y}) \tag{1.28}$$

From the above Eqn. 1.28, one can conclude that one component is static and the other is rotating at twice the RF field frequency. The component rotating at twice the RF field frequency can be ignored because only the component corresponding to the static to the RF field frequency has an effect on nuclear spins. Utilizing the unitary operator $U(t) = e^{i\omega_n t I_z/\hbar}$, we can convert Hamiltonian H_{RF} into the rotating frame Hamiltonian, described as:

$$H_{RF}^{rot} = -\hbar(\omega_n - \Omega)I_z - \hbar\omega_1 I_x \tag{1.29}$$

with $\omega_1 = \gamma_n B_1$. Now if we consider ϕ is to be non-zero, then

$$H_{RF}^{rot} = -\hbar(\omega_n - \Omega)I_z - \hbar\omega_1\{I_x \cos(\phi) + I_y \sin(\phi)\} \tag{1.30}$$

The quantum ensemble's evolution in the rotating frame under the effective field is given by the following equation:

$$\rho_{rot}(t) = e^{-iH_{RF}^{rot}t}\rho_{rot}(0)e^{iH_{RF}^{rot}t} \tag{1.31}$$

with $\rho_{rot}(0)$ represents the density matrix at $t = 0$.

1.3 NMR quantum computing

NMR hardware was proposed as a promising possibility for quantum information processors at the end of the 20^{th} century [25, 32, 33]. The NMR quantum processor uses the spin ensemble of nuclear spins to do computations, whereas measurement results are expressed in terms of expectation values of the observables. NMR has been a test bed for various quantum algorithms and quantum information protocols. Quantum algorithms such as Grover's search algorithm [34], Shor's algorithm [35], Deutsch-Jozsa algorithm [26], and many more, have been experimentally demonstrated on an NMR quantum information processor.

The next subsections examine NMR's capabilities in light of the DiVincenzo criterion [13].

1.3.1 Qubit realization in NMR

As was previously mentioned, when atomic nuclei with non-vanishing nuclear spin are put in a static magnetic field, the nuclear energy spectrum composed of $(2I+1)$ equally spaced energy levels is produced. Each of these spin-1/2 nuclei is a two-level quantum system can be encoded as a qubit and $^{1}\mathrm{H}$, $^{13}\mathrm{C}$, $^{15}\mathrm{N}$, $^{19}\mathrm{F}$, and $^{31}\mathrm{P}$ are most used spin-1/2 nuclei in NMR quantum information processor [25, 26, 32, 33, 34, 35, 36].

The Hamiltonian H, corresponding to the ensemble of N spin-1/2 particles, placed in B_0, is given as:

$$H = -\omega_0 I_z \tag{1.32}$$

with $I_z = \sigma_z$. The eigenvalues of H are $\{\frac{\omega_0}{2}, -\frac{\omega_0}{2}\}$ corresponding to the eigenstate $\{|0\rangle|1\rangle\}$ and energy difference between the two energy levels is equal to $\hbar\omega_0$. A molecule may include more than one spin-1/2 nucleus. These spins can communicate directly through magnetic dipole-dipole interactions or indirectly through covalent bonds known as scalar-coupling (J-coupling). J-coupling involves the interaction of the nucleus with the electronic environment of the bonded electron cloud to the other nuclei while dipole-dipole interactions do not require a medium. Quantum computations frequently involve controlling the states of two different qubits. The J-coupling between the spins is crucial, as controlled operations can be easily accomplished through

evolution under coupling[9]. For the n weakly interacting spins-1/2 nuclei, the Hamiltonian is described as:

$$H = -\sum_{i=1}^{n} \hbar\omega^i I_z^i + \sum_{\substack{i,j=1 \\ i<j}}^{n} 2\pi\hbar J_{ij} I_z^i I_z^j \tag{1.33}$$

where ω^i is the Larmor frequency and J_{ij} denotes the scalar coupling constant between the i^{th} and j^{th} spins.

1.3.2 Initialization

The quantum register should be initialized in a pure state for any quantum information task. As was previously discussed, NMR deals with a large ensemble of nuclei that are in a mixed state. Cory et al. [25] and Chuang et al. [32] produced excellent techniques for producing the so-called effectively pure or pseudo pure states which can mimic actual pure states. Due to the fact that NMR experiments only detect deviation part of the density matrix, it is possible to establish the pseudo pure state (PPS). The concept of the PPS is based on the observation that NMR experiments are only sensitive to the traceless deviation density matrix. We could therefore look for transformations that, when applied to the density matrix at thermal equilibrium, resulting a deviation density matrix that has the same form as a pure state density matrix $|\psi\rangle\langle\psi|$.

The spin ensemble's thermal equilibrium state at temperature T and after the application of magnetic field B can be expressed as:

$$\rho_{th} = \frac{e^{-H/k_B T}}{\sum_m e^{-E_m/k_B T}} \tag{1.34}$$

At room temperature, the above thermal equilibrium state can be rewritable as:

$$\rho_{th} = \frac{1}{2I+1}\mathbb{I} + \frac{\Delta}{2I+1} I_z \tag{1.35}$$

with $\Delta = \frac{\hbar\omega}{k_B T} << 1 \approx 10^{-5}$ denotes a measure of thermal magnetization at temperature T in magnetic field B. The first term in Eqn. 1.35 corresponds to the identity operator $\mathbb{I}$ and the second term corresponds to the deviation part of thermal state I_z. Further, the PPS state can be achieved from the thermal state Eqn. 1.35, which can be written as:

$$\rho_{\text{PPS}} = \frac{(1-\Delta)}{2^n}\mathbb{I} + \frac{\Delta}{2^n}|\psi\rangle\langle\psi| \tag{1.36}$$

with $\frac{1}{2^n}$ representing the maximally mixed state and $|\psi\rangle$ denoting pure state. The term Δ corresponds to a measure of state's purity. In NMR experiments, only the

signal from the pure component is seen in NMR measurements because the maximally mixed state ($\frac{1}{2^n}$) is not detectable. Because of this, the behaviour of a pseudo-pure state behaves exactly like a pure state. However, the purity does affect the magnitude of the detectable signal, therefore pseudo-pure states would produce considerably smaller signals than pure states. The maximum pseudo-pure state signal obtained [37] from a system of n identical spins in thermal equilibrium has been demonstrated to be limited by the simple bound of

$$\frac{2\sinh(n\hbar\omega/2k_BT)}{2^n\cosh^n(n\hbar\omega/2k_BT}) \approx \frac{2}{2^n} \times \frac{\hbar\omega}{k_BT} \tag{1.37}$$

where the approximation holds at the high temperature limit, which is $\hbar\omega << k_BT$ and suitable for standard NMR experiments. The first term ($\frac{2}{2^n}$) of the result indicate that the detectable signal drops exponentially with the size of the spin system. This result seems to cap NMR quantum computing based on pseudo-pure states to about 10-20 qubits. A variety of methods exist for preparing PPS in NMR, including temporal averaging [38], spatial averaging [39], logical labelling [32], state initiation using long-lived singlet states [40], and NMR line-selective pulses [41]. It is well known that the NMR ensemble can be initiated in the PPS, replicating the behavior of the pure state.

1.3.3 Quantum gate implementation

This section contains the description of the physical realization of unitary gates on an NMR quantum processor. The NMR quantum gates can be generated via RF pulses and free evolution under the internal nuclear spin interactions. The deviation part of the thermal state is given by:

$$\Delta\rho_{th} = \frac{\hbar\omega}{4k_BT}\begin{bmatrix}1 & 0\\ 0 & -1\end{bmatrix} \tag{1.38}$$

By taking rotating frame considerations into account, the interactions of RF fields may be understood. It is possible to convert the rotating frame density operator ρ^{lab} into a rotating frame density operator which is given as:

$$\rho^{\text{rot}} = e^{-i\Omega tI_z}.\rho^{\text{lab}}.e^{i\Omega tI_z} \tag{1.39}$$

where $e^{-i\Omega tI_z}$ represents the rotation operator. In a rotating frame, the resulting effective Hamiltonian [9] can be expressed as:

$$H_{\text{eff}} = -\hbar(\omega - \Omega)I_z - \hbar\omega_1 I_x \tag{1.40}$$

When RF frequency $\omega_1 >> (\omega - \Omega)$ commonly known as nutation frequency, rotating frame Hamiltonian can be estimated as $H_{\text{eff}} \approx 1$ and for resonance condition

$\omega = \Omega$, $H_{\text{eff}} = 1$. The evolution operator for the RF pulse can be written down explicitly as

$$U_p = e^{-iH_{\text{eff}}t_p/\hbar} = e^{i\omega_1 t_p I_x} = R_x(-\theta_p) \tag{1.41}$$

where $R_x(-\theta_p)$ represents the rotation operator which is rotating about x-axis with an angle $-\theta_p$ governed by the RF irradiation period t_p. Explicit form of rotation operators that are achievable in NMR can be expressed as:

$$R_x(\theta_p) = \begin{bmatrix} cos\left(\frac{\theta_p}{2}\right) & -i\ sin\left(\frac{\theta_p}{2}\right) \\ -i\ sin\left(\frac{\theta_p}{2}\right) & cos\left(\frac{\theta_p}{2}\right) \end{bmatrix} \tag{1.42}$$

$$R_y(\theta_p) = \begin{bmatrix} cos\left(\frac{\theta_p}{2}\right) & sin\left(\frac{\theta_p}{2}\right) \\ -sin\left(\frac{\theta_p}{2}\right) & cos\left(\frac{\theta_p}{2}\right) \end{bmatrix} \tag{1.43}$$

$$R_{\phi_p}(\theta_p) = \begin{bmatrix} cos\left(\frac{\theta_p}{2}\right) & -i\ sin\left(\frac{\theta_p}{2}\right) e^{-i\phi_p} \\ -i\ sin\left(\frac{\theta_p}{2}\right) e^{i\phi_p} & cos\left(\frac{\theta_p}{2}\right) \end{bmatrix} \tag{1.44}$$

The final rotation operator corresponds to an RF pulse with phase ϕ_p with the rotating frame's x-axis. With the use of the aforementioned rotation operators, the resulting state after the action of H_{eff} (Eqn. 1.40) on deviation density operator (Eqn. 1.38) can be calculated. For example if consider $\omega_1 t_p = \theta_p = \frac{\pi}{2}$, then the action of rotation operator can be demonstrated as:

$$\Delta\rho(t_p) = R_x\left(-\frac{\pi}{2}\right).\Delta\rho_{th}.R_x\left(\frac{\pi}{2}\right) = \frac{\hbar\omega}{2k_BT}I_y \tag{1.45}$$

Using these rotation operator, any single qubit quantum gate can be generated. For instance, $R_y(\pi/2)$ produces the Hadamard(H)-gate effect, whereas $R_y(\pi)$ rotation produces the NOT (X) - gate effect. Utilizing the scalar J-couplings of the spins allows for the creation of two-qubit quantum gates such as CNOT gate. The following is the NMR pulse sequence of CNOT gate:

$$U_{\text{CNOT}} = R_z^1\left(-\frac{\pi}{2}\right) R_x^2\left(\frac{\pi}{2}\right) R_y^2\left(-\frac{\pi}{2}\right) \frac{1}{2J} R_y^2\left(\frac{\pi}{2}\right) \tag{1.46}$$

where the time span $1/2J$ describes the free evolution for spin systems.

1.3.4 NMR measurements

Reading out the result, which involves characterization of the final quantum state, is the last step in a quantum computation. Normally, reading out the results would be

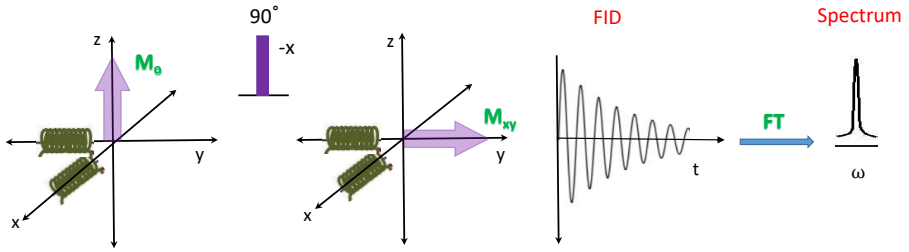

Figure 1.2: Illustration of scheme to detect the NMR signal where bulk magnetisation is brought in the xy plane with help of suitable RF field.

accomplished by the use of quantum measurements, which project the quantum state onto the measurement basis. The detection of the NMR signal is not a strong projective measurement, but rather a weak ensemble measurement, making this method unsuitable in standard NMR experiments. A weak ensemble measurement in an NMR experiment monitors the spin system's state without making any significant changes.

As described earlier, the NMR experiments deal with the ensemble of large nuclei, and when they are placed in a static magnetic field (B_0), the magnetic moments μ of the nuclei at thermal equilibrium produces a bulk magnetization (M_0) in the direction of the applied magnetic field (z - axis). By using an RF pulses, this developed bulk magnetization is rotated to xy-plane from z-axis. This rotated bulk magnetization process around the z-axis with the Larmor frequency ω_0. The precessing bulk magnetization causes a change in magnetic flux in the RF coil which in turn produces a signal voltage. The bulk magnetization's precession results in a change in magnetic flux, which leads to produce a signal voltage in the RF coil placed in xy-plane (Fig. 1.2). A time-domain NMR signal recorded and given the name "free induction decay" (FID) as shown in Fig. 1.2. Due to multiple NMR relaxation mechanisms, FID often decays with time. The transverse magnetization's time-domain signal can be described as:

$$S(t) \propto Tr\{\rho(t) \sum_k (\sigma_{kx} - i\sigma_{ky})\} \tag{1.47}$$

where $\sum_k (\sigma_{kx} - i\sigma_{ky})$ represents the detection operator, Pauli spin operators σ_{kx} and σ_{ky} corresponds to the x and y components of the magnetization caused by the k^{th} spin, and the average state of the single molecule is reprented by $\rho(t)$ [42]. The time-domain signal (Eqn. 1.47) can be transformed using the Fourier transform (FT) to produce the frequency-domain NMR signal.

Characterizing the output state is just as crucial to quantum information processing as creating the initial state and implementing quantum gates. In many instances, we want a full characterization of the system status rather than just a simple readout. This

can be done by computing each component of the density matrix of the system. We can calculate each element of the density matrix by using density matrix tomography, also referred to as quantum state tomography (QST). QST is a technique for reconstructing the density operator from different experimental settings [42, 43].

In a computational basis, any single-qubit density matrix [44] can be converted into the following form:

$$\rho = \frac{\mathbb{I}}{2} + a\sigma_x + b\sigma_y + c\sigma_z \tag{1.48}$$

which can again be rewritten as:

$$\rho = \begin{bmatrix} \frac{1}{2} - c & a - i\ b \\ a + i\ b & \frac{1}{2} + c \end{bmatrix} \tag{1.49}$$

It is possible to observe that $\langle \sigma_z \rangle_\rho = \mathrm{Tr}(\rho\sigma_z) = c$. Furthermore, by selecting the correct rotation operators, it is possible to measure the parameters a and b as well as to reconstruct the entire density operator ρ. In an NMR experiment, the signal is proportional to the transverse magnetisation i.e. $\rho_{12} = (a - i\ b)$ where the values of a and b can be estimated by measuring the intensities of real and imaginary parts of the NMR spectra, respectively. The value of c can be estimated by the measuring the real intensity of NMR spectra on the application of $\frac{\pi}{2}$ pulse along y direction.

Chuang et al. [45] developed the first NMR QST approach for coupled spin systems. It involves preparing the state to be tomographed and using RF pulses to carry out specific unitary rotations on the qubits. After that, the NMR readout spectrum is acquired, and the line intensities are computed. This process is repeated for various suitable RF pulses (tomographic pulses). After a specific number of readouts, a set of equations involving the line intensities and the components of the original density matrix can be constructed.

In NMR quantum computing, the Uhlmann-Jozsa relation is commonly used to compute the state fidelity [46, 47], given as:

$$F = \left[\mathrm{Tr}\left(\sqrt{\sqrt{\rho_{\mathrm{th}}}\rho_{\mathrm{ex}}\sqrt{\rho_{\mathrm{th}}}} \right) \right]^2 \tag{1.50}$$

where the theoretical and experimental density operators are denoted by the symbols ρ_{th} and ρ_{ex}, respectively.

1.4 Quantum Entanglement

Quantum entanglement is a key aspect of quantum theory and was first introduced in 1935 by Erwin Schrödinger [48]. It has been demonstrated that quantum entanglement is a physical resource [1] that can be used to conduct quantum computational operations [11] which cannot be carried out using classical resources.

Given a quantum system with two subsystems, A and B, whose quantum states are defined in Hilbert spaces $\mathcal{H}_A$ and $\mathcal{H}_B$ of dimension d_A and d_B, respectively, it is possible to express a vector in the joint Hilbert space $\mathcal{H}_A \otimes \mathcal{H}_B$ as [11]:

$$|\psi\rangle = \sum_{i,j=1}^{d_A,d_B} c_{ij}|a_i\rangle \otimes |b_i\rangle \quad \in \mathcal{H}_A \otimes \mathcal{H}_B \tag{1.51}$$

where $\{|a_i\rangle\}$ and $\{|b_i\rangle\}$ are the basis in $\mathcal{H}_A$ and $\mathcal{H}_B$, respectively, and $c_{ij} \in \mathbb{C}$. Normalization condition of $|\psi\rangle$ can be describes as $\sum_{i,j=1}^{d_A,d_B} |c_{ij}|^2 = 1$.

If $|\psi\rangle \in \mathcal{H}$ denotes a general pure state of the composite system AB, then it can be expressed as:

$$|\psi\rangle = |\phi^A\rangle \otimes |\phi^B\rangle \tag{1.52}$$

If $|\phi^A\rangle \in \mathcal{H}_A$, $|\phi^B\rangle \in \mathcal{H}_B$, then the state $|\psi\rangle$ is a separable or product state. If on the other hand, $|\psi\rangle$ cannot be written in the above separable form, it is said to be entangled.

Consider a more general scenario, where the system can be in any one of the states $|\phi_i\rangle \in \mathcal{H}$ having the probability p_i, a mixed state of the system can be written as

$$\rho = \sum_i p_i |\phi_i\rangle\langle\phi_i| \tag{1.53}$$

where $\sum_i p_i = 1$ and $p_i \geq 0$. If the state of the composite system can be written as a convex mixture, of the product states $\rho^A \otimes \rho^B$:

$$\rho = \sum_i w_i \rho_i^A \otimes \rho_i^B \tag{1.54}$$

then ρ is separable, otherwise it is entangled. These formulae for bipartite entanglement can also be generalized to multipartite situations.

It is essential to produce, identify, and protect entangled states as they are the one of the important resource of quantum information processing [49]. In quantum theory, characterising and detecting entanglement is typically a difficult problem. Significant experimental work has been put into creating entanglement in recent years. Several solutions to these problems have been proposed, including the positivity under partial transposition (PPT) [50] criterion, permutation-based estimates of quantum correlations [51], and others. It is also a well-established field to detect entanglements using entanglement witnesses [52]. Quantifying the entanglement in the state may be of relevance in addition to entanglement detection. There are various entanglement measures available to quantify the amount of entanglement present in the quantum state such as concurrence [53] and negativity [54]. More details are provided in Chapter 4.

1.5 Nonlocality and Quantum Contextuality

Since its inception, some aspects of quantum theory, including nonlocality [55, 56, 57], and quantum contextuality [58, 59, 60] have been subject to debate. These phenomena, despite their puzzling nature, enable some tasks that are either unfeasible or cannot be carried out as effectively using classical computer. It is widely established that the correlations corresponding to the measurements of quantum states contradict an interpretation based on classical theories. Results of measurements made on single indivisible systems or even spatially separated systems may show correlations that are higher than their apparent classical values. For bipartite space-like separated and for a single indivisible system, these correlations are referred to as Bell non-local or contextual, respectively. These correlations have been studied by means of inequalities and suggest non-classical behaviour when violated. To test the contextual nature of the correlations, the Klyachko, Can, Binicioğlu, and Shumovsky (KCBS) inequality [61], the simplest and well-studied inequality, is used while Clauser-Horne-Shimony-Holt (CHSH) inequality [62] is used to reveal the nonlocal nature of the correlations. Tasks involving the processing of quantum information [63, 64, 65] have greatly benefited from the use of the aforementioned quantum correlations. Also, a monogamy relationship between such quantum correlations has been developed [66, 67]. Utilizing a variety of quantum information processors, the experimental tests of quantum contextuality [68, 69], nonlocality [70], monogamy of nonlocality and contextuality [71] have been performed. Along with the previously described quantum properties, entanglement is a crucial aspect of quantum theory [11, 72, 73, 74, 75]. Entanglement is one of the essential components of nonlocality, and studies have looked into how the two are related [76].

In 1964, Bell inequality was developed to set bounds on classical situations describable by local realistic hidden variable models (LRHVM). Violation of the Bell inequality implies the inconsistency of LRHVM with quantum mechanics. The correlations which violate the inequality are termed as nonlocal. In 1967, Kochen and Specker provided an alternate method of determining intrinsic quantumness for the single quantum system and introduced the notion of quantum contextuality which is not compatible with noncontextual hidden variable (NCHV) theories.

1.5.1 Kochen-Specker theorem

Kochen-Specker (KS) theorem [58], one of the crucial concepts of quantum foundation theory was developed in 1967. According to the KS theorem, it is not always possible to pre-define the outcomes of the projective measurements in the Hilbert space of dimension 3 or greater. For a particular set of commuting projectors $\{\Pi_i\}$, with

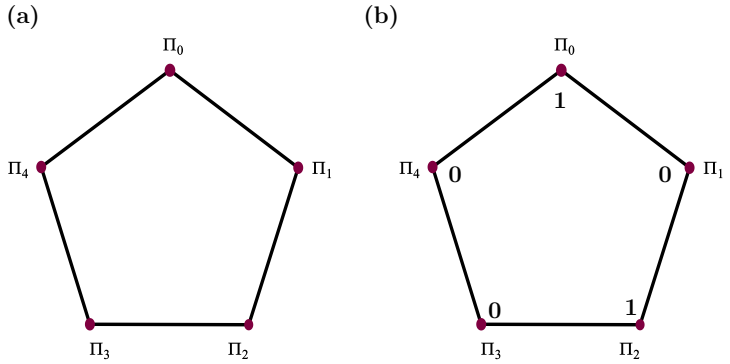

Figure 1.3: (a) Representation of orthogonality graph where each vertex corresponds to the projectors and each of the edge represents the orthogonality relationship between the two projectors. (b) Orthogonality graph, illustrating assignment of numerical values.

$\sum_i \Pi_i = 1$, it is impossible to associate the numerical values 0 or 1. Also, the sum of outcomes associated with the projectors must be equal to 1 i.e. $\sum_i v(\Pi_i) = 1$. It takes the utilization of 117 distinct projectors in a three-dimensional Hilbert space to prove the original KS theorem. The proof of the KS theorem involves the projectors having more than one contexts. It has been demonstrated that one can reach a contradiction of the non-contextuality hypothesis in which the assignment projectors' numerical values are independent of the context in which they appear.

1.5.2 Quantum contextual inequalities

As discussed in the previous section, the KS theorem describes the impossibility of assignment of definite outcomes to observables. The KS theorem can be viewed as a logical demonstration of contextuality and it is not suitable for implementation in the lab.

1.5.2.1 State dependent quantum contextuality: KCBS inequality

The first simplest scenario suitable for the experimental implementation was developed by Klyachko, Can, Binicioğlu, and Shumovsky and is known as KCBS scenario [61]. To test the KCBS inequality and reveal quantum contextuality, 3-dimensional Hilbert space system are required. The KCBS inequality involves five projectors and the scenario can be described via an orthogonality graph, depicted in Fig. 1.3(a).

In the orthogonality graph, the projectors are illustrated by the vertices, and an edge joins two orthogonal projectors. Projectors commute pairwise and are orthogonal

to one another. As a result, they can be evaluated together. A collection of such co-measurable observables represent the context. It can be concluded that context is defined by the edge and each projector is defined in two different contexts. According to the deterministic non-contextual model, the values 0 or 1 can be assigned to the vertex i with the probabilities P_i or $(1 - P_i)$. According to non-contextual assignment of numerical values, one can assign the probability $P_i = 1$ to maximum number of vertices is 2, regardless of the underlying state and one such possible assignment of numerical values are depicted in Fig. 1.3(b). The KCBS inequality can be described as:

$$K = \frac{1}{5}\sum_{0}^{4} P_i \leq \frac{2}{5} \tag{1.55}$$

where $\frac{2}{5}$ represents the maximum values that can be achieved via the non-contextual assignment of the numerical values. The KCBS inequality is an illustration of state-dependent contextuality that is satisfied by all noncontextual hypotheses. For the set projectors Π_i and for the particular state $|\psi\rangle$, the KCBS inequality can be violated. The maximum numerical value that can be achieved is $\frac{\sqrt{5}}{5}$ which is greater than $\frac{2}{5}$, showing that quantum theory does not allow the noncontextual hypothesis. These state-dependent scenarios exhibit violation depending on the observables and chosen quantum state .

1.5.2.2 State independent quantum contextuality

There exists another type of contextuality test, known as state-independent quantum contextuality [77, 78] where the inequality violation does not depend on the choice of states. Similar to state-dependent proofs, state-independent scenarios of contextuality can be constructed where each observable is a part of many contexts of commuting observables. One example of state-independent contextuality is the Peres-Mermin inequality [79] where the inequality is violated by any two-qubit quantum state for a particular set of nine observables.The observable set chosen is the "PM square" of nine dichotomous and mutually compatible observables $A, B, C, a, b, c, \alpha, \beta, \gamma$ [80]:

$$\begin{array}{lll} A = \sigma_z \otimes I, & B = I \otimes \sigma_z, & C = \sigma_z \otimes \sigma_z \\ a = I \otimes \sigma_x, & b = \sigma_x \otimes I, & c = \sigma_x \otimes \sigma_x \\ \alpha = \sigma_z \otimes \sigma_x, & \beta = \sigma_x \otimes \sigma_z, & \gamma = \sigma_y \otimes \sigma_y. \end{array} \tag{1.56}$$

Consider the expectation values of the above observable in certain combination described as follows:

$$\langle X_{\mathrm{PM}} \rangle = \langle ABC \rangle + \langle bca \rangle + \langle \gamma\alpha\beta \rangle + \langle A\alpha a \rangle + \langle bB\beta \rangle - \langle \gamma cC \rangle \tag{1.57}$$

The inequality values can be described as if we make non-contextual assignments:

$$\langle X_{\mathrm{PM}} \rangle \leq 4 \tag{1.58}$$

where the inequality known as Peres-Mermin inequality that is satisfied by all non contextual hidden variable (NCHV) theories [80] and violated by quantum theory. A value of $\langle X_{PM} \rangle = 6$ has been demonstrated for any four-dimensional quantum system with a certain set of observables, exhibiting state-independent contextuality [81].

1.5.3 Bell-CHSH inequality

The Bell's inequality [62] deals with nonlocal features which encompass the tensor products of systems in different Hilbert spaces. The existence of nonlocality is a fundamental departure from the classical theory. Einstein et al. [82] initially introduced the concept of nonlocality in 1935. They argued that the accuracy of the quantum mechanical description of reality should be examined. They constructed a scenario based on the assumptions of reality and locality for two spatially separated observers and demonstrated the paradoxical character of quantum theory [82].

According to John Bell's famous inequality in 1964 [55], at least one of the aforementioned premises must be false and has to be discarded. To establish the conventional interpretations of quantum theory, the concept of reality is typically abandoned. John Bell's findings, which are presented as a theorem, demonstrate that nature is intrinsically probabilistic and that no local realistic model can replicate it. More precisely, Bell's theorem states that any model based on local realism i.e. which assigns outcomes to measurements in a local manner can not reproduce the statistics of quantum theory. Based on this premise, the probability distribution of the measurements outcomes is given as:

$$p(a, b|A, B) = \int \mu(\lambda) p(a|A, \lambda) p(b|B, \lambda) d(\lambda) \tag{1.59}$$

where the outcomes of observables A and B are denoted by a and b, respectively and λ denotes the hidden variable, and $\mu(\lambda)$ denotes the hidden variable state probability. According to the local assumption, it is assumed that observables are measured on spatially distinct systems and hence cannot affect the outcomes of each other. According to Eqn. 1.59, given the probability distribution over the hidden variables λ, it is possible to factorise the joint probability distribution $p(a, b|A, B)$ into local distributions over the observables A and B. Several Bell inequalities that put limits on the behaviour of local hidden-variable models can be obtained using Eqn. 1.59.

The Bell-CHSH inequality is the most well-known and extensively studied Bell inequality. This inequality was developed for two parties, each having access to two mea-

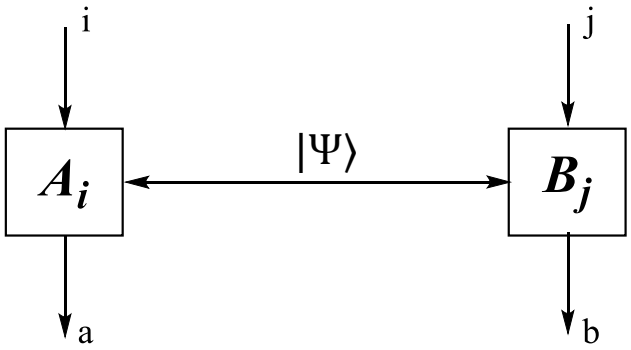

Figure 1.4: Schematic diagram corresponding to Bell CHSH inequality where A_i, B_i are the observables corresponding to Alice and Bob system, respectively, with $i, j \in \{0, 1\}$. The observables outcome are represented a, b with $a, b \in \{+1, -1\}$.

surement basis and each of the measurements being assumed to have two outcomes. The correlations that result from observations on two-qubit states are measured by the Bell-CHSH inequality. Nonlocal correlations are all those that violate the Bell-CHSH inequality.

Consider the two spatially separated parties Alice and Bob sharing an entangled state $|\psi\rangle$depicted in Fig 1.4. Each party can perform two measurements, each having ± 1 measurement outcomes . If A_0, A_1 and B_0, B_1 are the measurements performed on Alice's particle and on Bob's particle, respectively, a joint operator, referred to as the Bell operator, can be defined as:

$$\mathcal{B} = A_0 \otimes B_0 + A_0 \otimes B_1 + A_1 \otimes B_0 - A_1 \otimes B_1 \tag{1.60}$$

The expectation value of the above Bell operator $\mathcal{B}$ using any local realistic hidden variable model (LRHVM) is bounded between the 2 and -2, which is written as:

$$\langle S \rangle \equiv |\mathcal{B}| \leq 2. \tag{1.61}$$

In quantum theory, the violation of the above inequality can be achieved for some quantum states. The fact that some quantum states defy this bound suggests that there is no LRHVM for the above scenarios.

Major portion of the thesis is dedicated to the experimental study of quantum foundational properties such as quantum contextuality and non-locality. These two quantum phenomena were investigated separately for many years; however, it has recently been demonstrated that quantum contextuality and nonlocality can be examined simultaneously via the development of a monogamy relationship between them. This motivates us to move towards the experimental study of monogamy relationship between

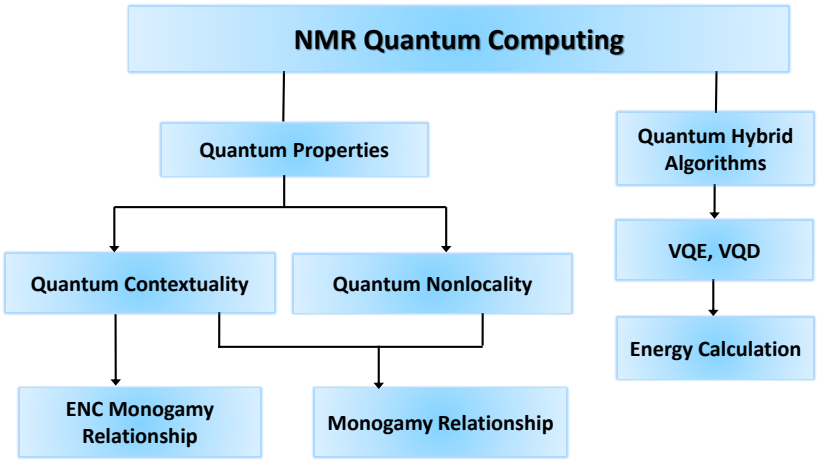

Figure 1.5: Graphical illustration of summary of contents of the thesis.

quantum contextuality and non-locality. Furthermore, we develop the novel method to derive the monogamy relation of entropic noncontextual inequalities and experimentally verified the developed theoretical results. Final part of the thesis contains the NMR implementation of quantum-classical hybrid algorithms, like variational quantum algorithms. We have simulated the ground state energy and excited state energies of H_2 molecule using the VQE and VQD algorithms respectively. The simulated results are then verified on an NMR quantum processor. The graphical representation of outline of this thesis is described in Fig. 1.5

1.6 Organization of the thesis

The work presented in this thesis focuses on the experimental exploration of key concepts of quantum theory such as quantum contextuality and non-locality. The thesis chapters are organized as follows:

Chapter 2 focuses on the experimental implementation of fully contextual correlations. Two different state-dependent quantum contextuality have been demonstrated using two and three NMR qubits. Section 2.1 introduces the notion of quantum contextuality. Section 2.2 describes the theoretical background of fully contextual correlations in four dimensional Hilbert space and their experimental demonstration is described in Section 2.3. Fully contextual correlations in eight-dimensional Hilbert space are described theoretically in Section 2.4, and their experimental demonstration is discussed in Section 2.5. Some concluding remarks of the chapter are presented in Section 2.6.

Chapter 3 provides the construction of a quantum scattering circuit capable of performing non-invasive measurements. We have utilized this circuit for the experimental demonstration of Peres-Mermin (PM) inequality as well as a Bell-type inequality using a three-qubit system. Section 3.1 introduces the notion quantum contextuality in temporal scenarios and non-invasive measurements. Section 3.2 describes the generalization of quantum scattering circuit capable of performing the non-invasive measurements. Section 3.3 describes the experimental demonstration of the violation of temporal Peres-Mermin and Bell-type inequalities using the three qubit quantum scattering circuit. Section 3.4 presents the chapter's concluding remarks.

Chapter 4 provides the experimental construction of a symmetric three-qubit entangled state, which is then utilized to violate a Bell-type inequality. Violation of the inequality reveals the maximal nonlocal nature of the scenario. Section 4.1 provides the description of tripartite entanglement states and its utility in tight Bell inequalities. Section 4.2 describes the theoretical background of the tight Bell inequality in the $(3, 2, 2)$ scenario. Section 4.3 provides the experimental construction of the three-qubit $|S\rangle$ entangled state and experimental demonstration of the violation of the tight Bell inequality, revealing the maximal nonlocality. The conclusions of the chapter are presented in Section 4.4.

Chapter 5 contains the experimental simulation of the monogamy relationship between non-locality and contextuality where a three-qubit system is used to realize the ququart-qubit system. Section 5.1 provides introduction of monogamy relationship between quantum contextuality and nonlocality. Section 5.2 contains the theoretical of monogamy relationship between quantum contextuality and nonlocality in ququart-qubit scenario and their experimental demonstration is presented in the Section 5.3. In Section 5.4, the chapter's conclusions are presented.

Chapter 6 uses a graph theoretical method based on the no-disturbance principle to present a theoretical analysis of the monogamous relation of entropic noncontextual (ENC) inequalities. Additionally, for pure and mixed states, we have experimentally verified the theoretical results. Section 6.1 introduces the notion of the monogamous relation of ENC inequalities. Section 6.2 describes the theoretical study of entropic inequalities and their monogamy relationship using the graph theoretical approach. Section 6.3 provides the experimental demonstration of monogamy relationship of ENC inequalities using the tripartite mixed and pure states. The chapter's conclusions are addressed in Section 6.4.

Chapter 7 contains an investigation of variational quantum eigensolver (VQE) and variational quantum deflation (VQD) algorithms to simulate the H_2 molecule's ground state and excited state energies. On an NMR quantum processor, the simulation findings are then validated. Section 7.1 provides the introduction of variational quantum algorithms and their applications in quantum chemistry. Section 7.2 contains the study

of simulation of energy calculation of H_2 molecules using the quantum hybrid (VQE, VQD) algorithms and their NMR implementation has been described in Section 7.3. Section 7.4 describes the study used to reduce the resources required for the ground state energy calculation of LiH molecule. Section 7.5 explains the chapter's conclusions.

Chapter 8 contains a summary of the thesis and future directions of work.

Chapter 2

NMR implementation of fully contextual quantum correlations

2.1 Introduction

The concept of the non-contextual hidden variable (NCHV) model was introduced by Specker and Kochen in 1967 and proposed that quantum theory is inconsistent with the NCHV model [56, 58]. This result is known as the Kochen-Specker (KS) theorem which states that the outcome measurements are independent of other compatible observables which are being measured simultaneously within the same measurement setting [60]. The context of measurements of other compatible observables within the same measurement environment have been shown to affect the measurement output, demonstrating the contextual nature of the quantum theory [59, 83, 84]. For composite systems, the Bell inequality can be used to test for quantumness, while noncontextual inequality can be used to show quantumness for single individual systems [61]. There are now several easier and more methodical methods of demonstrating quantum contextuality, especially those based on graph theory [85]. Using such approach several new scenarios of contextuality have been identified [77, 86, 87, 88].

Another area of scientific interest is finding the physical principles that underlie this kind of contextuality [89] and finding theories that are more contextual than quantum mechanics has been a major research focus [90, 91, 92]. It is crucial to pinpoint the basic contexts in which general theories cannot be more contextual than quantum theory. There exist scenarios in which it is possible that the maximum quantum values saturate the maximum for the general probability (GP) theories [68, 90].

Certain NC inequalities can be violated in order to reveal the contextuality, and Kochen and Specker developed the first NC inequality, known as the KS theorem [58]

and later, Peres suggested an updated version of the KS scheme [93]. The KS theorem, which was developed using counterfactual justification, is regarded as the logical proof of contextuality. As a result, implementing the KS scheme in the lab is unfeasible. The initial contextuality test suited for an experimental test was put forth by Klyachko, Can, Binicioğlu and Shumovsky, known as KCBS inequality [61]. Tests of contextuality can be classified as state-independent or state-dependent tests of contextuality. The contextuality can be revealed for every quantum state using the state independent tests [77, 94, 95], however the state-dependent tests can only reveal contextuality for specific quantum states [61, 96].

The KCBS inequality is an illustration of a state-dependent contextuality test, meaning that for a particular subset of quantum states, there is no joint probability distribution for the results of measurements. The KCBS inequality can violated by a set of five yes-no outcome observables on a three-level quantum system (qutrit). Utilizing single photons, the state-independent test of contextuality has been experimentally demontrated [97, 98]. Using four-dimensional photonic devices, the experimental demonstration of a KS set of the quantum yes-no test has been carried out [99]. There are further experimental studies that use photons to demonstrate quantum contextuality [68, 100]. Furthermore, contextuality is experimentally demontrated by verious groups using ions [101, 102], neutrons [103], and nuclear spins [69, 104].

In this chapter, we have used an NMR quantum processor to experimentally demonstrate fully contextual correlations. Two distinct inequalities are used to reveal fully contextual connections. The first inequality, contructed by Nagali et al. [68], utilizing ten projectors and ten measurements on a specific state in the four-dimensional Hilbert space. The second fully contextual inequality was proposed by Cabello [90] and known as twin KCBS inequality as it utilizes the same number of measurements as KCBS inequality. Twin KCBS inequality requires ten projectors and five measurements on a state in the six-dimensional Hilbert space. States in an eight-dimensional Hilbert space were used to realise the six-dimensional subspace. The graphical methodology for the experimental demonstration of the twin KCBS inequality is given in Fig. 2.1.

We first recast the inequalities to make them appropriate for NMR measurements in order to do the experimental demonstration. We decompose the projectors in terms of Pauli operators and map these decomposed Pauli operators into the single-qubit operator. The benefit of such mapping is that it does not require full state tomography, enables us to measure the required observables directly, and lowers the number of observables required to implement the inequalities. In NMR experiments, the two-qubit and three-qubit systems corresponding to four and eight-dimensional Hilbert spaces, are physically realised by ^{13}C-labeled chloroform and ^{13}C-labeled diethyl fluoromalonate molecules, respectively. Experimentally observed violations of the inequalities are in good agreement with theoretical prediction. Additionally, by introducing some

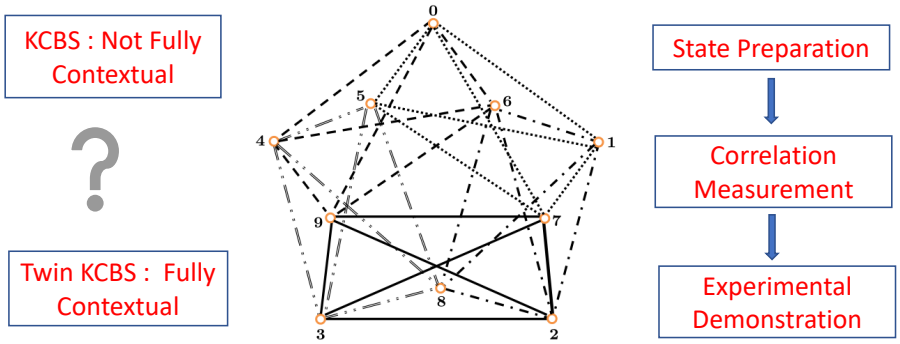

Figure 2.1: Scheme to experimentally demonstrate twin KCBS inequality which involves fully contextual correlations.

unitary rotation to the underlying quantum state, we studied how these inequalities behave for various quantum states. In relation to the rotation angle of the underlying state, the violation of both inequalities exhibits a nonlinear trend. Our findings indicate that fully contextual correlations in the eight-dimensional Hilbert space are more robust than those in the four-dimensional Hilbert space.

2.2 Fully contextual quantum correlations in four-dimensional Hilbert space

In this section, we will first look at a contextuality inequality that can reveal fully contextual quantum correlations as developed by Nagali et al. [68] which utilize states in a Hilbert space of dimension four. We present a modified version of the inequality by decomposition into Pauli matrices which we experimentally test on a four-level quantum system using two NMR qubits.

The simplest test of quantum contextuality requires measurement of 5 different projectors $\{\Pi_i\}$, $i \in \{0,1,2,3,4\}$ and $\Pi_i = |v_i\rangle\langle v_i|$, where $|v_i\rangle$ are unit vectors. The aforementioned projectors follow the exclusivity relation $P(\Pi_i = 1) + P(\Pi_{i\oplus 1} = 1) = 1$, where $P(\Pi_i = 1)$ represents the probability of obtaining outcome Π_i and addition is taken modulo 5. For projective measurements, this relationship implies that only one of Π_i or $\Pi_{i\oplus 1}$ can be obtained in a joint measurement of both. The corresponding test, termed as KCBS inequality is of the form

$$\mathcal{K} = \frac{1}{2}\sum_{i=0}^{4} P(\Pi_i + \Pi_{i\oplus 1} = 1) \overset{\text{NCHV}}{\leq} 2 \overset{\text{QM}}{\leq} \sqrt{5} \overset{\text{GP}}{\leq} \frac{5}{2}, \tag{2.1}$$

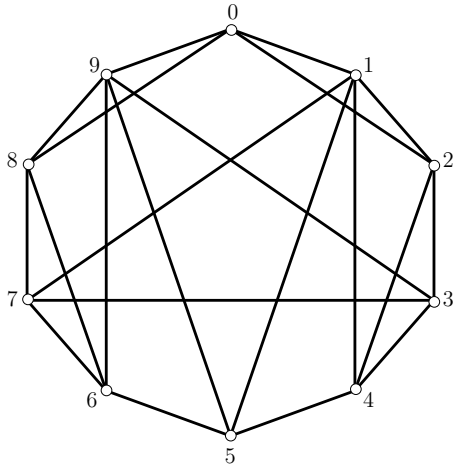

Figure 2.2: A ten-vertex orthogonality graph with the labels $0, 1, 2, ...9$ is used to depict the inequality $\mathcal{C}$. Each vertex represents a projector, and the orthogonal projectors are connected by an edge.

where the inequalities correspond to the maximum value achievable for non-contextual hidden variable (NCHV) theories, quantum mechanics (QM) and generalized probabilitic (GP) theories.

As is evident from Eqn. (2.1), the maximum violation that can be achieved in quantum mechanics is less than what can be attained if an underlying GP model is considered. Therefore, for the KCBS scenario, quantum correlations are not fully contextual. Recently, it has been shown that there exist tests of contextuality for which quantum correlations saturate the bound as imposed by GP models [105]. For these scenarios, quantum correlations are either non-contextual or fully contextual.

Fully contextual quantum correlations can also be obtained for scenarios other than KCBS as well. As shown in [68], one such scenario entails measurements corresponding to 10 different projectors $\Pi_j = |u_j\rangle\langle u_j|$, $j = \{0, 1, ..., 9\}$. In this particular scenario, the projectors follow exclusivity relationships as depicted in Fig. 2.2, where each vertex represents a projector Π_i and two projectors are connected by an edge if and only if they are exclusive. The corresponding test of contextuality is then given by the inequality,

$$\mathcal{C} = \sum_{i=0}^{9} P(\Pi_i = 1) \overset{\text{NCHV}}{\leq} 3 \overset{\text{QM, GP}}{\leq} \frac{7}{2}. \tag{2.2}$$

The scenario is reminiscent of the twin KCBS inequality as discussed above, however this test requires 10 different measurements rather than 5 and is capable of revealing fully contextual quantum correlations in a much smaller Hilbert space of dimension at least 4. The inequality can be explicitly tested if we consider the unit vectors $|u_i\rangle$ as

follows:

$$\langle u_0| = \frac{1}{\sqrt{2}}(0,0,1,1), \tag{2.3a}$$

$$\langle u_1| = \frac{1}{2}(1,-1,1,-1), \tag{2.3b}$$

$$\langle u_2| = \frac{1}{2}(1,-1,-1,1), \tag{2.3c}$$

$$\langle u_3| = \frac{1}{\sqrt{2}}(1,0,0,-1), \tag{2.3d}$$

$$\langle u_4| = \frac{1}{2}(1,1,1,1), \tag{2.3e}$$

$$\langle u_5| = \frac{1}{\sqrt{2}}(0,1,0,-1), \tag{2.3f}$$

$$\langle u_6| = \frac{1}{2}(-1,1,1,1), \tag{2.3g}$$

$$\langle u_7| = \frac{1}{\sqrt{2}}(1,0,0,1), \tag{2.3h}$$

$$\langle u_8| = \frac{1}{2}(1,1,1,-1), \tag{2.3i}$$

$$\langle u_9| = \frac{1}{2}(1,1,-1,1). \tag{2.3j}$$

The corresponding projective measurements are of the form

$$\mathcal{M}_j = \{\Pi_j, \mathbb{1} - \Pi_j\} \quad \forall j \in \{0,1,...,9\}, \tag{2.4}$$

which are performed on the state

$$\langle \phi| = (0,0,0,1). \tag{2.5}$$

To experimentally demontrate the inequality $\mathcal{C}$ on a four-level quantum system using two NMR qubits, one has to determine the expectation value of the observables involved for an experimentally prepared state. This can be achieved by decomposing the observables as a linear superposition of Pauli operators. For a two-qubit system, any observable can be decomposed as a linear superposition of 16 Pauli operators, and the Pauli operator can be mapped to the single-qubit Pauli Z operator. This mapping is particularly useful in the context of an NMR experimental setup where the expectation value of the Z operator is easily accessible. In an NMR measurement schema, the observed z magnetization of a nuclear spin in a particular quantum state is proportional to the expectation value of the Z operator of the spin in that state. The time-domain NMR

signal, i.e., the free-induction decay with an appropriate phase, results in Lorentzian peaks when Fourier transformed. These normalized experimental intensities give an estimate of the expectation value of Z in that quantum state [106, 107].

For the experimental implementation of the inequality, we decompose the projectors (Π_j) in terms of Pauli operators $\{I, X, Y, Z\}$. The inequality Eqn. (2.2) can be rewritten in terms of expectation values as:

$$\mathcal{C} = \sum_{i=0}^{9} \langle \Pi_i \rangle = \sum_{i=0}^{9} tr(\Pi_i \rho') \tag{2.6}$$

where $\rho' = |\phi\rangle\langle\phi|$. Using Eqn. 2.2, Eqn. 2.7 the inequality $\mathcal{C}$ can be rewritten as:

$$\mathcal{C} = \frac{1}{4} tr(B \cdot \rho') \overset{\text{NCHV}}{\leq} 3 \overset{\text{QM, GP}}{\leq} \frac{7}{2}, \tag{2.7}$$

where

$$B = XX + YY - ZI + 2ZZ - IZ + 10II \tag{2.8}$$

which can be measured experimentally. For example if we want to determine the expectation value $\langle XX \rangle$ in the state $\rho = |\psi\rangle\langle\psi|$, we map the state ρ to $\rho_1 = U_1.\rho.U_1^\dagger$ with $U_1 = \mathrm{CNOT}_{12}\, Y_2 Y_1$, followed by observing $\langle Z_2 \rangle$ for the state ρ_1. The expectation value $\langle Z_2 \rangle$ for the state ρ_1 is equivalent to the expectation value of $\langle XX \rangle$ in the state $\rho = |\psi\rangle\langle\psi|$. Table 2.1 details the mapping of Pauli basis operators (used in this paper) to the single-qubit Z operator. The observables of interest are given in the decomposition of Eqn. 2.8. By experimentally evaluating the expectation value of the observables given in Eqn. 2.8, the value of $\mathcal{C}$ can be estimated.

The underlying state $|\phi\rangle$ is unitarily rotated by an angle θ as:

$$|\phi(\theta)\rangle = U_\theta I |\phi\rangle, \tag{2.9}$$

where

$$U_\theta = \begin{bmatrix} cos\frac{\theta}{2} & -sin\frac{\theta}{2} \\ sin\frac{\theta}{2} & cos\frac{\theta}{2} \end{bmatrix} \tag{2.10}$$

The corresponding theoretical value of the inequality $\mathcal{C}$ for the aforementioned state Eqn. 2.9 is found to be $\mathcal{C} = \frac{1}{4}(11 + 3cos\theta)$ and is plotted in Fig. along with the experimentally observed values at various θ angles.

Table 2.1: Table providing the product operators for the two-qubit system that are utilised in this chapter. These operators are mapped to the Pauli Z operators by mapping the initial state $\rho \rightarrow \rho_i = U_i.\rho.U_i^\dagger$.

Observables	Unitary Operator
$\langle XX \rangle$ = tr($\rho_1.Z_2$)	$U_1 = \mathrm{CNOT}_{12}\, Y_2 Y_1$
$\langle YY \rangle$ = tr($\rho_2.Z_2$)	$U_2 = \mathrm{CNOT}_{12}\overline{X}_2\overline{X}_1$
$\langle ZI \rangle$ = tr($\rho_3.Z_1$).	U_3 = Identity
$\langle ZZ \rangle$ = tr($\rho_4.Z_2$)	$U_4 = \mathrm{CNOT}_{12}$
$\langle IZ \rangle$ = tr($\rho_5.Z_2$)	U_5 = Identity

2.3 NMR implementation of fully contextual quantum correlations using two NMR qubits

To implement the inequality on a four-dimensional quantum system, the molecule of ^{13}C-enriched chloroform dissolved in acetone-D6 was used, with ^{1}H and ^{13}C spins being labeled as qubit 1 and qubit 2, respectively (see Fig. 2.3 and Table 2.2 for details of the experimental parameters).

The Hamiltonian for a two-qubit system is given by [107]

$$\mathcal{H} = -\nu_{\mathrm{H}} I_z^{\mathrm{H}} - \nu_{\mathrm{C}} I_z^{\mathrm{C}} + J_{\mathrm{HC}} I_z^{\mathrm{H}} I_z^{\mathrm{C}} \tag{2.11}$$

Table 2.2: Table listing the NMR parameters for ^{13}C- labeled chloroform molecule used as a two-qubit system

Qubit	ν (Hz)	J (Hz)	T_1 (s)	T_2 (s)
^{1}H	4787.86	$J_{HC} = 215.11$	7.9	2.95
^{13}C	11814.09		16.6	0.3

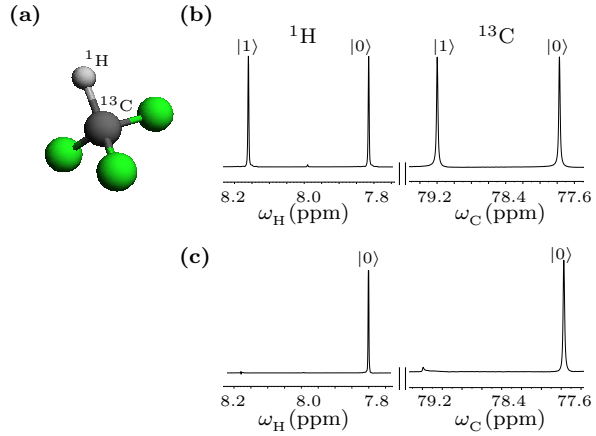

Figure 2.3: (a) Structure of ^{13}C- labeled chloroform molecule with ^{1}H and ^{13}C spins being realized as two-qubit system. (b) NMR spectra of ^{1}H and ^{13}C spins corresponding to thermal equilibrium state and (c) pseudopure state after the application of $\frac{\pi}{2}$ detection pulse. The logical state of the qubit, which is passive during the transition, is identified on each peak.

where $\nu_{\rm H}$, $\nu_{\rm C}$ are the chemical shifts, $I_z^{\rm H}$, $I_z^{\rm C}$ are the z-components of the spin angular momentum operators of the ^{1}H and ^{13}C spins, respectively, and $J_{\rm HC}$ is the scalar coupling constant. The system was initialized in the pseudopure state (PPS), i.e., $|00\rangle$, using the spatial averaging [108] with the density operator given by

$$\rho_{00} = \frac{1}{4}(1-\epsilon)\mathbb{I}_4 + \epsilon|00\rangle\langle 00| \tag{2.12}$$

where $\mathbb{I}_4$ is the 4×4 identity operator and ϵ is proportional to spin polarization and can be evaluated from the ratio of magnetic and thermal energies of an ensemble of magnetic moments μ in a magnetic field B at temperature T; $\epsilon \sim \frac{\mu B}{k_B T}$ and at room temperature and for a $B \approx 10$ Tesla, $\epsilon \approx 10^{-5}$. The state fidelity of the experimentally prepared PPS was computed to be 0.99 using the fidelity measure [109]. For the experimental reconstruction of the density operator full quantum state tomography [42, 110] was performed using a set of preparatory pulses $\{II, IX', IY', X'X'\}$, where I implies no operation and and X'(Y') denotes a qubit-selective radio-frequency (rf) pulse of 90° flip angle of phase x(y). The durations of $\frac{\pi}{2}$ pulses for ^{1}H, ^{13}C were 9.56 μs at power level 18.14 W, 16.15 μs at a power level of 179.47 W, respectively.

The quantum circuit to achieve the required states to test the inequality $\mathcal{C}$ on a four-dimensional quantum system is shown in Fig. 2.4(a) and the corresponding NMR pulse sequence is shown in Fig. 2.4(b). Eight different states were generated by varying the flip angle θ over a range of values: 180°, 120°, 90°, 69.23°, 60°,45°, $30^\circ$and 0°.

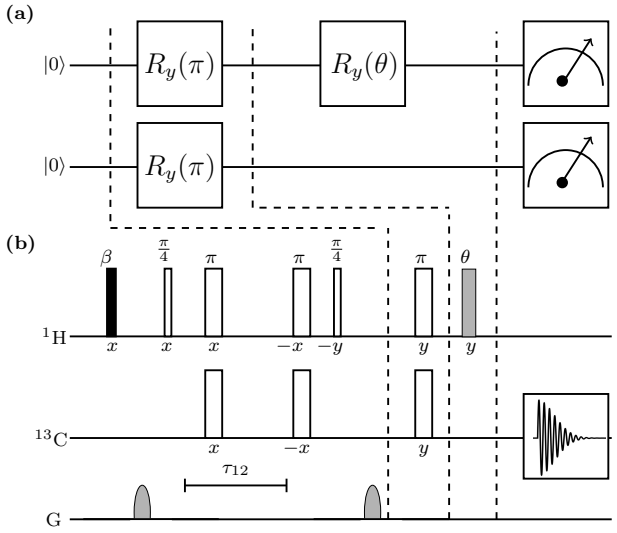

Figure 2.4: (a) Quantum circuit that modifies the flip angle θ to create the various two-qubit states required (b) NMR pulse sequence associated with the quantum circuit. The NMR pulse sequence for the PPS state $|00\rangle$ preparation is shown before the first dashed black line with the value of flip angle $\beta = 59.69°$. The various states are generated by varying the flip angle θ. The interval τ_{12} is defined as $\frac{1}{2J_{HC}}$ where J_{HC} is the scalar coupling between ^{1}H and ^{13}C.

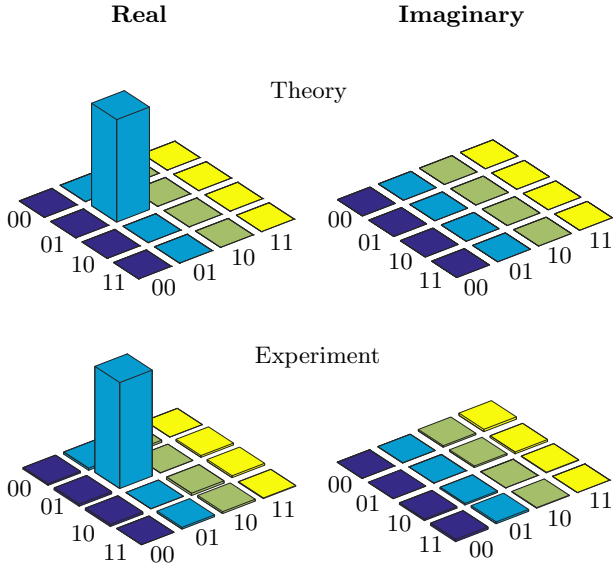

Figure 2.5: The theoretical (up) and experimental (down) tomographs of the $\langle\phi_1| = (0, -1, 0, 0)$ state, with the experimental fidelity of 0.99.

The state that is prepared with the flip angle $\theta = 180^\circ$ gives the minimum value of $\mathcal{C}$, while the state which is prepared without applying any rf pulse ($\theta = 0^\circ$) gives the maximum value. All the states required for testing the inequality on the four-dimensional quantum system were experimentally prepared with state fidelities greater than or equal to 0.97. The tomograph for one such experimentally prepared state with the flip angle $\theta = 180^\circ$ and state fidelity 0.99 is depicted in Fig. 2.5.

For each of these eight different initial states, the contextuality test was repeated three times. The mean values and the corresponding error bars were calculated and the results are shown in Fig. 2.6, where the inequality values are plotted for different θ values. The maximum of the sum of probabilities using classical theory is 3 and the maximum of the sum of probabilities using quantum theory is 3.5, which are shown by dotted and dashed lines, respectively, Fig. 2.6. As can be seen from the values tabulated in Table 2.3, the theoretically computed and experimentally measured values of the inequality agree well to within experimental errors.

From Fig. 2.6 it can be seen that the violation for the inequality $\mathcal{C}$ decreases as the original state $|\phi\rangle$is rotated through an angle θ; no violation is observed for the angle $\theta > 70^\circ$. The corresponding curve is found to obey a nonlinear trend such that smaller rotations lead to minor changes in the violation, while larger rotations may lead to a situation where no violation is observed.

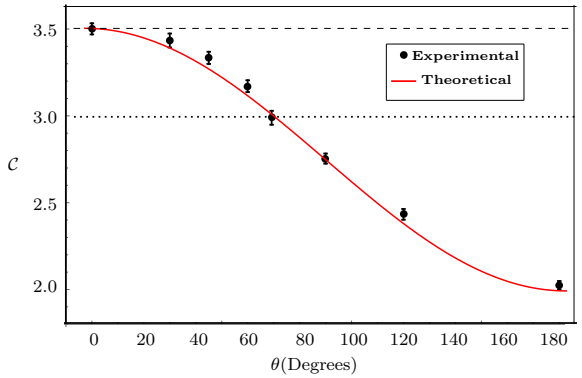

Figure 2.6: Graph showing the inequality $\mathcal{C}$ values for the different states versus different flip angles θ states. Dotted and dashed lines represent the maximum values using classical and quantum theory, respectively.

Table 2.3: Table showing the values of the inequality $\mathcal{C}$ calculated theoretically and experimentally for various states produced by rotating the initial state $|\phi\rangle$ with different values of flip angle θ.

θ	Theoretical	Experimental
180°	2.000	2.024±0.025
120°	2.375	2.433±0.031
90°	2.750	2.754±0.029
69.23°	3.016	2.989±0.040
60°	3.125	3.171±0.034
45°	3.280	3.334±0.035
30°	3.399	3.434±0.040
0°	3.500	3.501±0.032

2.4 Fully contextual quantum correlations in eight-dimensional Hilbert space

In this section we first review a contextuality inequality which is capable of revealing fully contextual quantum correlations as developed by Cabello [90], which requires a Hilbert space dimensionality of at least 6. We then design a modified version of the inequality via decomposition of the projectors into Pauli matrices, for ease of experimental implementation. We experimentally test the inequality on an eight-level quantum system, physically realized via three NMR qubits.

One of the simplest tests of contextuality, capable of revealing fully contextual quantum correlations, requires only five measurements, but of ten different projectors $\{\Pi_i\}$, and is of the form

$$\mathcal{K} = \frac{1}{2}\sum_{i=0}^{4} P(\Pi_i + \Pi_{i+1} + \Pi_{i+5} + \Pi_{i+7} = 1) \overset{\text{NCHV}}{\leq} 2 \overset{\text{QM, GP}}{\leq} \frac{5}{2}, \tag{2.13}$$

where the sum in the indices is defined as standard addition except for three cases where we define it as $4 + 1 = 0$, $3 + 7 = 5$, and $4 + 7 = 6$ to ensure that only those vertices connected by the same edge style in Fig. 2.7 appear in the sum. To elaborate, the term corresponding to $i = 4$ will be of the form $P(\Pi_4 + \Pi_0 + \Pi_9 + \Pi_6 = 1)$.

Since both the KCBS and the aforementioned inequality Eqn. 2.13 require only five different measurements, the above scenario is termed a KCBS twin inequality, with the only difference that it is capable of revealing fully contextual quantum correlations and requires quantum systems having Hilbert space dimension at least 6. We will henceforth refer to this inequality as the KCBS twin inequality.

The scenario corresponding to the KCBS twin inequality Eqn. 2.13 can be represented by an exclusivity graph as shown in Fig. 2.7. In this graph, each vertex corresponds to a unit vector $|v_i\rangle$ used to construct the projectors $\{\Pi_i\}$, and two vertices are connected by an edge if and only if they are exclusive. From the graph it is possible to identify five different measurements $\mathcal{M}_i$, which are defined as

$$\mathcal{M}_i = \{\Pi_i, \Pi_{i+1}, \Pi_{i+5}, \Pi_{i+7}\}, \quad \forall i \in \{0, 1, ..., 9\}. \tag{2.14}$$

These measurements can be identified from the graph in Fig. 2.7 by five sets of four interconnected vertices, each represented by a different line style.

An explicit form of the KCBS twin inequality Eqn. 2.13 which saturates the QM

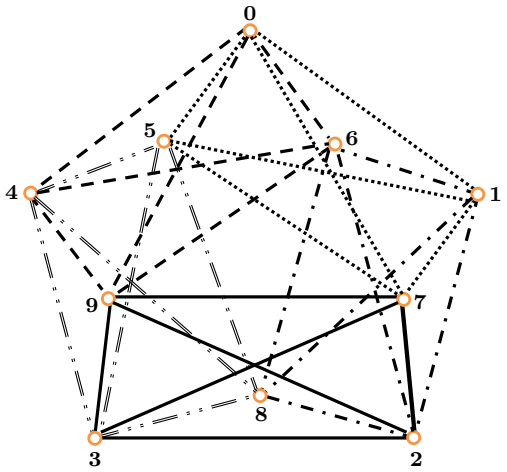

Figure 2.7: A ten-vertex orthogonality graph, representing the twin KCBS inequality $\mathcal{K}$ with ten vertices labeled $0, 1, 2, ...9$ corresponding to five measurements. Each vertex represents a projector, and an edge represents the orthogonality relationship between the projectors. Five different measurements are represented by five different edge styles and each of the measurements is joined by four vertices.

and GP bound can be obtained if we consider the unit vectors $|v_i\rangle$ defined as,

$$\langle v_0| = \frac{1}{\sqrt{8}}(\sqrt{2}, -\sqrt{2}, 0, 0, 2, 0, 0, 0), \tag{2.15a}$$

$$\langle v_1| = \frac{1}{\sqrt{8}}(\sqrt{2}, 0, 0, \sqrt{2}, -1, \sqrt{3}, 0, 0), \tag{2.15b}$$

$$\langle v_2| = \frac{1}{2}(1, -1, -1, -1, 0, 0, 0, 0), \tag{2.15c}$$

$$\langle v_3| = \frac{1}{2}(1, -1, 1, 1, 0, 0, 0, 0), \tag{2.15d}$$

$$\langle v_4| = \frac{1}{\sqrt{8}}(\sqrt{2}, 0, 0, -\sqrt{2}, -1, \sqrt{3}, 0, 0), \tag{2.15e}$$

$$\langle v_5| = \frac{1}{\sqrt{8}}(\sqrt{2}, 0, -\sqrt{2}, 0, -1, -\sqrt{3}, 0, 0), \tag{2.15f}$$

$$\langle v_6| = \frac{1}{\sqrt{8}}(\sqrt{2}, 0, \sqrt{2}, 0, -1, -\sqrt{3}, 0, 0), \tag{2.15g}$$

$$\langle v_7| = \frac{1}{2}(1, 1, 1, -1, 0, 0, 0, 0), \tag{2.15h}$$

$$\langle v_8| = \frac{1}{\sqrt{8}}(\sqrt{2}, \sqrt{2}, 0, 0, 2, 0, 0, 0), \tag{2.15i}$$

$$\langle v_9| = \frac{1}{2}(1, 1, -1, 1, 0, 0, 0, 0). \tag{2.15j}$$

The state $|\psi\rangle$ on which the measurements $\mathcal{M}_i$ will be performed is chosen as

$$\langle\psi| = (1, 0, 0, 0, 0, 0, 0, 0), \tag{2.16}$$

so that $\langle v_i|\psi\rangle = \frac{1}{2}\ \forall i \in \{0, 1, ..., 9\}$ which subsequently ensures the exclusivity relation $P(\Pi_i + \Pi_{i+1} + \Pi_{i+5} + \Pi_{i+7} = 1) = 1$, $i = 0, 1, ..., 4$.

To experimentally test the inequality $\mathcal{K}$ on an eight-level quantum system using three NMR qubits, the expectation values of the observables involved have to be determined for an experimentally prepared state. The expectation value of desired observables can be determined by decomposing the observables as a linear superposition of the Pauli operators as has been detailed in Sec. 2.2. For a three-qubit system, any observable can be decomposed as a linear superposition of 64 Pauli basis operators.

In order to evaluate the twin KCBS inequality experimentally, we first decompose the projectors involved in terms of Pauli operators $\{I, X, Y, Z\}$ for three qubits. Since in an NMR quantum information processor it is only possible to measure the expectation value of the observables, we first translate Eqn. 2.13 in terms of expectation values as

$$\mathcal{K} = \frac{1}{2}\sum_{i=0}^{4} P(\Pi_i + \Pi_{i+1} + \Pi_{i+5} + \Pi_{i+7}) = \sum_{i=0}^{9}\langle\Pi_i\rangle = \sum_{i=0}^{9} tr(\Pi_i\rho) \tag{2.17}$$

where $\rho = |\psi\rangle\langle\psi|$. Using the decomposition, the inequality $\mathcal{K}$ Eqn. 2.13 can be rewritten as:

$$\mathcal{K} = \frac{1}{8}tr(A \cdot \rho) \overset{\text{NCHV}}{\leq} 2 \overset{\text{QM, GP}}{\leq} \frac{5}{2}, \tag{2.18}$$

and

$$A = IIZ + 4IZI + IZZ + 4ZII + ZIZ - 2ZZI + ZZZ + 10III \tag{2.19}$$

which we experimentally verify using a three-qubit NMR information processor. We note here in passing that the decomposition of the observable A consists only of diagonal Pauli operators, which can be easily observed in an experiment. The fact that the observable A can be decomposed as a combination of only diagonal Pauli operators is an interesting coincidence. Furthermore, in an NMR setup, it is easier to implement these diagonal operators as compared to other operators which have diagonal and off-diagonal terms.

For example, the expectation value of $\langle IIZ\rangle$ can be obtained simply by measuring the NMR peak intensities after applying a detection pulse on the third qubit. The

Table 2.4: Table listing the product operators used in this chapter for the three-qubit system. These operators are mapped to the Pauli Z operators by mapping the initial state $\rho \rightarrow \rho_i = U_i.\rho.U_i^\dagger$.

Observables	Unitary Operator
$\langle IIZ \rangle$ = tr($\rho_1.Z_2$)	U_1 = Identity
$\langle IZI \rangle$ = tr($\rho_2.Z_2$)	U_2 = Identity
$\langle IZZ \rangle$ = tr($\rho_3.Z_1$).	$U_3 = \mathrm{CNOT}_{23}$
$\langle ZII \rangle$ = tr($\rho_4.Z_2$)	U_4 = Identity
$\langle ZIZ \rangle$ = tr($\rho_5.Z_2$)	$U_5 = \mathrm{CNOT}_{13}$
$\langle ZZI \rangle$ = tr($\rho_5.Z_2$)	$U_5 = \mathrm{CNOT}_{12}$
$\langle ZZZ \rangle$ = tr($\rho_5.Z_2$)	$U_5 = \mathrm{CNOT}_{23}\mathrm{CNOT}_{12}$

underlying state $|\psi\rangle$ is unitarily rotated by an angle θ as

$$|\psi(\theta)\rangle = U_\theta II|\psi\rangle, \tag{2.20}$$

where U is as given in Eqn. 2.10. For the aforementioned state (2.20), the theoretical value of the inequality (2.18) is found to be $\mathcal{K} = \frac{1}{2}(4 + cos\theta)$, which is plotted in Fig. along with the experimentally observed values at various θ angles. By experimentally measuring the expectation value of the observable A for state ρ, the value of inequality $\mathcal{K}$ can be estimated. For example, in order to determine $\langle IZZ \rangle$, the underlying state ρ is mapped to the state $\rho_3 = U_3.\rho.U_3^\dagger$ with $U_3 = \mathrm{CNOT}_{23}$, followed by measuring $\langle Z_3 \rangle$, which is is equivalent to the expectation value of $\langle IZZ \rangle$ for the state ρ. The explicit mapping of the expectation value of the observables onto Pauli Z operators for three qubits is given in Table 2.4.

2.5 NMR implementation of fully contextual quantum correlations using three NMR qubits

To experimentally implement the KCBS twin inequality capable of revealing fully contextual quantum correlations for an eight-dimensional quantum system, we used the molecule of ^{13}C -labeled diethyl fluoromalonate dissolved in an acetone-D6 was used. ^{1}H, ^{19}F and ^{13}C spin-half nuclei being encoded as qubit one, qubit two and qubit three, respectively (see Fig. 2.8 for the molecular structure and corresponding NMR spectrum of the PPS state, and Table 2.5 for details of the experimental NMR parameters).

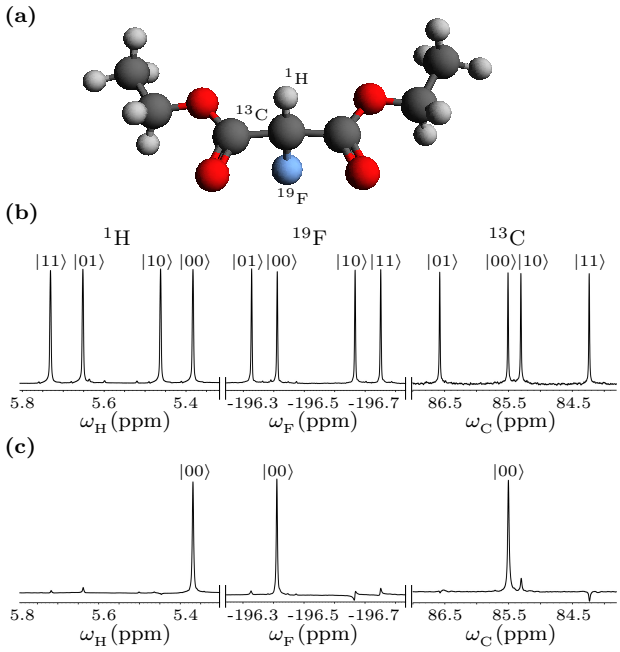

Figure 2.8: (a) Structure of ^{13}C- labeled diethyl fluoromalonate molecule with ^{1}H, ^{19}F and ^{13}C spins being realized as the three-qubit system. (b) NMR spectra of ^{1}H, ^{19}F and ^{13}C corresponding to thermal equilibrium state and (c) pseudo pure (PPS) state after the application of $\frac{\pi}{2}$ detection pulse. The logical state of the qubit, which is passive during the transition, is identified on each peak.

The NMR Hamiltonian for a three-qubit system is given by

$$\mathcal{H} = -\sum_{i=1}^{3} v_i I_z^i + \sum_{i>j,i=1}^{3} J_{ij} I_z^i I_z^j \tag{2.21}$$

where the indices i, j = 1, 2, or 3 represent the qubit number and where ν_i is the respective chemical shift in rotating frame, J_{ij} is the scalar coupling constant, and I_z^i

is z-components of the spin angular momentum operators of the i^{th} qubit. The system was initialized in the pseudopure state (PPS), i.e., $|000\rangle$, using the spatial averaging [111] with the density operator given by

$$\rho_{000} = \frac{1-\epsilon}{2^3}\mathbb{I}_8 + \epsilon|000\rangle\langle 000| \tag{2.22}$$

where ϵ is proportional to spin polarization and $\mathbb{I}_8$ is the 8×8 identity operator. The fidelity of the experimentally prepared PPS state was computed to be 0.96. Full quantum state tomography was performed to experimentally reconstruct the density operator via a set of preparatory pulses $\{III, IIY', IY'Y', Y'II, X'Y'X', X'X'Y', X'X'X'\}$, where I implies no operation and X'(Y') denotes a qubit-selective rf pulse of flip angle 90° of phase x(y).

Table 2.5: Table representing NMR parameters for ^{13}C- labeled diethyl fluoromalonate molecule used as a three-qubit system

Qubit	ν (Hz)	J (Hz)	T_1 (s)	T_2 (s)
^{1}H	3334.24	$J_{HF} = 47.5$	3.4	1.6
^{19}F	-110999.94	$J_{HC} = 161.6$	3.7	1.55
^{13}C	12889.53	$J_{FC} = -191.5$	3.6	1.3

Experiments were performed at room temperature (294 K) on a Bruker Avance III 600-MHz FT-NMR spectrometer equipped with a QXI probe. Local unitary operations were achieved by using highly accurate and calibrated spinselective transverse rf pulses of suitable amplitude, phase, and duration. Nonlocal unitary operations were achieved by free evolution under the system Hamiltonian, of suitable duration under the desired scalar coupling with the help of embedded π refocusing pulses. The durations of $\frac{\pi}{2}$ pulses for ^{1}H, ^{19}F, and ^{13}C were 9.36 μs at 18.14 W power level, 23.25 μs at a power level of 42.27 W, and 15.81 μs at a power level of 179.47 W, respectively.

The quantum circuit to construct the states required to test fully contextual quantum correlations is shown in Fig. 2.9(a) and the corresponding NMR pulse sequence is shown in Fig. 2.9(b). Different states can be prepared by varying the value of the flip angle θ of the rf pulse. We prepared seven different states by varying the flip angle θ to attain a range of values: 180°, 120°, 90°, 60°, 45°,36°, and 0°. The state prepared with $\theta = 180$ gives the minimum value of $\mathcal{K}$, while the state prepared without applying

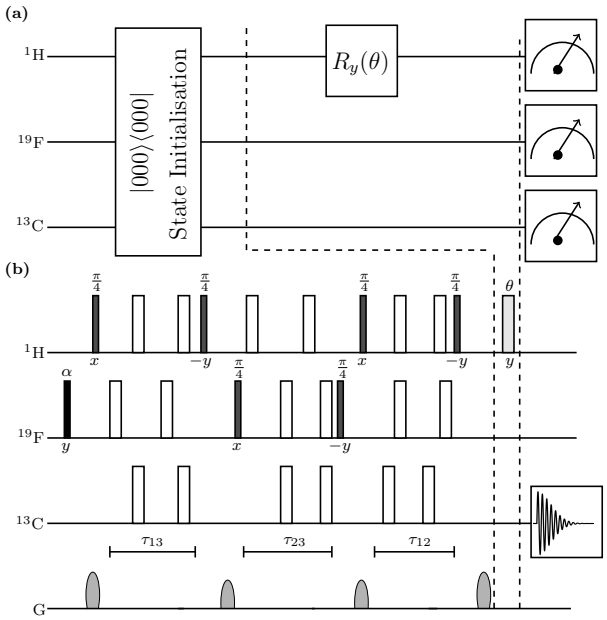

Figure 2.9: (a) Quantum circuit that alters θ, the flip angle, to produce the different three-qubit states needed (b) NMR pulse sequence associated with the quantum circuit. The NMR pulse sequence for the PPS state $|000\rangle$ preparation is shown before the first dashed black line with the value of flip angle $\alpha = 57.67°$. The various states are generated by varying the flip angle θ. The broad white rectangles represent π pulses and the flip angle and corresponding phases of other pulses are written alongside them. The intervals τ_{12}, τ_{13}, τ_{23} are defined as $\frac{1}{2J_{HF}}$, $\frac{1}{2J_{HC}}$, $\frac{1}{2J_{FC}}$ respectively (J_{HF}, J_{HC}, J_{FC} are the scalar couplings between the respective NMR qubits).

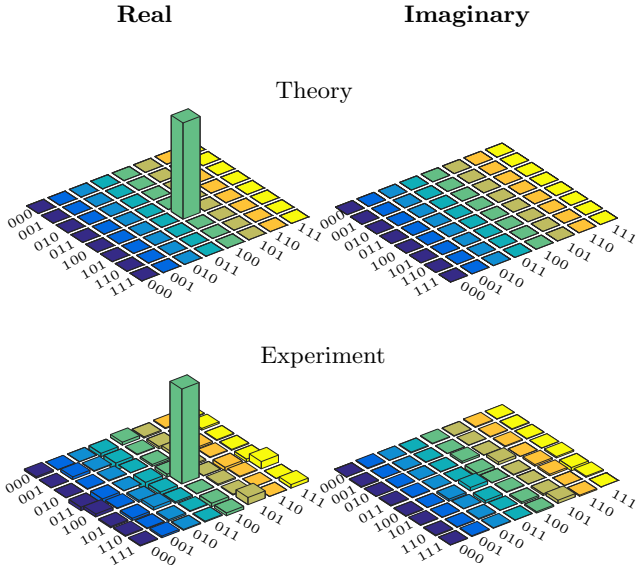

Figure 2.10: The theoretical (up) and experimental tomographs (down) tomographs of the $\langle\psi_1| = (0, 0, 0, 0, 1, 0, 0, 0)$ state, with an experimental fidelity of 0.97.

any rf pulse ($\theta = 0°$) gives the maximum value. All the states required to demonstrate the KCBS twin inequality on an eight-dimensional Hilbert space which are capable of revealing the transformation from classical correlations to fully contextual correlations were experimentally prepared with state fidelities greater than or equal to 0.96.

The tomograph of one such experimentally reconstructed state with flip angle $\theta = 180°$ with state fidelity 0.97 is depicted in Fig. 2.10. For each of the initial states, the contextuality test was repeated three times. The mean values and the corresponding error bars were computed and the results are shown in Fig. 2.11. where the inequality values are plotted for different values of the parameter θ. The maximum of the sum of probabilities using classical theory is 2 and the maximum of the sum of probabilities using quantum theory is 2.5; they are depicted by dotted and dashed lines, respectively, in Fig. 2.11. The theoretically computed and experimentally obtained values of the inequality for different values of the θ parameter are tabulated in Table 2.6. The theoretical and experimental values match well, within the limits of experimental errors. From Fig. 2.11 it can also be seen that the violation observed for the KCBS twin inequality decreases as the original state $|\psi\rangle$ is rotated through an angle θ, with no violation when the transformed state is orthogonal to the original state. Furthermore, the plot is nonlinear, indicating that smaller rotations lead to minor changes in violation, while larger rotations may also lead to observing no violation at all.

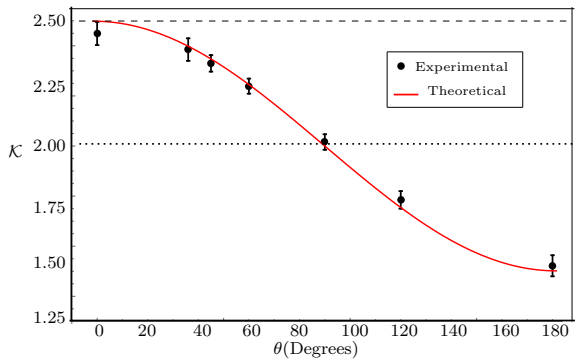

Figure 2.11: Graph denoting the inequality $\mathcal{K}$ values for the different states versus different values of flip angle θ. Dotted and dashed lines represent the maximum values using classical and quantum theory, respectively.

Table 2.6: Table displaying values of the inequality $\mathcal{K}$ calculated theoretically and experimentally for various states produced by rotating with angle θ, from the initial state $|\psi\rangle$.

θ	Theoretical	Experimental
180°	1.500	1.522±0.042
120°	1.750	1.785±0.035
90°	2.000	2.016±0.031
60°	2.250	2.239±0.030
45°	2.353	2.33±0.033
36°	2.404	2.385±0.045
0°	2.500	2.449±0.046

2.6 Conclusions

In this chapter, we experimentally demonstrated fully contextual quantum correlations on an NMR quantum information processor. We studied two distinct inequalities capable of revealing such correlations: The first inequality used ten measurements on a four-dimensional Hilbert space while the second inequality used five measurements on an eight dimensional Hilbert space to reveal fully contextual correlations. However, both inequalities involved the same number of projectors. For an experimental demonstration of each inequality, every projector was decomposed in terms of the Pauli basis and the corresponding inequality recast in terms of Pauli operators, thereby reducing the need for resource intensive full state tomography. Both inequalities $\mathcal{C}$ and $\mathcal{K}$ were experimentally implemented with a fidelity greater than or equal to 0.96 by measuring the expectation values of only five and seven Pauli operators, respectively, for the state which maximizes the violation.

In addition to demonstration of fully contextual quantum correlations, we analyzed the behavior of each inequality under rotation of the underlying state, which unitarily transforms it to another pure state. The experiments were repeated for various states rotated through an angle θ and were in good agreement with theoretical results. It was seen that both the inequalities follow a nonlinear trend, while the inequality $\mathcal{K}$ offers a greater range of violation than the inequality $\mathcal{C}$ with respect to the parameter θ.

An experimental implementation of fully contextual quantum correlations is an important step towards achieving information processing tasks, for which no postquantum theory can do better. While the inequality $\mathcal{C}$ has been experimentally observed in optical systems, an experimental demonstration of the inequality $\mathcal{K}$ is difficult owing to the high dimensionality of the Hilbert space required. Our work asserts that NMR is an optimal test bed for such scenarios. Results of this chapter are contained in Phys. Rev. A **100**, 022109(2019).

Chapter 3

Implementation of state-independent contextual inequalities on an NMR quantum processor, using non-invasive measurements

3.1 Introduction

The issue of hidden variables has been a point of contention ever since the development of quantum theory. Einstein et al. derived a paradox (EPR paradox) [112] that claimed quantum mechanics was incomplete and later Bell demonstrated [55] that no local ontological model is consistent with the EPR argument. This suggests that quantum correlations behave fundamentally different than those that can be accounted for by classical models. As discussed in the previous chapter, the violation of a Bell inequality reveals the incompatibility of quantum theory with the local hidden variable model. Kochen and Specker adopted a novel method for determining quantumness by introducing the notion of contextuality that does not fit in non-contextual hidden variable (NCHV) theories [58, 113]. In order to disprove the NCHV hypotheses experimentally, the hidden variable theorems were constructed in a form that allowed them to be applied to experimental settings [114]. In order to identify minimal contextuality scenarios, an efficient construction for minimal GHZ and Hardy-style demonstrations of the Kochen-Specker theorem was put forth [115]. There exist a scenario where the kinematics predictions of quantum theory and the NCHV model are compatible [116].

As mentioned in the previous chapter, several state independent and dependent tests

of contextuality have been developed [77, 84, 87, 117]. Contextuality has been experimentally verified by several experimental groups [68, 69, 97, 98, 99, 100, 101, 102, 103, 104]. The KCBS inequality, which uses the five measurements on the qutrit state, revealed the first state-dependent test of contextuality [61]. To describe fully contextual quantum correlations, a twin KCBS inequality was developed [90]. The Peres-Mermin (PM) inequality, a state-independent contextuality inequality, is regarded as the easiest way to demonstrate the KS theorem. PM inequality utilizes the six compatible measurements of nine dichotomic observables in the four-dimensional Hilbert space [79, 118].

The Leggett-Garg (LG) inequality was developed, capable of capturing the quantumness of temporal correlation under the assumptions of macroscopic realism and noninvasive measurements [119]. LG inequality demands noncommuting observables being sequentially measured at various times. Later, different LG-type inequalities has been developed using different measurement scenarios [120, 121, 122, 123]. Temporal contextuality was tested via the violation of the temporal KCBS inequality [124]. Additionally, violation of temporal CHSH inequality, a Bell-type inequality, was developed, supporting the multipartite nature of temporal correlations [125]. The Tsirelson bound, which has been explored for both Bell-type [126, 127, 128] and LG-type [129] inequalities, is defined as the most degree to which inequality can be violated. Unexpected outcomes were reported in the case of some LG-type inequalities, where the maximum degree of violation was higher than the Tsirelson bound and grew as the system's size increased [130]. Although Bell-inequalities, NC inequalities, and LG inequalities are all produced under various conditions, they all address the same issue, namely the results of context-free measurements of quantum mechanical observables. It has been shown that contextual scenarios can be transformed into the LG- and Bell-type inequalities [131].

The temporal contextuality inequality developed using noninvasive measurements. Therefore, we must perform the noninvasive measurement, which is highly challenging to do in experiments, in order to capture the temporal quantum connection. Lower bounds on the quantum dimension were obtained using state-independent temporal noncontextuality inequalities [80]. Experimental implementation of LG-type inequalities have been carried out using using polarized photons [132, 133], atomic ensembles [134], a hybrid optomechanical system [135], NMR systems [136, 137, 138, 139, 140], bosonic systems [141] and superconducting qubits [142].

In this chapter, we used an NMR quantum processor for the experimental implementation of the PM inequality. Violation of the PM inequality reveals state-indepenendent contextuality. Due to the fact that the PM inequality requires noninvasive measurements, we must do the noninvasive measurements experimentally. This was accomplished by using a three-qubit system, physically realized by a ^{13}C-labeled diethyl

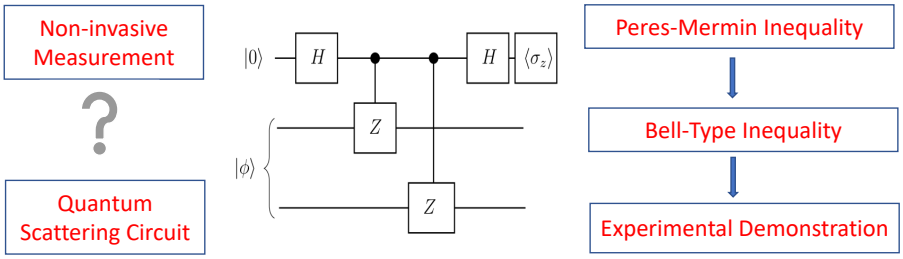

Figure 3.1: Scheme used to experimentally demonstrate violation of PM and Bell-type inequality using a quantum scattering circuit.

fluoromalonate molecule. First, we have generalized the quantum scattering [136], capable of measuring the n-point correlation where the observables are measured sequentially in time. We were able to perform a noninvasive measurement in the experiment using this quantum scattering circuit. Our circuit, in contrast to existing measurement techniques, can capture the desired temporal correlations in a single experimental run. For the violation of the temporal PM inequality, we applied our quantum scattering circuit capable of measuring correlations, involved in the PM inequality. This was done experimentally by sequentially measuring the three-point correlation function in order to estimate the expectation value of the joint probability distributions, which were involved in the PM inequality. Further, we have used a quantum scattering circuit to demonstrate the violation of a Bell-type inequality that corresponds to the temporal KCBS inequality. The graphical methodology for the experimental demonstration of violation of PM and Bell-type inequality using a quantum scattering circuit is given in Fig. 3.1.

3.2 Non-invasive measurements

Noninvasive measurements which do not disturb the subsequent evolution of a system are in general not possible in quantum mechanics. Several noncontextual inequalities such as the LG inequality or the temporal Bell-type inequalities require expectation values of the product of an observable at different times, to capture temporal quantum correlations. Ideally, one would imagine that non-invasive measurements would be required to compute such quantities. Experiments to carry out such noninvasive measurements are typically nontrivial to design and implement. It should be noted that if these individual measurements were to be carried out one by one, they would not be non-invasive in nature. While this equivalence is true according to a quantum mechanical description, it no longer holds if one assumes a nonclassical hidden variable

description, and one would need to associate a measurement procedure with classical variables using the same experimental setup.

In general, the concept of noninvasive measurability, implies the possibility of performing a measurement without disturbing the subsequent evolution of a system. Such type of measurement can be performed using quantum scattering circuit where the ancillary qubit probes the time correlations of the ensemble without disturbing its subsequent dynamics. A probe qubit (ancillary) on a scattering circuit interacts with the system in such a way that a measurement of its state after the interaction brings the information about the system state. This requires that the input state of the probing qubit can be known and the interaction can be controlled. Quantum scattering circuit's operation is demonstrated using NMR quantum information processor, which measures the time correlation.

Simulating the non-invasive measurement of the expectation value of the product of the same observable at different times via a single overall measurement is achieved via the generalized scattering circuit.

3.3 Generalized quantum scattering circuit for non-invasive measurements

Our generalized quantum scattering circuit is aimed at carrying out noninvasive measurements which we will use to investigate the violation of temporal contextuality inequalities. The standard quantum scattering circuit consists of a probe qubit (ancillary) and the system qubit. The generalized quantum scattering circuit which we have designed to compute n point correlations functions involves performing n successive noninvasive measurements on an N qubit quantum system, using only one ancilla qubit as the probe qubit. The circuit measures the n-point correlation function $\langle O(t_1)O(t_2)...O(t_n)\rangle$, wherein an observable is measured sequentially at time instants $t_1, t_2, ...t_n$.

Fig. 3.2 depicts a schematic diagram of the generalized quantum scattering circuit to generate temporal correlations and demonstrate violation of temporal noncontextuality. The system is prepared in a known initial state, which interacts with the ancilla in such a way that a measurement over its state after the interaction, brings out the information about the system state. The 'probe qubit' (ancillary qubit) is prepared in a known initial state and the 'system qubit' is prepared in the state for which the observables are to be measured. The system is initially in the state $|\psi\rangle$, and is brought in contact with an ancilla qubit prepared in the state $|0\rangle$. This ancilla acts as a 'probe particle' in the quantum scattering circuit. The circuit is implemented in three steps:

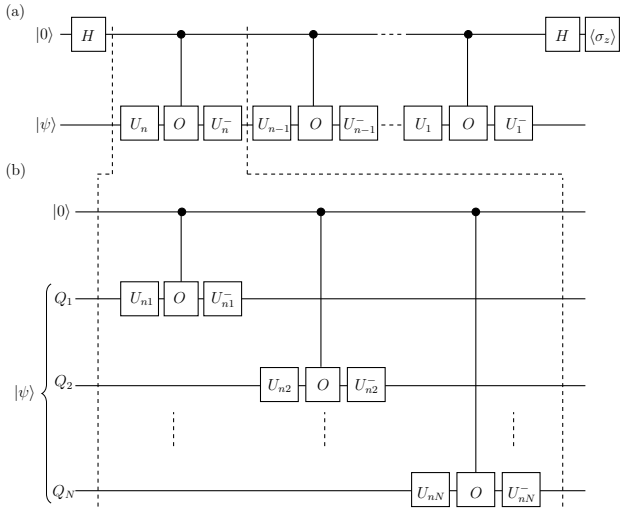

Figure 3.2: (a) Diagrammatic representation of a quantum scattering circuit capable of measuring the n point time correlation function, defined as $\langle[O_1(t_1)\otimes O_2(t_1)\cdots\otimes O_N(t_1)][O_1(t_2)\otimes O_2(t_2)\cdots\otimes O_N(t_2)]\ldots[O_1(t_n)\otimes O_2(t_n)\cdots\otimes O_N(t_n)]\rangle$. The unitary operators are defined as $U_1^{\mp}=e^{\pm\frac{iHt_1}{\hbar}}$,... $U_{n-1}^{\mp}=e^{\pm\frac{iHt_{n-1}}{\hbar}}$, $U_n^{\mp}=e^{\pm\frac{iHt_n}{\hbar}}$. (b) Expanded circuit diagram of the generalized quantum scattering circuit between dotted lines in panel (a). The circuit representing the reconstruction of the correlation function $\langle[O_1(t_n)\otimes O_2(t_n)\cdots\otimes O_N(t_n)]\rangle$, such that $O_i(t_n)$ is measured on the ith qubit with $i=1...N$. $|\psi\rangle$ corresponds to the initial state and $U_{n1}^{\mp}=e^{\pm\frac{iHt_{n1}}{\hbar}}$, $U_{n2}^{\mp}=e^{\pm\frac{iHt_{n2}}{\hbar}}$..., $U_{nN}^{\mp}=e^{\pm\frac{iHt_{nN}}{\hbar}}$.

1. A Hadamard gate is applied on the ancilla qubit.
2. A Controlled-U operator is then applied (does nothing if the state of the ancilla is $|0\rangle$).
3. A Hadamard gate is once again applied on the ancilla qubit and a measurement is performed on this qubit to detect its polarization (corresponding to measuring the expectation values of Pauli operators σ_z).

For non-invasive measurements, the input state of the system qubit has to be prepared in such a way that it is not affected by the application of the 'Controlled-U' operator. This is achieved as follows:

The initial state is $|0\rangle \otimes |\psi\rangle$. After applying Hadamard on ancilla qubit, the state is transformed to $\frac{1}{\sqrt{2}}(|0\rangle + |1\rangle) \otimes |\psi\rangle$. Application of the Controlled-U operation changes the state to $\frac{1}{\sqrt{2}}(|0\rangle \otimes |\psi\rangle + |1\rangle \otimes U|\psi\rangle)$ with $U = e^{-iHt_1} O e^{iHt_1} e^{-iHt_2} O e^{iHt_2} \cdots$. Finally, the state after application of the second Hadamard gate on the ancilla qubit turns out to be:

$$\begin{aligned} &\frac{(|0\rangle + |1\rangle) \otimes |\psi\rangle + (|0\rangle - |1\rangle) \otimes U|\psi\rangle}{2} \\ =&\frac{|0\rangle \otimes (I+U)|\psi\rangle + |1\rangle \otimes (I-U)|\psi\rangle}{2} \end{aligned}$$

Thus, if a measurement of the ancilla qubit in the computational basis yields the result $|0\rangle$, the state of the system qubit is $(I+U)|\psi\rangle$; however if the measurement yields the result $|1\rangle$, the state of the system qubit is $(I-U)|\psi\rangle$. We note here that in this case, the operator U is a unitary because the observable O is a unitary (having only eigenvalues $+1$ or -1); however this is in general not true for an arbitrary observable.

Consider the input state:

$$\rho_{in} = \rho_{probe} \otimes \rho_{sys} = |0\rangle\langle 0| \otimes |\psi\rangle\langle\psi| \tag{3.1}$$

where the 'probe qubit' is prepared in the $|0\rangle$ state and the 'system qubit' is prepared in the state $|\psi\rangle$. After applying the unitary transformation shown in Fig. 3.2, the output is given by:

$$\begin{aligned} \rho_{\text{out}} &= |\psi_{\text{out}}\rangle\langle\psi_{\text{out}}|, \text{ with} \\ |\psi_{\text{out}}\rangle &= |0\rangle \otimes (I+U)|\psi\rangle + |1\rangle \otimes (I-U)|\psi\rangle, \text{ and} \\ U &= e^{\frac{iHt_1}{\hbar}} O e^{-\frac{iHt_1}{\hbar}} e^{\frac{iHt_2}{\hbar}} O e^{-\frac{iHt_2}{\hbar}} \cdots e^{\frac{iHt_n}{\hbar}} O e^{-\frac{iHt_n}{\hbar}} \end{aligned} \tag{3.2}$$

The expectation of any operator A is given by $\sum_i p_i \lambda_i$, where p_i is the probability to get the eigenvalue λ_i. Hence

$$\langle \sigma_z \rangle = p_0 - p_1 \tag{3.3}$$

where p_0 and p_1 are the probabilities to measure $|0\rangle$ with eigenvalue 1 and $|1\rangle$ eigenvalue -1, respectively. However p_0 and p_1 are also equal to the probabilities of having the state of the system in $(I+U)|\psi\rangle$ with eigenvalue 1, and $(I-U)|\psi\rangle$ with eigenvalue -1, respectively.

Hence,

$$\begin{aligned} \langle \sigma_z \rangle &= \langle U \rangle = \mathrm{Tr}(\rho_{sys} U) \\ &= \langle \psi | e^{-iHt_1} O e^{iHt_1} e^{-iHt_2} O e^{iHt_2} \cdots | \psi \rangle \\ &= \langle O(t_1).O(t_2)... \rangle \end{aligned} \tag{3.4}$$

where the operators $O(t_1), O(t_2)....$ commute. Therefore, the real part of the expectation value of the z-component of the spin angular momentum of the 'probe' qubit turns out to be related to the expectation values of the desired observables of the original state.

The generalized quantum scattering circuit can be used to experimentally demonstrate those inequalities which involve temporal correlation functions, such as the temporal PM noncontextual inequality and the temporal KCBS inequality. While the ideal negative measurement (INM) protocol described in Ref. [143] is similar to our measurement scheme, in the INM protocol the ancilla is coupled to only one of the two measurement outcomes and the protocol hence requires two experimental runs: with a CNOT gate as well as with an anti-CNOT gate. Our circuit on the other hand, requires only a single experimental run and does not require additional CNOT and anti-CNOT gates for its implementation.

3.4 Violation of temporal Peres-Mermin and Bell-type inequalities

3.4.1 Time-correlation functions

For the experimental implementation, we used the molecule of ^{13}C -labeled diethyl fluoromalonate dissolved in acetone-D6 as a three-qubit system (for more details see Chapter 2).

Consider performing a set of five dichotomic (i.e. the measurement outcomes are ± 1) measurements of variables $X_j, j = 1, ..5$ on a single system. Each measurement X_j is compatible with the preceding and succeeding measurements and the sums are modulo 5. Compatible measurements implies that the joint or sequential measurements of the variables X_j do not affect each other, which basically ensures that the measurements are noninvasive. We note here in passing that compatibility of the measurements

must be verified classically as well, and one cannot assume the quantum mechanical properties (such as commutativity of operators) to justify noninvasive measurability from a classical perspective. The existence of a joint probability distribution for all the measurement outcomes can be tested by constructing the KCBS inequality [131]:

$$\sum_{j=0}^{4}\langle X_j X_{j+1}\rangle \geq -3 \tag{3.5}$$

where -3 is the minimum value for an NCHV model. Noncontextual in this sense implies that the NCHV theory assigns a value to an observable which is independent of other compatible observables being measured along with it. By definition each correlation function is given by By definition each correlation function is given by [131]:

$$\langle X_i X_j\rangle = \sum_{x_i,x_j=\pm 1} x_i x_j p(x_i,x_j) \tag{3.6}$$

A "pentagon LG" inequality was constructed wherein [120]

$$\sum_{1\leq i<j\leq 5}\langle X_i X_j\rangle + 2 \geq 0 \tag{3.7}$$

This inequality has 10 two-time correlation functions which can be computed from one single experiment, wherein the measurements are performed in a manner such that the measurement of X_j does not affect the measurement outcome of X_i (noninvasive measurements). The two-time correlation function turns out to be [128]:

$$\langle X_i X_j\rangle = \frac{1}{2}Tr[\rho\{X_i,X_j\}] \tag{3.8}$$

for a density matrix ρ. The five measurable observables were chosen to be:

$$X_1 \equiv \sigma_z\,, X_2 \equiv \sigma_\theta\,, X_3 \equiv \sigma_z\,, X_4 \equiv \sigma_\theta\,, X_5 \equiv \sigma_z \tag{3.9}$$

where σ_x, σ_z are the Pauli operators and $\sigma_\theta \equiv \cos\theta\,\sigma_z + \sin\theta\,\sigma_x$. For this set of chosen observables and with θ chosen such that $\cos\theta = -3/4$, the correlation function takes the value [120]

$$\sum_{1\leq i<j\leq 5}\langle X_i X_j\rangle = -9/4 \tag{3.10}$$

which is the smallest possible value and violates the "pentagon" LG inequality given in Eq. (3.7).

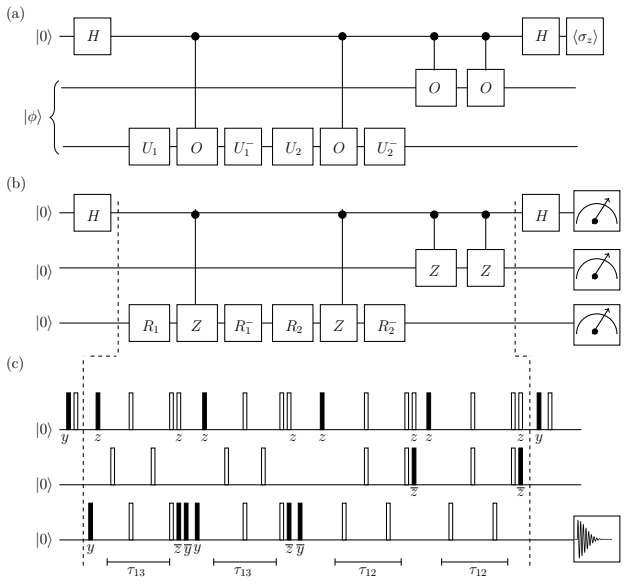

Figure 3.3: (a) Diagrammatic representation of a quantum scattering circuit that can measure the three-point correlation function $\langle A\alpha a\rangle$ associated to the PM inequality. Parameters corresponding to the circuit are defined as: $O = \sigma_z$, $U^{\pm}_{1,2} = e^{\mp i\sigma_y\theta/2}$ with $\theta = \pi/2$. (b) Quantum circuit representation in terms of rotation operators corresponding to above quantum scattering circuit. The different notation are defined as: $R^{\pm}_{1,2}$ equals to $(\frac{\pi}{2})_{\pm y}$, H represents Hadamard gates and Z corresponds to the rotations about the z axis. Corresponding (c) NMR pulse sequence representation with $\frac{\pi}{2}$ and π NMR pulses denoted by black and white rectangles, respectively. The time intervals τ_{12}, τ_{13} are equals to $\frac{1}{2J_{HF}}$ and $\frac{1}{2J_{HC}}$, respectively.

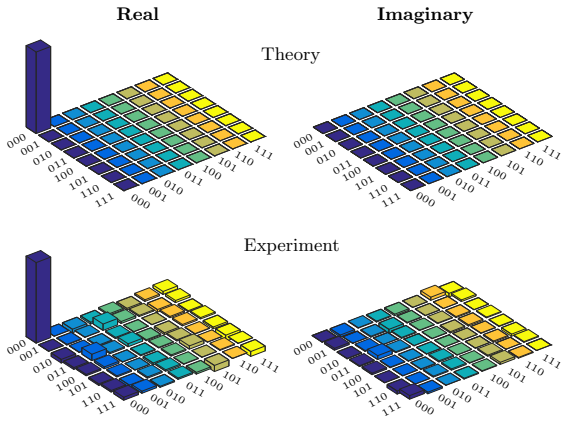

Figure 3.4: Tomographs of the input state $\rho = |0\rangle\langle 0| \otimes |00\rangle\langle 00|$ with an experimental state fidelity of 0.964±0.004.

3.4.2 Experimental violation of temporal Peres-Mermin inequality

A temporal equivalent of the KCBS inequality can be constructed similarly to the "pentagon LG" inequality by considering a set of nine dichotomic variables, and three successive measurements at two sequential times from the set of time points $t = \{t_1, t_2, ..t_5\}$. The observable set chosen is the "PM square" of nine dichotomous and mutually compatible observables $A, B, C, a, b, c, \alpha, \beta, \gamma$ [80]:

$$\begin{array}{lll} A = \sigma_z \otimes I, & B = I \otimes \sigma_z, & C = \sigma_z \otimes \sigma_z \\ a = I \otimes \sigma_x, & b = \sigma_x \otimes I, & c = \sigma_x \otimes \sigma_x \\ \alpha = \sigma_z \otimes \sigma_x, & \beta = \sigma_x \otimes \sigma_z, & \gamma = \sigma_y \otimes \sigma_y. \end{array} \tag{3.11}$$

Consider the combination of expectation values defined as follows:

$$\langle X_{\mathrm{PM}} \rangle = \langle ABC \rangle + \langle bca \rangle + \langle \gamma\alpha\beta \rangle + \langle A\alpha a \rangle + \langle bB\beta \rangle - \langle \gamma cC \rangle \tag{3.12}$$

If we make non-contextual assignments of values we get the inequality

$$\langle X_{\mathrm{PM}} \rangle \leq 4 \tag{3.13}$$

which is satisfied by all NCHV theories. This is the temporal PM inequality (X_{PM}) [80]. It has been shown that for a four-dimensional quantum system and a particular set of observables, a value of $\langle X_{PM} \rangle = 6$ is obtained for any quantum state, demonstrating state-independent contextuality [81].

We note here in passing that in this "PM square" set of measurements, each observable always occurs either in the first place or the second place or the third place in the sequential mean value. This inequality is violated whenever a joint probability

distribution cannot be found which assigns predetermined outcomes to the measurements X_i at all times $t_1 ... t_5$, and this violation is termed contextual in time. The system evolves under the action of a time-independent Hamiltonian $H = \hbar\omega\sigma_{x,y}$, which can be implemented in NMR using suitable rf pulses applied on the qubits. After state preparation, the probe qubit interacts with the system qubit via suitable unitaries. The temporal correlation functions are obtained by measuring the real part of the expectation value of z-component of the spin angular momentum of the probe qubit.

Our experimental task is to measure the expectation values of joint probabilities which are measured sequentially. To violate the temporal PM inequality we need to measure the three observables sequentially for any two-qubit state. We experimentally violated the PM inequality by measuring the six correlation functions using the generalized quantum scattering circuit. Fig. 3.3 shows the quantum scattering circuit, the operator decomposition and the corresponding NMR pulse sequence, to calculate the correlation function $\langle A\alpha a\rangle$ which is one of the six correlation function used in the PM temporal inequality. The PM temporal inequality is violated for any two-qubit state. The probe qubit is prepared in known $|0\rangle$ state and system qubit is prepared in $|\phi\rangle = |00\rangle$ state. The experimental tomograph of the state prepared in $\rho = |0\rangle\langle 0| \otimes |00\rangle\langle 00|$ is given in Fig 3.4, achieved with a fidelity of 0.964$\pm$0.004.

We apply the transformation given in Fig. 3.3, with suitable values of $O = \sigma_z$ and $\theta = \pi/2$. The correlation function $\langle A\alpha a\rangle$ for the $|\phi\rangle = |00\rangle$ state can be obtained by measuring the real part of the expected value of the z-component of the spin for the probe qubit. The other correlation functions involved in the PM temporal inequality are measured in a similar fashion. The mean value of the correlation functions and their error bars were calculated by repeating the experiment three times and the theoretically expected and experimentally calculated values are given in Table 3.1. The theoretically computed and experimentally measured values of the correlation functions agree well to within experimental errors. We experimentally violated the temporal PM inequality, obtaining $\langle X_{PM}\rangle_{\rm Expt} = 4.667 \pm 0.013$, showing the contextual nature of the measured expectation values.

3.4.3 Experimental violation of a Bell-type inequality corresponding to the temporal KCBS inequality

While it is clear that quantum correlations can violate spatial Bell-type and temporal LG-type inequalities, they do not go all the way to the values allowed by the no-signaling condition, and thus satisfy a bound called the Tsirelson's bound [126]. The reasons for the existence of such a bound which limits the algebraic values of the correlations between the measurement outcomes over and above the no-signaling condition, is still a matter of debate [127, 128]. We construct here an experimental situation

Table 3.1: Table listing the values of correlation functions corresponding to the PM inequality that have been theoretically calculated and experimentally measured.

Observables	Theoretical	Experimental
$\langle ABC \rangle$	1	0.928 ± 0.017
$\langle bca \rangle$	1	0.706 ± 0.012
$\langle \gamma\alpha\beta \rangle$	1	0.817 ± 0.010
$\langle A\alpha a \rangle$	1	0.685 ± 0.008
$\langle bB\beta \rangle$	1	0.755 ± 0.011
$\langle \gamma cC \rangle$	-1	-0.784 ± 0.019

where the maximum possible quantum correlation is achieved for four two-point correlation functions involved in the temporal KCBS inequality when it is re-interpreted as a Bell-type inequality [131].

The temporal KCBS noncontextual inequality can be constructed by considering a dichotomic variable X_t with successive measurements performed at two sequential times drawn from the time instants $t = \{t_0, t_1, ..., t_4\}$. The two-point temporal correlations thus obtained lead to the corresponding temporal KCBS inequality [131]:

$$\sum_{i=0}^{4} \langle X_{t_i} X_{t_{i+1}} \rangle \geq -3 \tag{3.14}$$

The violation of this inequality can be termed as contextuality in time. The temporal KCBS inequality can be transformed into a Bell-type inequality which tests the existence of a joint probability distribution for measurements on dichotomic variables, performed on subsystems A and B. The Bell-type inequality is given by [131]

$$\langle A_0 B_1 \rangle + \langle A_1 B_2 \rangle + \langle A_2 B_3 \rangle + \langle A_3 B_4 \rangle + \langle A_4 B_0 \rangle \geq -3 \tag{3.15}$$

where A_i and B_j are measured on the subsystems with the additional constraint that

$$\langle A_i B_i \rangle = 1 \ \text{ for all } \ i \tag{3.16}$$

which implies that the outcomes of pairs of measurements are the same. Violation of this inequality shows the non-existence of joint probability distribution for this scenario.

We experimentally demonstrated the violation of the Bell-type inequality given in Eq. (3.15) using the quantum scattering circuit on the same three-qubit system. Fig. 3.5(a) shows the quantum scattering circuit to calculate the correlation function

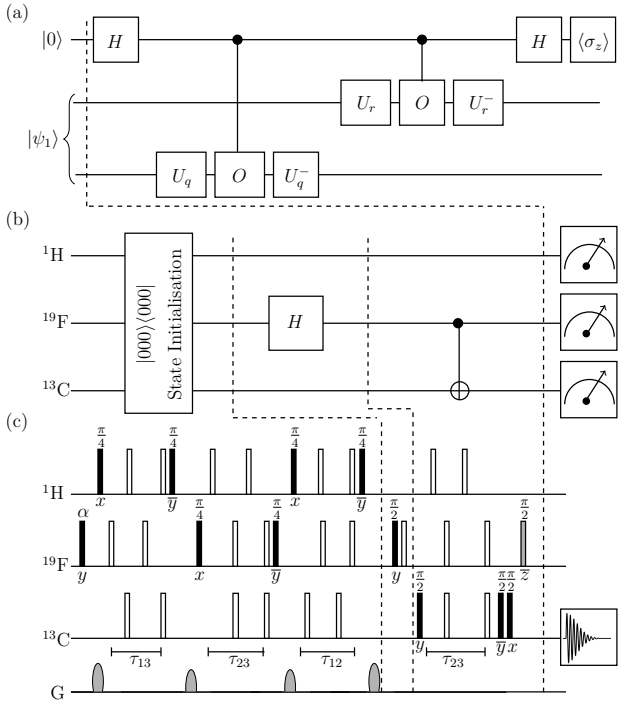

Figure 3.5: (a) Diagrammatic representation of a quantum scattering circuit that can measure the two-point correlation function $\langle A_r B_q \rangle$ used in the Bell-type inequality. The circuit parameters are defined as: $U_{r,q} = e^{\frac{-i2\pi r,q}{5}}$, $O = \sigma_z$ with $r, q = 0, 1, 2, 3, 4$. (b) Schematic circuit diagram for required quantum state and corresponding (c) NMR pulse sequence. The PPS $|000\rangle$ state (initial state) is prepared by using the series of pulses that come before the first dashed black line. The white rectangles represent the π pulses, while the phases and flip angles of the other pulses are listed next to each pulse. The time intervals τ_{12}, τ_{13}, τ_{23} equal to $\frac{1}{2J_{HF}}$, $\frac{1}{2J_{HC}}$, $\frac{1}{2J_{FC}}$, respectively.

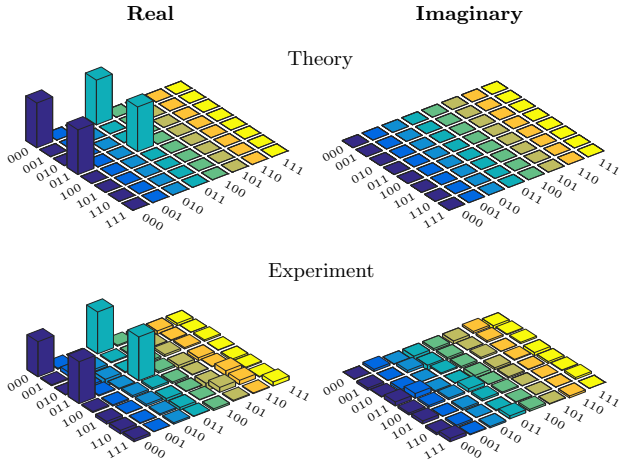

Figure 3.6: Tomographs of the state $\langle\psi_1| = \frac{1}{\sqrt{2}}(1,0,0,1,0,0,0,0)$ with an experimental state fidelity of 0.947±0.009.

$\langle A_r B_q\rangle$, involved in the Bell-type inequality on an eight-dimensional quantum system. For the violation of the Bell-type inequality, we used the ^{1}H as the probe qubit and ^{13}C and ^{19}F as the system qubits. We apply the transformations given in Fig. 3.5(a) with suitable values of $O = \sigma_z$ and $q, r = 0, 1, 2, 3, 4$.

The optimal violation of the Bell-type inequality can be obtained for the state $\langle\psi_1| = \frac{1}{\sqrt{2}}(1,0,0,1)$ with the probe qubit prepared in the state $|0\rangle$, and for the measurements $A_j = \sigma_j \otimes I$, $B_j = I \otimes \sigma_j$ where $j = 0, 1, 2, 3, 4$ and $\sigma_j = e^{i\frac{2\pi j}{5}\sigma_y}\sigma_z e^{-i\frac{2\pi j}{5}\sigma_y}$. The correlation functions $\langle A_r B_q\rangle$ for the state $\langle\psi_1| = \frac{1}{\sqrt{2}}(1,0,0,1)$ can be obtained by measuring the real part of the expected value of the spin z-component for the probe qubit. The corresponding quantum circuit for state preparation is shown in Fig. 3.5(b) and the NMR pulse sequence is shown in Fig. 3.5 (c). The sequence of pulses before the first dashed black line achieves state initialization into the $|000\rangle$ state. After this we apply the Hadamard gate (on ^{13}C), followed by a CNOT$_{23}$ gate, and the resultant state corresponds to $\rho_1 = |0\rangle\langle 0| \otimes |\psi_1\rangle\langle\psi_1|$ with $\langle\psi_1| = \frac{1}{\sqrt{2}}(1,0,0,1)$.

The tomograph of the state prepared in $\rho_1 = |0\rangle\langle 0| \otimes |\psi_1\rangle\langle\psi_1|$ with $\langle\psi_1| = \frac{1}{\sqrt{2}}(1,0,0,1)$ is given in Fig. 3.6 with an experimental fidelity of 0.947±0.009. The mean values of the correlation functions and their error bars were calculated by repeating the experiment three times and and calculated values are given in Table 3.2. As seen from the values tabulated in Table 3.2, the theoretically computed and experimentally measured values of the correlation functions agree well to within experimental errors. We have experimentally violated the Bell-type inequality with the violation of -3.755 ± 0.008.

It should be noted that there are no space-like separated measurements here. How-

Table 3.2: Theoretically computed and experimentally measured values of quantum correlations corresponding to the Bell-test.

Observables	Theoretical	Experimental
$\langle A_0 B_1 \rangle$	-0.809	-0.684 $\pm$ 0.014
$\langle A_1 B_2 \rangle$	-0.809	-0.754 $\pm$ 0.006
$\langle A_2 B_3 \rangle$	-0.809	-0.756 $\pm$ 0.011
$\langle A_3 B_4 \rangle$	-0.809	-0.746 $\pm$ 0.005
$\langle A_4 B_0 \rangle$	-0.809	-0.815 $\pm$ 0.004

ever, the inequality given in Eq. (3.15), with the constraint specified in Eq. (3.16), will be valid when the measurements on A and B are space-like separated and when the no-signaling principle is relevant. Our limited goal here is to show the possibility of maximally violating the Bell-type inequality given in Eq. (3.15).

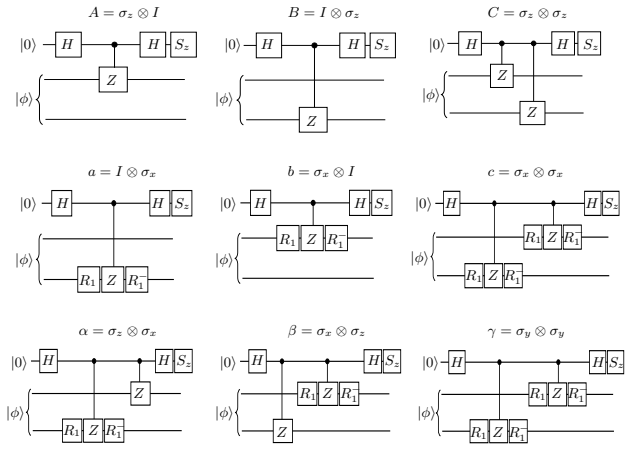

Figure 3.7: Individual quantum scattering circuits corresponding to measurements of the nine observables used in the PM inequality. Parameters are defined as: $R_l^{\pm} = e^{\mp \frac{iH\sigma_y}{\hbar}}$,$R_2^{\pm} = e^{\mp \frac{iH\sigma_x}{\hbar}}$, $S_z = \langle \sigma_z \rangle$.

3.4.4 Classical description of the experimental setup

All experimental tests of nonclassical properties of quantum correlations whether quantum contextuality, Bell nonlocality, or nonclassical temporal correlations, ultimately seek to disprove a classical theory, either local hidden variable models, or noncon-

Table 3.3: Table containing the theoretically computed and experimentally measured values of the each individual observables in their eigenstates.

Input State	Observables	Experimental (Theoretical)
$\|00\rangle$	$\sigma_z \otimes I$	$+ 0.945 \pm 0.026$ (+1)
$\|11\rangle$	$\sigma_z \otimes I$	$- 1.075 \pm 0.027$ (-1)
$\|00\rangle$	$I \otimes \sigma_z$	$+ 0.914 \pm 0.021$ (+1)
$\|11\rangle$	$I \otimes \sigma_z$	$- 0.901 \pm 0.015$ (-1)
$\|00\rangle$	$\sigma_z \otimes \sigma_z$	$+ 0.932 \pm 0.026$ (+1)
$\|10\rangle$	$\sigma_z \otimes \sigma_z$	$- 1.048 \pm 0.029$ (-1)
$\frac{\|00\rangle+\|01\rangle}{\sqrt{2}}$	$I \otimes \sigma_x$	$+ 0.969 \pm 0.025$ (+1)
$\frac{\|10\rangle-\|11\rangle}{\sqrt{2}}$	$I \otimes \sigma_x$	$- 0.993 \pm 0.026$ (-1)
$\frac{\|01\rangle+\|11\rangle}{\sqrt{2}}$	$\sigma_x \otimes I$	$+ 0.984 \pm 0.028$ (+1)
$\frac{\|01\rangle-\|11\rangle}{\sqrt{2}}$	$\sigma_x \otimes I$	$- 0.994 \pm 0.029$ (-1)
$\frac{\|00\rangle+\|11\rangle}{\sqrt{2}}$	$\sigma_x \otimes \sigma_x$	$+ 0.967 \pm 0.025$ (+1)
$\frac{\|00\rangle-\|11\rangle}{\sqrt{2}}$	$\sigma_x \otimes \sigma_x$	$- 0.97 \pm 0.027$ (-1)
$\frac{\|00\rangle+\|01\rangle}{\sqrt{2}}$	$\sigma_z \otimes \sigma_x$	$+ 1.067 \pm 0.023$ (+1)
$\frac{\|10\rangle+\|11\rangle}{\sqrt{2}}$	$\sigma_z \otimes \sigma_x$	$- 1.042 \pm 0.021$ (-1)
$\frac{\|00\rangle+\|10\rangle}{\sqrt{2}}$	$\sigma_x \otimes \sigma_z$	$+ 0.903 \pm 0.025$ (+1)
$\frac{\|01\rangle+\|11\rangle}{\sqrt{2}}$	$\sigma_x \otimes \sigma_z$	$- 0.975 \pm 0.027$ (-1)
$\frac{\|01\rangle+\|10\rangle}{\sqrt{2}}$	$\sigma_y \otimes \sigma_y$	$+ 1.001 \pm 0.012$ (+1)
$\frac{\|00\rangle+\|11\rangle}{\sqrt{2}}$	$\sigma_y \otimes \sigma_y$	$- 1.014 \pm 0.026$ (-1)

Table 3.4: Table containing the experimentally determined expectation values for every possible combination of each observables of the six sequences in order to verify their commutativity.

Observables	Experimental	Observables	Experimental	Observables	Experimental
$\langle A.B.C\rangle$	0.928 ± 0.017	$\langle b.c.a\rangle$	0.706 ± 0.012	$\langle \gamma.\alpha.\beta\rangle$	0.817 ± 0.010
$\langle A.C.B\rangle$	0.935 ± 0.012	$\langle b.a.c\rangle$	0.723 ± 0.010	$\langle \gamma.\beta.\alpha\rangle$	0.839 ± 0.012
$\langle B.A.C\rangle$	0.919 ± 0.009	$\langle a.b.c\rangle$	0.725 ± 0.019	$\langle \alpha.\beta.\gamma\rangle$	0.829 ± 0.010
$\langle B.C.A\rangle$	0.935 ± 0.008	$\langle a.c.b\rangle$	0.707 ± 0.015	$\langle \alpha.\gamma.\beta\rangle$	0.799 ± 0.018
$\langle C.A.B\rangle$	0.929 ± 0.012	$\langle c.a.b\rangle$	0.733 ± 0.018	$\langle \beta.\alpha.\gamma\rangle$	0.824 ± 0.014
$\langle C.B.A\rangle$	0.908 ± 0.010	$\langle c.b.a\rangle$	0.719 ± 0.017	$\langle \beta.\gamma.\alpha\rangle$	0.796 ± 0.016
$\langle A.\alpha.a\rangle$	0.685 ± 0.008	$\langle b.B.\beta\rangle$	0.755 ± 0.011	$\langle \gamma.c.C\rangle$	-0.784 ± 0.019
$\langle A.a.\alpha\rangle$	0.672 ± 0.017	$\langle b.\beta.B\rangle$	0.726 ± 0.019	$\langle \gamma.C.c\rangle$	-0.813 ± 0.010
$\langle \alpha.A.a\rangle$	0.671 ± 0.018	$\langle B.b.\beta\rangle$	0.776 ± 0.017	$\langle C.\gamma.c\rangle$	-0.760 ± 0.020
$\langle \alpha.a.A\rangle$	0.644 ± 0.020	$\langle B.\beta.b\rangle$	0.779 ± 0.009	$\langle C.c.\gamma\rangle$	-0.811 ± 0.012
$\langle a.A.\alpha\rangle$	0.714 ± 0.017	$\langle \beta.B.b\rangle$	0.776 ± 0.015	$\langle c.C.\gamma\rangle$	-0.771 ± 0.019
$\langle a.\alpha.A\rangle$	0.639 ± 0.019	$\langle \beta.b.B\rangle$	0.746 ± 0.019	$\langle c.\gamma.C\rangle$	-0.789 ± 0.013

textual or macrorealist theories. Hence any experimental test of quantum correlations must subsume a classical description of the setup and one should be able to associate a measurement procedure to any classical variable using this setup. For instance, in order to measure the correlator $\langle AB\rangle$ one should in principle be able to measure A and B independently.

Throughout in our analysis, we have considered expectation values of products of observables to show that a quantum description may violate bounds derived from classical ideas of assignment of outcomes to individual measurements. As mentioned above, it is important to be able to measure the observables one by one, where it is possible to imagine assigning outcomes from a classical description. To provide the possibility of a classical description of our experimental setup, we validate the following assumptions: (i) that each of the nine observables involved in the PM inequality can be measured individually and has the eigenvalue ± 1; and (ii) that the observables involved in the sequences of the PM inequality are mutually compatible.

We first check that each observable in the PM inequality has the eigenvalue ± 1. To do so, we measure the expectation values of the nine individual observables using the quantum scattering circuit given in Fig. 3.7. The input states are prepared in the

eigenstates of each of the nine observables involved in the PM inequality. Table III contains a comparison of the experimentally observable expectation values of each observables with its theoretically expected value of ± 1.

We then proceed to check the second assumption that the measurements in the six sequences involved in the PM inequality are commutative i.e. each of the observables is context-independent. We do this by switching the measurement sequence in the the scattering circuit. Table IV contains the experimentally calculated expectation values of all possible combinations of each observable in the six sequences involved in the PM inequality.

3.5 Conclusions

We designed and experimentally implemented a generalized quantum scattering circuit to measure an n-point correlation function on an NMR quantum information processor, with an observable being measured sequentially at these n time instants. We experimentally demonstrated the violation of a temporal noncontextuality PM inequality using three NMR qubits, which involved performing sequential noninvasive measurements. The generalized quantum scattering circuit we have constructed is independent of the quantum hardware used for its implementation and can be applied to systems other than NMR qubits. Our work asserts that NMR quantum processors can serve as optimal test beds for testing such inequalities. Results of this chapter are contained in Phys. Rev. A **105**, 022216 (2022).

Chapter 4

Simulation of maximal non-locality using a three-qubit entangled state on an NMR quantum simulator

4.1 Introduction

Entanglement is thought to be the most fundamental non-classical aspect of quantum theory, noticed in 1935 [112]. As entanglement serves as the primary resource of quantum information processing, it is crucial to create, identify, and protect entangled states [11]. In quantum theory, detecting entanglement is typically a challenging issue. Different methods for revealing the entanglement have been proposed [49, 145, 146, 147]. The full characterization of entanglement, despite the existence of sufficient criteria for entanglement identification of quantum states in higher dimensional Hilbert spaces, is still a work in progress. Extensive research has been conducted on three-qubit entanglement, proving that there are two different ways in which three qubits can be entangled [148, 149]. One of the foundational concepts in physics is symmetry, and in quantum theory, the permutation symmetry corresponding to multipartite quantum systems is equivalent to a natural symmetry. Studies on the entanglement of symmetric states of multipartite systems have been conducted in-depth [150]. Several quantum informational tasks have benefited from the usage of permutation symmetric entangled states, which maintain their invariance through pair-wise qubit swapping [151, 152, 153]. The geometric measure of entanglement, which resembles a measure of distance, describes the entanglement of symmetric multipartite states [154, 155]. In order to achieve the permutation symmetric entangled states, quantum circuits were developed [156].

4. Simulation of maximal non-locality using a three-qubit entangled state on an NMR quantum simulator

A crucial aspect of experimental quantum computing is the generation and detection of diverse multipartite entangled states. Several experimental schemes for three-qubit entanglement have been carried out experimentally using an NMR quantum processor. The experimental construction of a canonical form for generic three-qubit states has been performed, which are capable of generating three-qubit entangled states such as W and GHZ states [157]. In another NMR experiment, a three-qubit $\mathrm{W}\bar{\mathrm{W}}$ entangled state was created, demonstrating that even though $\mathrm{W}\bar{\mathrm{W}}$ state belongs to the same entanglement class as the GHZ state, it encodes information about multipartite correlations entirely differently [158]. Decoherence of tripartite entangled states has been studied using the dynamical coupling method on an NMR experimental setup. The findings indicate that whereas the states corresponding to the W-class are the most robust against the experimental noise, the GHZ-class states are the most fragile [159].

Nonlocality describes the ability of the observers to produce instantaneous effects over specially separated systems. Quantum theory follows the notion of nonlocality, which is inconsistent with the theories which follow the notion of locality such as hidden variable theories [55]. As discussed in previous chapters, the violation of Bell inequality like the Clauser-Horne-Shimony-Holt (CHSH) inequality demonstrates the existence of nonlocality [160]. Nonlocality has immense application in the field of secure communication [161], and information theory [162]. The violation of Bell-type inequalities was demonstrated for the GHZ, Cluster, and W states using the N-partite generalization of Wigner's hypothesis [57]. The violation of CHSH inequalities in a tripartite scenario has been used to characterize nonlocality [163, 164, 165]. For the nonlocal correlations to exist, the state has to be entangled [166]. Various studies have been conducted to determine what kind of entanglement causes the maximum quantum violation of Bell-type inequalities, which reveals the maximum nonlocality [167, 168, 169].

The existence of incompatibility measurements, another key aspect of quantum theory, demonstrates the fundamental departure from classical theory [170]. Studies have demonstrated the necessity of incompatibility measurements in order to violate the Bell-type inequality [171, 172, 173]. The quantification of measurement incompatibility has been investigated in relation to Bell nonlocality [174]. The significance of the entanglement and incompatibility has been studied separately for the nonlocality. There exist scenarios where the entanglement and incompatibility are combined to obtain the maximum nonlocality by obtaining the maximum violation of Bell inequalities [76]. It has been demonstrated that for the maximal incompatible local measurements, there exists a maximal quantum violation of tight Bell inequality for a few entangled states such as Bell state, GHZ state, and $|\mathrm{S}\rangle$ state [118, 175]. Experimental demonstrations of the tight Bell-inequalities have been performed on different experimental set-ups [176, 177, 178, 179].

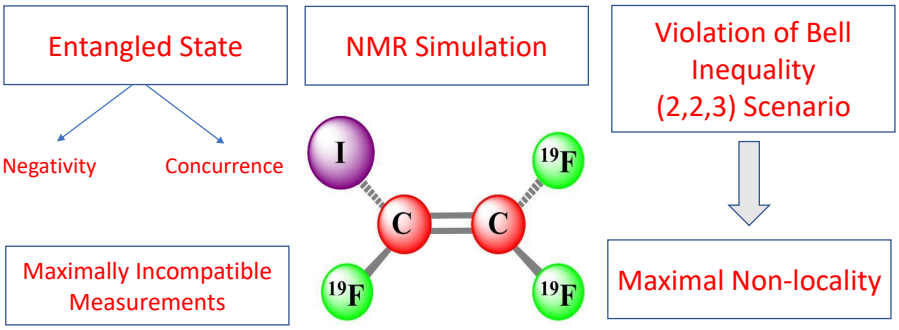

Figure 4.1: Scheme to experimentally simulate the violation of a tight Bell-inequality using the tripartite entangled $|\mathrm{S}\rangle$ state.

In this chapter, we use the NMR experimental set-up to experimentally design and construct the quantum circuit for the three-qubit $|\mathrm{S}\rangle$ entangled state, involved in the tight Bell inequality. By experimentally computing the two entangled measures, namely concurrence and negativity, the entanglement of $|\mathrm{S}\rangle$ state is validated. Further, we use this $|\mathrm{S}\rangle$ state to experimentally simulate the violation of tight Bell inequality, This tight Bell ineqaulity corresponds to the inequality number 26 in Sliwa's classification in the $(3, 2, 2)$ scenario [76]. Additionally, by including compatible measures in the existing measurement configuration, maximum incompatibility was examined. The methodology used in this chapter is depicted in Fig. 4.1. It should be highlighted that we referred to our experimental demonstration as a simulation as the NMR experiments are not suitable for the non-local scenario which require spacelike separated events. In an NMR experimental set-up, the nuclear spins of the atoms in a single molecule, serve as the qubits. The separation between the NMR qubits is of the order of a few angstroms and are suitable for the local scenario [180].

4.2 The Bell inequality in the (3, 2, 2) scenario

A Bell inequality is tight when it corresponds to the facet of the local polytope which is generated by the local-realistic joint probabilities model [160]. Quantum nonlocality has been classified according to the combinations of entangled states and incompatible measurements for 46 classes of tight Bell inequalities in the $(3, 2, 2)$ scenario [76]. The

inequality number 26 in Sliwa's classification scheme is given by:

$$\begin{aligned} T_{26} = &\langle A_0\rangle + \langle B_0\rangle + \langle A_0B_0\rangle + 2\langle A_1B_1\rangle + \langle C_0\rangle \\ &+ \langle A_0C_0\rangle + \langle B_0C_0\rangle - \langle A_0B_0C_0\rangle - 2\langle A_1B_1C_0\rangle \\ &+ 2\langle A_1C_1\rangle - 2\langle A_1B_0C_1\rangle - 2\langle B_1C_1\rangle \\ &+ \langle A_0B_1C_1\rangle \leq 5 \end{aligned} \tag{4.1}$$

where A_i, B_i, C_i are the measurement settings of the first, second and third party, respectively. Each observable is dichotomous and can have ± 1 outcomes. The maximum quantum violation of the inequality number 26 in Sliwa's classification scheme is achieved using the entangled $|\mathrm{S}\rangle$ state given in Eq. 4.2 [181].

Three-qubit entanglement with genuine three-party entanglement, has been well studied and falls into one of the two inequivalent classes namely, the GHZ class and the W class [148]. The $|\mathrm{S}\rangle$ state which is a three-qubit permutation-symmetric entangled state, has been defined as [76]:

$$|\mathrm{S}\rangle = \frac{1}{\sqrt{6}}(|001\rangle + |010\rangle - |100\rangle) + \frac{1}{\sqrt{2}}|111\rangle \tag{4.2}$$

The $|\mathrm{S}\rangle$ belongs to the W class of states and therefore is inequivalent to the GHZ state under local operations and classical communication (LOCC). The qubit-qubit concurrences for this state are all equal to 0.244, as opposed to the W state whose qubit-qubit concurrences are all equal to 0.667 [178]. The $|\mathrm{S}\rangle$ state has interesting properties and as we shall see, plays an important role in the context of violation of Bell's inequalities for the $(3, 2, 2)$ scenario.

For the particular set of observables $A_0 = B_0 = C_0 = \sigma_z$ and $A_1 = B_1 = C_1 = \sigma_x$ which are maximally incompatible according to any quantifier of incompatibility, the $|\mathrm{S}\rangle$ state produces the maximum quantum violation given by [76]:

$$T_{26} = 1 + 4\sqrt{3} \approx 7.928 \tag{4.3}$$

4.3 Experimental construction of $|\mathrm{S}\rangle$ state and violation of Bell inequality

4.3.1 Experimental details

We used the molecule iodotrifluoroethylene dissolved in acetone-d6 with the three (^{19}F) spins encoding the three NMR qubits. The molecular structure and other experimental details are given in Ref. [159]. The three-qubit Hamiltonian in a rotating frame

is given by:

$$H = -\sum_{i=1}^{3}(\omega_i - \omega_{RF})I_{iz} + \sum_{i>j,j=1}^{3} 2\pi J_{ij} I_{iz} I_{jz} \tag{4.4}$$

where I_{iz}, ω_i, J_{ij} denote the spin angular momentum operator, the Larmor frequencies, and the scalar coupling constants, respectively. The first term in the Hamiltonian represents the Zeeman interaction between the spins and the applied static magnetic field, while the second term represents the interaction term. More details are provided in Ref. [9].

The NMR experiments were performed at room temperature and the system was initialized in a pseudopure (PPS) state, which mimics a pure state [9, 39]. The PPS state $|000\rangle$ was achieved via the spatial averaging technique [182] with the density operator being given by:

$$\rho_{000} = \frac{1-\epsilon}{8} I_8 + \epsilon |000\rangle\langle 000| \tag{4.5}$$

where I_8 is the 8×8 identity operator and ϵ is proportional to the spin polarization which is $\approx 10^{-5}$ at room temperature.

The NMR pulse sequence for preparing the PPS state $|000\rangle$ can be found in Ref. [159] which gives details of the specific sequence of RF pulses, four Z gradient pulses, and three time evolution periods that are used. We used the Gradient Ascent Pulse Engineering (GRAPE) technique [183, 184] for the optimization of all the RF pulses used to construct the PPS state. The GRAPE optimized RF pulses are robust against RF inhomogeneity, with an average fidelity of ≥ 0.999. We used four GRAPE pulses $(U_{P1}, U_{P2}, U_{P3}, U_{P4})$ optimized to reach the PPS state from the thermal state, where some RF pulses were combined into a single pulse. The duration of pulses U_{P1}, U_{P2}, U_{P3}, U_{P4} are $500\ \mu s$, $9000\ \mu s$, $7500\ \mu s$, $4000\ \mu s$ respectively. The experimental state was reconstructed using a least squares constrained convex optimization technique [185]. The set of tomographic operations $\{III, IIY, IYY, YII, XYX, XXY, XXX\}$ where the $X(Y)$ denotes the single spin operator implemented by a spin-selective $\frac{\pi}{2}$ pulse and I denotes no operation were performed to reconstruct the final density operator. All the seven tomography spin selective pulses were optimized using GRAPE with the length of each pulse being $\approx 500\mu s$. The PPS state $|000\rangle$ had an experimental state fidelity of 0.997.

4.3.2 Experimental construction of the $|\mathrm{S}\rangle$ state

After preparing the PPS state, we turn to the experimental preparation of the tripartite $|\mathrm{S}\rangle$ state on the three-qubit NMR system. The quantum circuit to prepare the $|\mathrm{S}\rangle$ state starting from the PPS $|000\rangle$ state is given in Fig. 4.2. The quantum circuit contains

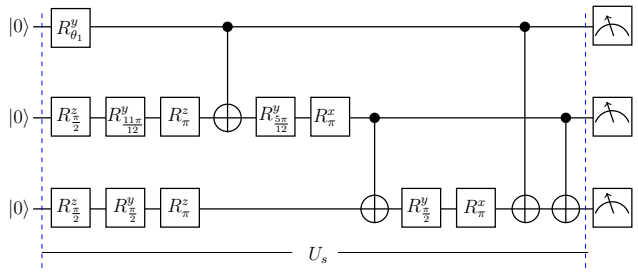

Figure 4.2: Diagrammatic representation of the quantum circuit used to create the $|\mathrm{S}\rangle$ state. The full unitary, U_s, includes all quantum gates needed for state preparation.

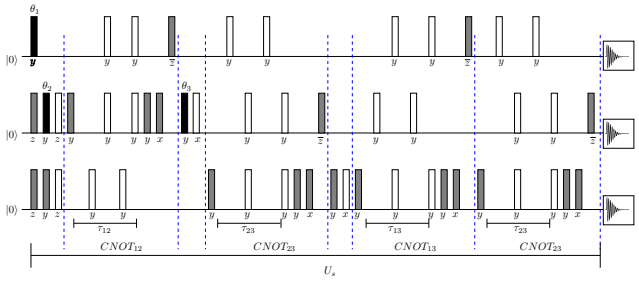

Figure 4.3: Representation of sequence of NMR pulses capable of constructing the required $|\mathrm{S}\rangle$ state. $\frac{\pi}{2}$ rotations are represented by grey rectangles, while π rotations are represented by empty rectangles. The other RF pulse rotations such as $\theta_1 = \frac{1.216\pi}{2}$, $\theta_2 = \frac{11\pi}{12}$ and $\theta_2 = \frac{5\pi}{12}$ are represented by black rectangles. The intervals are set to $\tau_{12} = \frac{1}{2J_{12}}$, $\tau_{13} = \frac{1}{2J_{13}}$, $\tau_{23} = \frac{1}{2J_{23}}$ with $J_{12} = 69.65$ Hz, $J_{13} = 47.67$ Hz, $J_{23} = -128.23$ Hz. Each CNOT gates pulses are divided by dotted lines, and the total sum of all the gates is represented by a single unitary U_s.

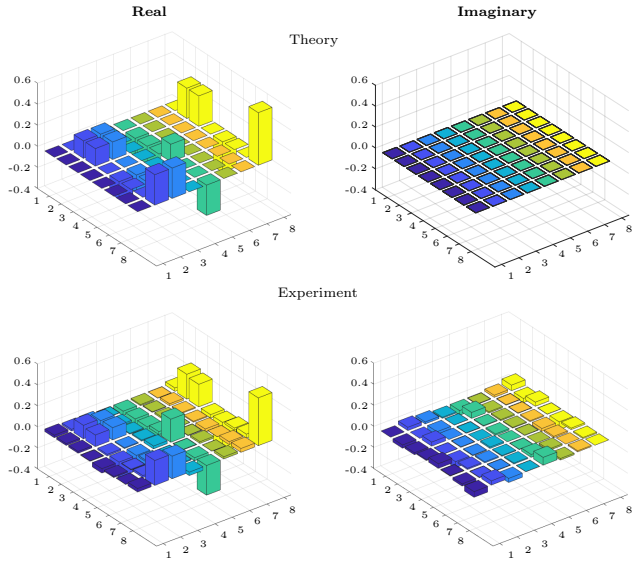

Figure 4.4: The tomographs of the $|\mathrm{S}\rangle$ state representing the theoretically simulated and experimentally observed values. The numbers $1, 2, 3..., 8$ stand for the binary-coded rows and columns that form the computational basis, ranging from $|000\rangle$ to $|111\rangle$.

several one-qubit gates and two-qubit gates. The NMR pulse sequence corresponding to the quantum circuit is shown in Fig. 4.3. All the NMR pulses were numerically optimized using the GRAPE algorithm and we were able to achieve high gate fidelities with relatively small RF pulse durations. The unitary operator for the entire preparation sequence of Fig. 4.3 contains four CNOT gates and eleven non-selective rotations; the entire unitary was generated by a specially crafted single GRAPE pulse U_s having a duration of $\approx 4600\mu s$.

To check the quality of the prepared $|\mathrm{S}\rangle$ state, state tomography was performed using the least squares optimization technique and an experimental state fidelity of 0.949 ± 0.003 was obtained. The tomographs of the $|S\rangle\langle S|$ state are shown in Fig. 4.4.

4.3.3 Entanglement verification of the $|\mathrm{S}\rangle$ state

Next, we experimentally verified the entanglement of the $|\mathrm{S}\rangle$ state. To quantify entanglement, we used the well-known tripartite negativity measure [54]. The tripartite negativity can be calculated using the bipartite negativity, where bipartite negativity is the absolute value of the sum of the negative eigenvalues of ρ^{T_A} with T_A denoting the partial transpose of ρ with respect to the subsystem A in the bipartition $A|BC$. Negativity is zero if the partial transpose ρ^{T_A} has no negative eigenvalues. Tripartite negativity N then becomes $(N_{A|BC}N_{B|AC}N_{C|BA})^{\frac{1}{3}}$. It ranges from 0 for a separable

state to 1 for a maximally entangled state. We computed the tripartite negativity for the experimentally prepared $|\mathrm{S}\rangle$ state and obtained $N = 0.794 \pm 0.015$, which is close to the theoretically predicted value of 0.943. This clearly shows the presence of tripartite entanglement in the $|\mathrm{S}\rangle$ state.

We also verified the entanglement of the $|\mathrm{S}\rangle$ state by using another entanglement measure termed qubit-qubit concurrence [53]. The concurrence is calculated from the eigenvalues $\lambda_1 \geq \lambda_2 \geq \lambda_3 \geq \lambda_4$ of the matrix $R = \rho(\sigma_y \otimes \sigma_y)\rho^*(\sigma_y \otimes \sigma_y)$ where σ_y is the Pauli matrix and ρ and ρ^* denote the density matrix and its complex conjugate, respectively. The qubit-qubit concurrence is given by C(ρ) = max$(0, \sqrt{\lambda_1} - \sqrt{\lambda_2} - \sqrt{\lambda_3} - \sqrt{\lambda_4})$. The bipartite concurrence ranges between 0 and 1, with 0 implying no entanglement is present in the system and 1 indicating maximal entanglement. The experimental values we obtained for the qubit-qubit concurrence, range from $\approx 0.094 - 0.32$, which verifies the presence of entanglement in the $|\mathrm{S}\rangle$ state.

4.3.4 Non-locality inequality violation

The experimentally prepared $|\mathrm{S}\rangle$ state was used to test the inequality T_{26} defined in Eq. 4.1. The numerical value of the experimental violation we obtain is:

$$T_{26} = 6.531 \pm 0.125 \tag{4.6}$$

where the observables $A_0 = B_0 = C_0 = \sigma_z$ and $A_1 = B_1 = C_1 = \sigma_x$ are maximally incompatible for each of the three parties.

In addition, we checked the maximal incompatibility of the observables of the three parties by changing one of the observables out of the six local measurements while leaving the other five in their initial configuration. These measurement modifications led to a decrease in the inequality value of T_{26}, fulfilling the requirement of maximal incompatibility in the three parties for the T_{26} scenario.

4.4 Conclusions

In this chapter, we experimentally prepared a genuinely entangled three-qubit state ($|\mathrm{S}\rangle$) on an NMR quantum processor, and certified its entanglement using two different entanglement measures namely, negativity, and qubit-qubit concurrence. We used the $|\mathrm{S}\rangle$ state to experimentally simulate the maximum quantum violation of a tripartite tight Bell inequality. Our results show a clear violation of the tight Bell inequality, revealing the maximally non-local nature of the state. We also tested the maximal incompatibility of the observables by modifying one of the six observables. An NMR quantum processor is a good testbed to perform tests of foundational issues in quantum

mechanics. Our results are a step forward in the direction of unearthing deeper connections between nonlocality, entanglement, and incompatibility. The results described in this chapter are available in arXiv:2206.12870v1.

4. Simulation of maximal non-locality using a three-qubit entangled state on an NMR quantum simulator

Chapter 5

NMR simulation of monogamy relationship between quantum contextuality and nonlocality

5.1 Introduction

Nonlocality and contextuality, the fundamental properties of quantum theory, have been extensively discussed in earlier chapters. Nonlocality and contextuality can be revealed via the violation of CHSH and KCBS inequalities, respectively. It is crucial to address the issue of whether it is conceivable to see both nonlocality and quantum contextuality at the same time. Monogamy is the trade-off between the Bell or noncontextual inequalities [66, 186]. It was discovered that a monogamous relation between contextuality and nonlocality is imposed by the quantum no-disturbance principle i.e. nonlocality and contextuality can not be observed simultaneously. These two fundamentally quantum phenomena were investigated separately for many years, however it has recently been demonstrated that contextuality and nonlocality can be examined together [187].

The fundamental monogamy relation between the nonlocality and contextuality has been derived using the graphical theoretic approach [188]. Different types of monogamous relationships, including monogamy of two KCBS inequalities [66], monogamy of two Bell inequalities [189], and monogamy of Bell and KCBS inequalities [190], have been presented using various scenarios. The no-disturbance concept, commonly referred to as the no-signaling principle for parties who are physically separated, is supported by QM [66]. The no-disturbance and no-signaling concept is the foundation for the development of a monogamous relationship between the noncontextuality and

Bell inequality [67]. Experimental simulation of such monogamy relation of noncontextuality and nonlocality has been proposed [191]. There are a variety of applications in which monogamous relationships are used, including QKD protocols [192], causality quantification [193], and local realism studies [194].

A photonic qutrit-qubit system has been used to illustrate the experimental test of the monogamous relationship between contextuality and nonlocality [71]. In this chapter, we experimentally simulated the monogamous relationship between contextuality and nonlocality on an NMR quantum information processor using a hybrid ququart-qubit system. We first present experimental proof of the monogamous relationship between contextuality and nonlocality. We further show that a quantum barrier exists and that it satisfies the no-disturbance principle at a single location, within the bounds of the experiment. The required ququart-qubit system was realized by the ^{13}C-labeled diethyl fluoromalonate molecule, a three-qubit system. The hybrid ququart-qubit system is achieved by merging the first two qubits into a single system with a four-dimensional Hilbert space. After preparing the hybrid ququart-qubit state the expectation values, involved in the monogamy inequality, were calculated by mapping the decomposed observables into single qubit operator. For eight alternative ququart-qubit input states, the values of the monogamous inequality between contextuality and nonlocality have been determined. In passing, we should mention that since the NMR qubits are actually the nuclear spins of atoms bonded together in a single molecule, separated by a few angstroms [195], we considered our test as a "simulation." The scheme used to calculate the monogamy relation of contextuality and nonlocality, in this chapter is depicted in Fig. 5.1. The monogamy relationship has been demonstrated experimentally as the violation of KCBS inequality for ququart state forbids the violation of CHSH inequality for the entangled ququart-qubit state. Our findings provide experimental evidence of the trade-off between the contextuality and nonlocalty, imposed by no-disturbance principle.

5.2 Monogamy relation between contextuality and nonlocality

Kurzynski *et. al.* [196] proposed a fundamental monogamy relation between the KCBS inequality and the CHSH inequality which is based on the no-disturbance quantum principle. Consider two spatially separated systems B and C. Two compatible dichotomous (*i.e.* having only two possible outcomes ± 1) observables are randomly chosen from a set of five observables $\{C_i\}, i = 1..5$ and measured on the system C. Similarly, for the system B, two incompatible dichotomous observables B_1, B_2 are chosen and performed. Fig. 5.2 illustrates a schematic of the compatibility relations

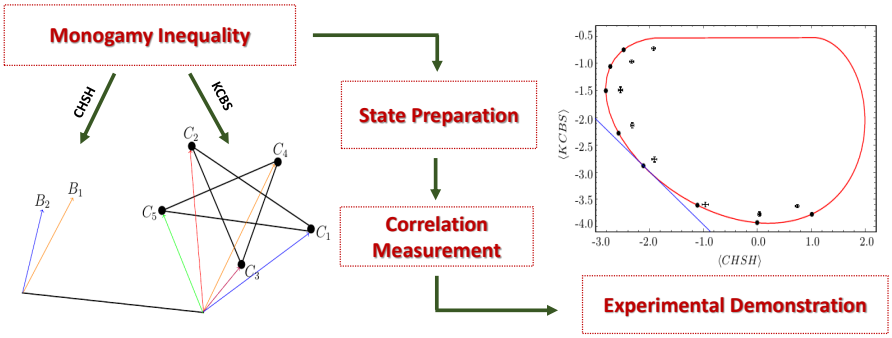

Figure 5.1: Scheme used to experimentally simulate the monogamy relationship between contextuality and nonlocality.

between the seven observables (five on system C and two on system B).

Quantum contextuality can be tested on the system C via the KCBS inequality given by

$$\mathcal{K}_{\mathfrak{e}} = \langle C_1 C_2 \rangle + \langle C_2 C_3 \rangle + \langle C_3 C_4 \rangle + \langle C_4 C_5 \rangle + \langle C_5 C_1 \rangle \geq -3. \tag{5.1}$$

where the violation of this inequality implies that the correlations cannot be captured using a noncontextual hidden variable (NCHV) model. The maximum violation of the KCBS inequality is $5 - 4\sqrt{5}$.

The CHSH inequality is given by:

$$\beta_{CB} = \langle C_1 \otimes B_1 \rangle + \langle C_1 \otimes B_2 \rangle + \langle C_4 \otimes B_1 \rangle - \langle C_4 \otimes B_2 \rangle \geq -2. \tag{5.2}$$

and the violation of this inequality implies that the correlations cannot be captured using a local hidden variable (LHV) model. The maximum violation for the CHSH inequality is $-2\sqrt{2}$. The classical bounds of both the KCBS and CHSH inequalities can be violated separately due to the lack of a joint probability distribution.

Quantum theory imposes a strict monogamy relation between NCHV and LHV models by restricting values of $\mathcal{K}_{\mathfrak{e}}, \beta_{CB}$ to a region in the parametric space bounded by the KCBS and CHSH inequalities. The ND principle leads to a non-trivial tradeoff between the violation of CHSH and KCBS inequalities:

$$\beta_{CB} + \mathcal{K}_{\mathfrak{e}} \geq -5 \tag{5.3}$$

The monogamy relation between these two inequalities posits that the violation of one inequality in turn forbids the violation of the other inequality. The bound on maximal violation arises due to the ND principle. This additional monogamy relation makes the quantum region smaller than the ND principle bounded region.

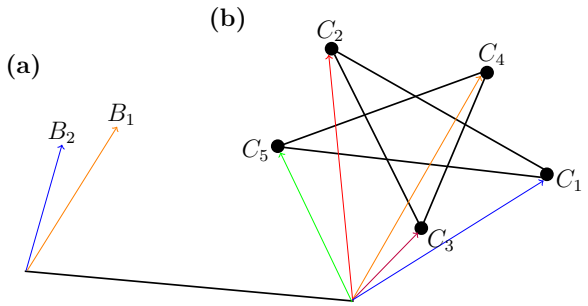

Figure 5.2: Graphical representation of measurement setting corresponding to the B and C spatially separated systems. (a) The two distinct directions represent the measurements corresponding to the qubit system B. Similarly, (b) the five distinct directions represent the measurements corresponding to the ququart system C. The connection between the observables are defined as: C_i are compatible with C_{i+1} are when it is connected by black edge and each C_i is compatible with The B_1 and B_2 observables.

Consider the scenario of the combined ququart-qubit system with basis states $\{|00\rangle, |01\rangle, |10\rangle\}$ and $\{|0\rangle, |1\rangle\}$, respectively. Measurements can be made of the five observables $C_i = 2|u_i\rangle\langle u_i| - I$ where $i = 1, ..., 5$ and the state $|u_i\rangle$ can be written as:

$$|u_i\rangle \propto \left[\cos\frac{4\pi i}{5}|00\rangle + \sin\frac{4\pi i}{5}|01\rangle + \sqrt{\cos\frac{\pi}{5}}|10\rangle\right] \tag{5.4}$$

For the CHSH scenario, the observables are chosen to be $B_1 = \sigma_z$ and $B_2 = \sigma_x$. The restriction of possible values of $\beta_{CB}, \mathcal{K}_{\mathfrak{C}}$ within the parametric space spanned by the value of these inequalities, quantum theory shows the additional monogamy relation between NCHV and LHV. The boundary of the quantum state is more interesting because the more stringent monogamy relation makes the quantum region smaller than that imposed by the ND.

The boundary of the quantum region can be produced by taking unnormalized states of the form:

$$|\psi_\phi\rangle = f(\phi)|001\rangle + g(\phi)|010\rangle + |101\rangle \tag{5.5}$$

where

$$\begin{aligned} f(\phi) &\approx -0.05 + 0.15\cot\phi - 0.57\tan\phi \\ g(\phi) &\approx 0.72 + 0.32\cot\phi + 0.26\tan\phi \end{aligned} \tag{5.6}$$

By choosing particular values of the states $|\psi_\phi\rangle$ ($\phi = -0.27$) such that the lower bound of $\beta_{CB} + \mathcal{K}_{\mathfrak{C}}$ is minimized, the inequality becomes an equality. The quantum boundary

touches the ND boundary at a single point where the average values of the operators are $\langle \mathrm{CHSH} \rangle \approx -2.89$ and $\langle \mathrm{KCBS} \rangle \approx -2.11$, respectively. The monogamy relation holds even in the extreme cases *i.e.* when both inequalities are not violated simultaneously.

5.3 Experimental realization of monogamy relation between contextuality and nonlocality

5.3.1 Experimental setup

To experimentally implement the KCBS and CHSH inequalities on a ququart and a qubit-ququart system, we used the molecule of ^{13}C-labeled diethyl fluoromalonate dissolved in acetone-D6 as an eight-dimensional quantum system, with the ^{1}H, ^{19}F and ^{13}C spin-1/2 nuclei being encoded as the three qubits. The three-qubit system can be reinterpreted as a ququart-qubit bipartite system by clubbing the first two qubits into a single system with a four-dimensional Hilbert space, with the four ququart basis vectors being mapped to the logical state vectors ($\{|00\rangle, |01\rangle, |10\rangle, |11\rangle\}$) of the first and second qubits. Experiments were performed at on a Bruker Avance III 600-MHz FT-NMR spectrometer equipped with a QXI probe. Local unitary operations were achieved by the rf pulses of suitable amplitude, phase, and duration and nonlocal unitary operations were achieved by free evolution under the system Hamiltonian. The T_1 and T_2 relaxations of ^{1}H, ^{19}F, ^{13}C spin-1/2 nuclei ranges from 4.16 sec to 7.16 sec and 0.99 sec to 3.56 sec, respectively. The durations of the $\frac{\pi}{2}$ pulses for ^{1}H, ^{19}F, and ^{13}C nuclei were 9.36 μs at 18.14 W power level, 23.4 μs at a power level of 42.27 W, and 15.8 μs at a power level of 179.47 W, respectively.

5.3.2 Experimental test of monogamy relation

To experimentally demonstrate the simulation of the monogamy relation between the KCBS and CHSH inequality, we started with initializing the system into the pure state. At room temperature, NMR experiments are only sensitive to the deviation density matrix and the initial state is prepared from the thermal equilibrium into a pseudo-pure state (PPS) i.e. $|000\rangle$ state. The PPS is prepared using spatial averaging technique which is based on dividing the system in sub-ensembles and these sub-ensembles can be accessed independently in NMR by using a combination of rf pulses and pulsed magnetic gradients. After preparing the PPS state, we prepared the states $|\psi_\phi\rangle$ and calculated the average values of $\langle \mathrm{KCBS} \rangle$ and $\langle \mathrm{CHSH} \rangle$ inequalities for different values of ϕ.

To experimentally demonstrate the simulation of the monogamy relation between the KCBS and CHSH inequalities, we prepared the states $|\psi_\phi\rangle$ (Eqn. 5.5) and calculated the average values of $\langle \mathrm{KCBS} \rangle$ and $\langle \mathrm{CHSH} \rangle$ for different values of ϕ. We prepared the $|\psi_\phi\rangle$ states of a ququart-qubit system where the ququart is encoded by the ^{1}H, ^{19}F NMR qubits and the qubit is encoded by the ^{13}C NMR qubit. For the implementation of the monogamy inequality, we decomposed the projectors in terms of the Pauli operators $\{I, \sigma_x, \sigma_y, \sigma_z\}$.

To experimentally test the inequalities on an NMR quantum processor, we experimentally measured the expectation values for a prepared state. This can be achieved by decomposing the observables as linear combinations of Pauli operators, which can be mapped onto a single-qubit Pauli z operator. This mapping is particularly useful in the context of an NMR experimental setup, where the observed z magnetization of nuclear spins is proportional to the expectation value of the z operator of the spin in that state.

5.3.3 Experimental study of quantum versus classical boundary

In an NMR quantum information processor it is only possible to measure the expectation value of the observables, so we first translate monogamy inequality (Eq.3), which involves the KCBS and CHSH inequality, in terms of expectation values. We have rewritten the KCBS and CHSH inequality in terms of expectation values so that we can measure the inequalities in the NMR experiment. Since the observables involved in the KCBS inequality (Eqn. 5.1) follow the exclusive scenario given in Fig. 5.2, the KCBS inequality can be rewritten as:

$$\begin{aligned}
\mathcal{K}_\mathcal{C} &= 5 - 4P(C_1 = 1) - 4P(C_2 = 1) - 4P(C_3 = 1) - 4P(C_4 = 1) - 4P(C_5 = 1) \\
&= 5 - 4\sum_{i=1}^{5} \langle \Pi_i^k \rangle \\
&= 5 - 4\sum_{i=1}^{5} Tr[\Pi_i^k \rho_\phi] = Tr[F\rho_\phi] \qquad (5.7)
\end{aligned}$$

where Π_i^k are the projectors involved in the inequality and F is defined as the linear combination of Pauli matrices as:

$$F = 0.559B_{12} + 0.132B_{48} - 0.559B_{60} + 1.25B_{64} \qquad (5.8)$$

where B_i are the Pauli matrices. The order of B_i is in the four-base subscript and the base-four notation, 0, 1, 2, 3 can be directly mapped to either identity or the Pauli x, y, z matrices. For example B_{15} has the form $I^1\sigma_z^2\sigma_z^3$ where I, σ_z are identity and

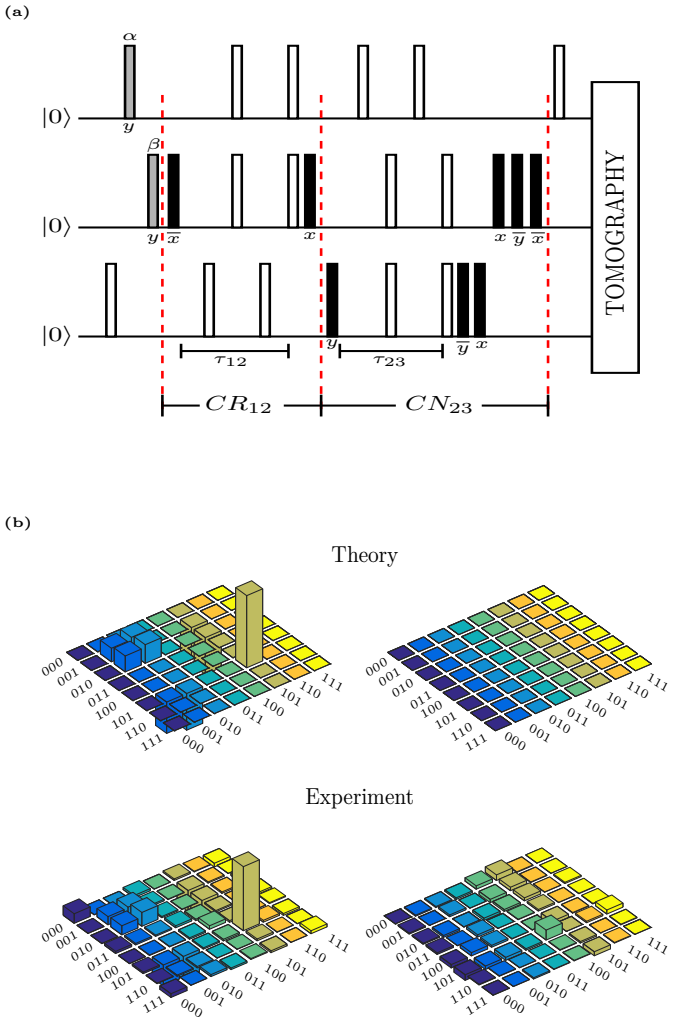

Figure 5.3: (a)Representation of NMR pulse sequence corresponding to the required state $\rho_\phi = |\psi_\phi\rangle\langle\psi_\phi|$. The flip angles α, β vary according to the various values of ϕ of the state ρ_ϕ. The empty rectangles corresponding to the π pulses of y rotation. The filled rectangles denotes the $\frac{\pi}{2}$ pulses. The time intervals τ_{12} and τ_{23} are defined as $\frac{1}{2J_{HF}}$ and $\frac{1}{2J_{FC}}$, respectively. CR_{12} and CN_{23} are control rotation and the control NOT gate, respectively. (b) The theoretically simulated and experimentally observed tomographs of the state $\rho_\phi = |\psi_\phi\rangle\langle\psi_\phi|$ for $\phi = -0.27$ radian, having an experimental state fidelity of 0.94.

Pauli z matrices, respectively. Similarly we can find the forms of others B_i (details are given in Ref. [106]. For instance, in order to determine the expectation value of $\langle B_{15}\rangle$ for the state $\rho = |\psi\rangle\langle\psi|$, we map the state ρ to $\rho_{15} = U_{15}\rho U_{15}^{\dagger}$ where $U_{15} = \mathrm{CNOT}_{12}$ followed by observing the $\langle\sigma_z^3\rangle$ in the state ρ_{15}. The expectation value $\langle\sigma_z^3\rangle$ for the state ρ_{15} is equivalent to the observing the expectation value of $\langle B_{15}\rangle$ for the state ρ.

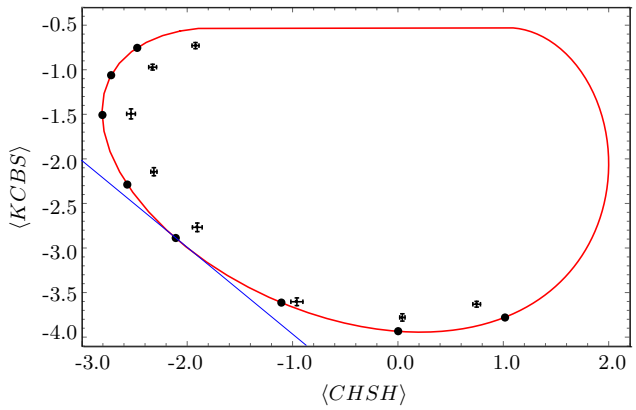

Figure 5.4: The graph representing the values of the inequalities ⟨CHSH⟩ and ⟨KCBS⟩ corresponding to the different values of ϕ. The red solid curve represents the region spanned by the allowed average values of the ⟨CHSH⟩ and ⟨KCBS⟩ inequalities. Theoretical and experimental results of ⟨CHSH⟩ and ⟨KCBS⟩ are represented by large black dots and small black dots (with error bars), respectively. The ND boundary is shown by the solid blue line.

The CHSH inequality (Eqn. 5.2) was simulated by measuring the expectation values of the projectors for the states $\rho_\phi = |\psi_\phi\rangle\langle\psi_\phi|$ with different values of ϕ. To do this we first rewrite the CHSH inequality as:

$$\beta_{CB} = Tr[\Pi_1^c\rho_\phi] + Tr[\Pi_2^c\rho_\phi] + Tr[\Pi_3^c\rho_\phi] - Tr[\Pi_4^c\rho_\phi]. \tag{5.9}$$

where $\Pi_1^c = C_1 \otimes B_1$, $\Pi_2^c = C_1 \otimes B_2$, $\Pi_3^c = C_4 \otimes B_1$, $\Pi_4^c = C_4 \otimes B_2$. Now we decompose each Π_i^c in terms of linear combinations of the Pauli matrices (B_i) and calculate the expectation values for the physically realized ququart-qubit states ρ_ϕ with different values of ϕ.

The NMR pulse sequence of state preparation is given in Fig. 5.3(a). The quantum states (for the different values of ϕ) were prepared by varying the flip angles α and β of the rf pulses. All the states required to demonstrate the simulation of monogamy inequality (Eqn. 5.3) were prepared with the state fidelities greater than or equal to 0.93. The tomograph of one such experimentally reconstructed state with $\phi = -0.27$ rad (flip angles $\alpha = 0.589$ rad and $\beta = 2.277$ rad) with state fidelity 0.94 is depicted in Fig. 5.3(b).

Table 5.1: Experimentally obtained average values of the $\langle \mathrm{CHSH} \rangle$ and $\langle \mathrm{KCBS} \rangle$ operators for eight input states.

State	ϕ(rad)	$\langle \mathrm{CHSH} \rangle$	$\langle \mathrm{KCBS} \rangle$
$\|\psi_\phi\rangle$	-0.66	0.919±0.035	-3.626±0.055
$\|\psi_\phi\rangle$	-0.48	0.167±0.038	-3.693±0.057
$\|\psi_\phi\rangle$	-0.36	-0.993±0.041	-3.490±0.062
$\|\psi_\phi\rangle$	-0.27	-1.944±0.036	-2.687±0.037
$\|\psi_\phi\rangle$	-0.22	-2.412±0.029	-2.155±0.030
$\|\psi_\phi\rangle$	-0.16	-2.654±0.041	-1.493±0.072
$\|\psi_\phi\rangle$	-0.12	-2.532±0.050	-1.036±0.069
$\|\psi_\phi\rangle$	-0.08	-2.123±0.041	-0.847±0.064

We calculated eight points on the quantum boundary corresponding to eight different input states ρ_ϕ, and computed the average values of the related KCBS and CHSH operators. The experimental results of the average values of the observables $\langle \mathrm{CHSH} \rangle$ and $\langle \mathrm{KCBS} \rangle$ are shown in Fig. 5.4 and Table 5.1. Our experimental results demonstrate that the monogamy inequality (Eqn. 5.3) is always satisfied, in agreement with the predictions of quantum theory. We also measured the average values of $\langle \mathrm{CHSH} \rangle = -1.944 \pm 0.036$ and $\langle \mathrm{KCBS} \rangle = -2.687 \pm 0.037$ for the state ρ_ϕ with $\phi = -0.27$ rad, where the quantum boundary touches the ND boundary within experimental errors. Our experimental results are in good agreement with both quantum theory and the photonics experiment [71].

5.4 Conclusions

In this chapter, we experimentally simulated the monogamy relation between contextuality and nonlocality on a ququart-qubit system. We calculated the values of the monogamy inequality between contextuality and nonlocality for eight different ququart-qubit input states, with experimental state fidelities greater than or equal to 0.93. We also measured the monogamy inequality having experimental values for $\langle \mathrm{CHSH} \rangle = -1.944 \pm 0.036$ and $\langle \mathrm{KCBS} \rangle = -2.687 \pm 0.037$ for the state ρ_ϕ (with $\phi = -0.27$) at the single point where the quantum boundary touches the ND boundary, within experimental errors. Our experimental results are hence a direct validation

of the monogamy relation between contextuality and nonlocality imposed by the no-disturbance quantum principle. An NMR quantum processor can hence be used to perform real tests of foundational issues in quantum mechanics. Our results are a step forward in the direction of understanding the deeper connections between different types of quantum correlations, namely contextual correlations and nonlocal correlations. Results of this chapter are contained in J. Magn. Reson. Open 10-11 100058 (2022).

Chapter 6

Theoretical and experimental study of monogamous relation of entropic non-contextual inequalities

6.1 Introduction

Quantum correlations have a wide range of applications in quantum information processing tasks, and most of these applications share the characteristic of monogamy of quantum correlations, which is discussed in the previous chapter. If there exists a monogamy relation between the inequalities (contextual or Bell-type) then a violation of one inequality forbids the violation of another i.e. both the inequalities can not be violated simultaneously. Braunstein and Caves provided a new perspective on quantum correlations by introducing an information-theoretic framework to explain non-local correlations [197, 198]. In this approach, the nonlocal correlations are studied in the form of inequalities, referred to as entropic inequalities. This method involves the inequalities carried with the Shannon entropies of the observables and this inequality must be satisfied in order to have the local realism of the correlations. In contrast to conventional Bell inequalities, which are linear, the presence of Shannon entropies makes such inequalities non-linear functions of probabilities. If the inequality is violated, there is no joint probability distribution over the observables, but if it is satisfied, there is no conclusive answer. Later, the study was broadened to include non-contextual situations [199, 200], referred to as entropic noncontextual (ENC) inequalities. These inequalities have undergone substantial exploration since their introduction, as well as experimental realisation [138, 201, 202, 203].

In contrast to Bell inequalities, ENC inequalities do not rely on the number of mea-

surement outcomes, making these inequalities more advantageous. In addition to numerous other applications, this characteristic of ENC inequalities makes them suitable candidates for nonlocality distillation [200] and bilocality situations. As discussed earlier, the ENC inequalities are non-linear in nature and due to this nature, it is challenging to provide the general description of monogamy relationship of these inequalities. It is possible to use the approach given in Ref. [198], to derive the monogamy of ENC inequalities, but generalisation would require sophisticated calculations. The photonic experimental setup has been used to experimentally implement the ENC inequalities, where probabilities are calculated using the frequency of clicks. Nevertheless, the monogamy of ENC inequalities has not yet been experimentally verified.

In this chapter, we have developed a theoretical method for evaluating the monogamy relationships of ENC inequalities and experimentally demonstrated the results of this approach on an NMR quantum information processor. In this method we utilize the graph theoretical approach to construct the monogamy relationship of ENC inequalities in arbitrary no-signalling scenarios. Next, we use our approach to construct the monogamy relation for the tripartite scenario in the entropic Bell-CHSH scenario. For the three parties, Alice, Bob, and Charlie, we have demonstrated that the monogamy connection holds always, i.e., if Alice and Bob violated the Bell-CHSH inequality, Alice and Charlie cannot do so (and vice-versa). Our method is also applicable to arbitrary m ENC distributed over n parties, which is an added benefit.

Further, we move on to the experimental demonstration of entropic Bell-CHSH inequality on an NMR quantum processor. In order to do this, we start by considering the case in which all three parties shared a mixed state with Alice-Bob and Alice-Charlie sharing a maximally entangled state with probability of p and $1 - p$, respectively. Further, we consider the scenario in which all three parties share an entangled tripartite pure state. We see that the monogamous relationship is always satisfied in both situations, although only one of the inequalities can show a violation. It should be highlighted that in NMR experimental set-up, it is only possible to extract expectation values. Determining the entropies in NMR hardware becomes a difficult task due to the inability to directly address the probabilities. We present a novel way to estimate entropies on an NMR quantum information processor in our experimental demonstration. Our experimental demonstration will be of independent interest to those working in this field. The scheme used to study monogamy relation of ENC inequalities in the Bell-CHSH scenario is depicted in Fig. 6.1.

For the true experimental test, the probabilities should be estimated via the frequency of clicks such as optical systems. As discussed above, on the NMR quantum information processor, we have only access to estimate the expectation value of the observable instead of probabilities. As a result, for NMR system, a true test of nonclassicality is impossible. Therefore, we assert that our experimental findings represent

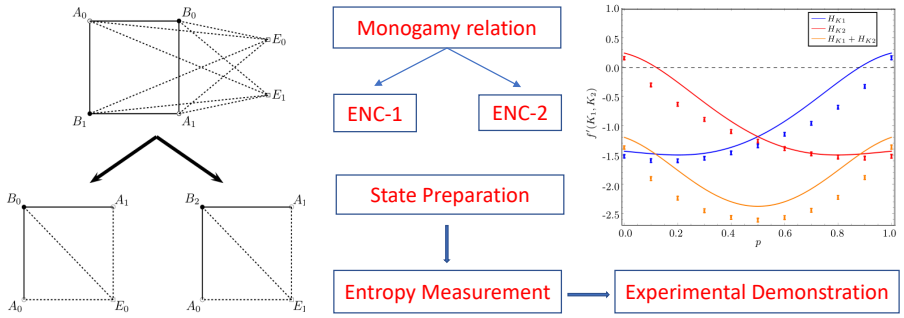

Figure 6.1: Scheme used to study monogamy relation of ENC inequalities in the Bell-CHSH scenario.

a witness rather than a true test of the monogamous relationship of ENC inequalities.

6.2 Entropic inequalities and their monogamy

In this section, we describe our theoretical results, which will be used later in the paper. We begin by providing a brief review of ENC inequalities and focus particularly on the entropic version of the Bell-CHSH inequality.

6.2.1 The entropic inequalities

An experiment corresponding to a contextuality inequality can be represented by a graph [204]. Mathematically, a graph G is defined by a set of vertices V and and a set of edges E, such that $G = (V, E)$. In relation to the contextuality inequality, the set V can represent either events, projectors or observables depending upon the scenario, while the set E represents a relationship between different elements of V, such as orthogonality, exclusivity or commutativity [204]. In this chapter, we use commutativity graphs to study ENC inequalities, in which the set of vertices corresponds to observables and two vertices are connected by an edge if they commute with each other [205].

Consider an n-cycle commutation graph in which the n vertices represent observables X_i and the existence of an edge indicates that the corresponding observables commute. An example of one such graph for $n = 4$ is given in Fig. 6.3 (top panel).

We assume that a non-contextual joint probability distribution exists over the entire set of observables considered, even though most of them do not commute. It is our aim to construct a condition based on the preceding assumption, for which a violation would indicate that such a non-contextual joint probability distribution does not exist.

6. Theoretical and experimental study of monogamous relation of entropic non-contextual inequalities

The existence of a non-contextual joint probability distribution over the observables X_i implies that it is possible to define a joint Shannon entropy $H(X_0, ..., X_{n-1})$ of them. We can then write

$$H(X_0, X_{n-1}) \leq H(X_0, ..., X_{n-1}), \tag{6.1}$$

where the relationship $H(X) \leq H(X, Y)$ is physically motivated by the fact that two random variables cannot contain less information than a single one of them. Furthermore, with repeated application of the chain rule $H(X, Y) = H(X|Y) + H(Y)$, where $H(X|Y)$ denotes the conditional entropy of observable X given information about observable Y, the right hand side of the inequality can be re-written as,

$$\begin{aligned} H(X_0, ..., X_{n-1}) &\leq H(X_0|X_1, ..., X_{n-1}) + H(X_1|X_2, ...X_{n-1}) + ... + H(X_{n-2}|X_{n-1}) \\ &\quad + H(X_{n-1}) \\ &\leq H(X_0|X_1) + H(X_1|X_2) + ... + H(X_{n-2}|X_{n-1}) + H(X_{n-1}). \end{aligned} \tag{6.2}$$

The latter inequality in Eq. (6.2) is a consequence of the relationship $H(X|Y) \leq H(X)$, which implies that conditioning cannot increase the information content of a random variable. Plugging Eq. (6.2) in Eq. (6.1) and using $H(X_0|X_{n-1}) = H(X_0, X_{n-1}) - H(X_{n-1})$, we finally get the required entropic non-contextuality inequality,

$$H_{K_1} : H(X_0|X_{n-1}) \leq H(X_0|X_1) + ...H(X_{n-2}|X_{n-1}). \tag{6.3}$$

A violation of Eq. (6.3) would then indicate that a non-contextual joint probability distribution over the corresponding set of observables does not exist.

It should be noted that no assumptions have been made regarding the nature of the observables X_i. For all intents and purposes they can correspond to projective measurements or POVMs with any number of outcomes. Furthermore, the observables could correspond to local scenarios or non-local, in which case the entropic inequality would be termed as non-contextual or Bell non-local. Since we consider generalized scenarios, we term all entropic inequalities as non-contextual as it subsumes the non-local scenarios as well.

One of the many interesting cases arises for $n = 4$ observables, which corresponds to the well known Bell-CHSH scenario. Consider two parties, Alice and Bob, each having two observables labelled $\{A_0, A_1\}$ and $\{B_0, B_1\}$ respectively, such that observables of any one party do not commute, while observables of different parties commute. Differing from the traditional Bell-CHSH scenario, it is also assumed that a measurement of the observables can have an arbitrary number of outcomes. The corresponding entropic inequality is written as,

$$H_{K_1} : H(A_1|B_1) - H(A_1|B_0) - H(B_0|A_0) - H(A_0|B_1) \leq 0. \tag{6.4}$$

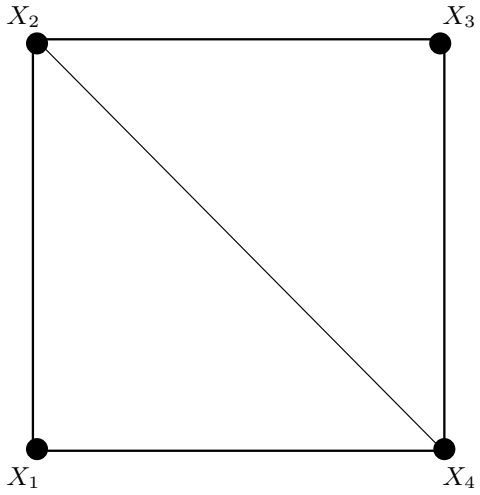

Figure 6.2: Representation of the chordal subgraph having the vertices and edges. The vertices corresponds to the observables X_i and the edges corresponds to commutativity relationship between them.

A violation of the above inequality implies a non-existence of a joint probability distribution over all the observables A_x and B_y $\forall x, y \in \{0, 1\}$. In the next section, we show that ENC inequalities admit a monogamous relationship which can be derived using a graph theoretic formalism. We particularly focus on the entropic Bell-CHSH scenario described above and show that it admits a monogamous relationship.

6.2.2 Monogamy of entropic inequalities

We now elucidate the formalism to check and derive a monogamous relationship for any arbitrary scenario using the graph theoretic formalism. It should be remembered that a violation of the inequality (6.4) implies that a joint probability distribution cannot exist over the given observables.

Proposition 6.2.1. *A monogamous relationship for a set of n observables X_i, corresponding to m non-contextuality scenarios exists if their joint commutation graph can be vertex decomposed into m chordal subgraphs such that all edges appearing in the original m non-contextuality graphs must appear just once in the decomposition. The monogamous relationship then reads as,*

$$H_{K_1} + H_{K_2} + H_{K_3} + ... + H_{K_m} \leq 0, \tag{6.5}$$

where H_{K_i} denotes the ith ENC inequality.

Proof. A chordal graph is a graph in which all cycles of four or more vertices have a chord. A chord is an edge that is not part of the cycle but which connects two of the vertices. It should be noted that the definition of chordal subgraphs implies that these subgraphs must have an edge connecting two vertices, such that any induced cycles in the subgraph have a length equal to three. Any induced cycles of length greater than 3 should then have an edge such that the resultant induced cycle satisfies the definition.

For these 3-cycle induced subgraphs, it is possible to write down the corresponding entropic inequality. Since it is a 3-cycle graph, a joint probability distribution over the observables always exists [66] and the entropic inequality is never violated. Therefore, we can add all the entropic inequalities obtained in this fashion to obtain

$$\sum_{l} \sum_{i,j=1}^{n} g_l(H'(X_i|X_j)), \tag{6.6}$$

where $H'(X_i|X_j) = H(X_i|X_j)$ only if the vertices i and j belong to an edge and zero otherwise, $g(X) = \pm X$ depending on the 3 cycle chosen and l is the number of edges appearing in the m chordal graphs. It should be noted that Eq. (6.6) is a linear combination of $H(X_i|X_j)$ and since we require that all the terms appearing in the individual m ENC inequalities appear in the decomposition, it is possible to obtain the form in Eq. (6.5) via linear manipulation of the ENC inequalities of the 3-cycle induced graphs. It should be noted that each term appearing in Eq. (6.3) corresponds to an edge in the commutativity graph and missing even a single edge in the chordal decomposition, would make one of the non-contextuality inequalities incomplete and Eq. (6.5) unachievable. Furthermore, the linear manipulations required correspond to choosing a suitable form of $g(X)$ such that the m ENC inequalities can be obtained by grouping certain terms together. This manipulation depends on the commutation graph of the interested scenario.

As an example of our technique consider the chordal graph given in Fig. 6.2 which is formed by two 3-cycle graphs. We assume that this is one of the subgraphs obtained via vertex decomposition of a joint commutativity graph such that the term $H(X_2|X_4)$ corresponding to the edge (X_2, X_4) does not appear in Eq. (6.5), while the terms corresponding to the other edges do appear. In order to eliminate this term, we consider the ENC inequality for the 3-cycle graph with vertices (X_1, X_2, X_4), written in a cyclic form as,

$$H(X_1|X_4) - H(X_1|X_2) - H(X_2|X_4) \leq 0, \tag{6.7}$$

while for the other 3-cycle graph formed by the vertices (X_2, X_3, X_4) we use an anti-cyclic form of the ENC inequality as,

$$H(X_2|X_4) - H(X_2|X_3) - H(X_3|X_4) \leq 0. \tag{6.8}$$

Since all 3-cycle graphs admit a joint probability distribution, the aforementioned inequalities are always satisfied and can therefore be added to give,

$$H(X_1|X_4) - H(X_1|X_2) - H(X_2|X_3) - H(X_3|X_4) \leq 0, \tag{6.9}$$

which is the ENC inequality over the graph in Fig 6.2 without the edge (X_2, X_4). We use this technique to derive our monogamous relationships. In the case when such a vertex decomposition cannot be found, we cannot guarantee that a monogamous relation will exist.

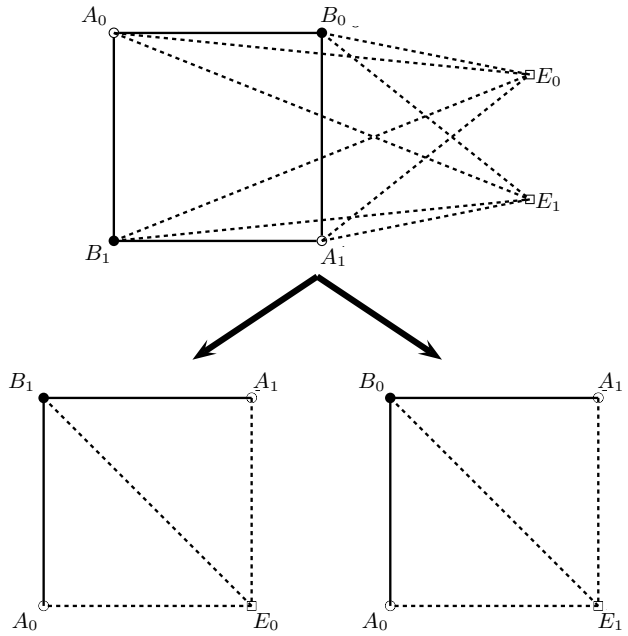

Figure 6.3: Representation of the joint Alice-Bob-Eve commutation graph (top) and its chordal decomposition (bottom) corresponding to Proposition 6.2.1. Solid and dashed lines represent the commutativity relationship between observables of Alice Bob, and Alice Charlie, respectively.

We now apply this technique to derive a monogamous relationship of two entropic CHSH inequalities. Consider a standard monogamous relationship between two en-

tropic non-contextuality scenarios, K_1 and K_2 which should dictate,

$$H_{K_1} + H_{K_2} \leq 0, \tag{6.10}$$

As explained, in order to achieve a form of Eq. (6.10), the joint graph of the non-contextuality scenarios must be decomposable into chordal subgraphs, which admit a joint probability distribution. However, we also require an additional feature that all edges of the individual non-contextuality graphs must appear at least once in any of the chordal subgraphs.

Consider the CHSH scenario in which two parties Alice and Bob can perform a measurement of the observables A_0, A_1 and B_0, B_1 respectively. We assume a third party Charlie with observables E_0 and E_1, which commute with the observables of Alice and Bob. The scenario is illustrated by a joint graph as shown in Fig. 6.3, where vertices represent observables and edges indicate the commutation relationship. Without loss of generality we assume that Charlie would like to violate the entropic CHSH inequality with Alice. The two corresponding Alice-Bob and Alice-Charlie entropic CHSH inequalities are,

$$\begin{aligned} H_{K_1} :& H(A_0|B_0) - H(A_0|B_1) \\ & - H(B_1|A_1) - H(A_1|B_0) \leq 0, \end{aligned} \tag{6.11}$$

$$\begin{aligned} H_{K_2} :& H(A_0|E_0) - H(A_0|E_1) \\ & - H(E_1|A_1) - H(A_1|E_0) \leq 0. \end{aligned} \tag{6.12}$$

The joint commutation graph is decomposed into two chordal graphs while keeping the edges appearing in the individual Alice-Bob and Alice-Charlie CHSH scenarios intact in the decomposition, as shown in Fig. (6.3). The corresponding ENC inequalities for each 3-cycle graph in every chordal subgraph are given as,

$$H(A_0|E_0) - H(A_0|B_1) - H(B_1|E_0) \leq 0, \tag{6.13}$$

$$H(B_1|E_0) - H(B_1|A_1) - H(A_1|E_0) \leq 0, \tag{6.14}$$

$$H(A_0|B_0) - H(A_0|E_1) - H(E_1|B_0) \leq 0, \tag{6.15}$$

$$H(E_1|B_0) - H(E_1|A_1) - H(A_1|B_0) \leq 0, \tag{6.16}$$

Being cyclic and chordal, all the above inequalities are a necessary and sufficient condition for a joint probability distribution to exist. Furthermore, we have carefully

chosen the terms with positive and negative coefficients so as to achieve a final form according to Eq. (6.10). Adding the above inequalities and grouping the terms according to H_{K_1} and H_{K_2}, we obtain

$$H_{K_1} + H_{K_2} \leq 0, \tag{6.17}$$

which is the required monogamy relationship. We note that this monogamy relationship was also derived in [198], albeit in a different manner and specifically for the entropic CHSH inequality. However, our formalism can be readily generalized to n observables distributed among m parties. □

The derived monogamy relationship (6.17) imposes severe restrictions on the violation of Alice-Charlie entropic CHSH inequality.

6.3 Experimental demonstration

In this section, we experimentally demonstrate the monogamy relationship derived for the entropic Bell-CHSH scenario (6.17) on an NMR quantum information processor, using two different set of states. We show that for both the sets of states, the entropic Bell-CHSH obeys the monogamy relationship we derived above.

6.3.1 Implementation using a mixed tripartite state

We experimentally implement the monogamy inequality (6.17) using a mixed tripartite state which is a classical mixture of two pure maximally entangled states given as:

$$\rho = p(|\psi_1\rangle\langle\psi_1|) + (1-p)(|\psi_2\rangle\langle\psi_2|), \tag{6.18}$$

where

$$\begin{aligned} |\psi_1\rangle &= \frac{1}{\sqrt{2}}(|001\rangle + |111\rangle), \\ |\psi_2\rangle &= \frac{1}{\sqrt{2}}(|010\rangle + |111\rangle), \end{aligned} \tag{6.19}$$

and $p \in [0, 1]$. As can be seen, the state ρ physically implies that Alice and Bob share a maximally entangled state with probability p while Charlie is separable, and with probability $1 - p$, Alice and Charlie share a maximally entangled state while Bob is separable.

The observables of Alice, Bob and Charlie are assumed to lie in the $X - Z$ plane and correspond to Pauli spin measurements along the unit vectors $\boldsymbol{a}, \boldsymbol{a'}, \boldsymbol{b}, \boldsymbol{b'}$ and $\boldsymbol{e}, \boldsymbol{e'}$

respectively. The vectors $\boldsymbol{a}, \boldsymbol{b'}, \boldsymbol{a'}$ and $\boldsymbol{b}$ are successively separated by an angle $\frac{\theta}{3}$, while the vectors $\boldsymbol{e}$ and $\boldsymbol{e'}$ are taken to be the same as Bob's. The corresponding Pauli observables are then given as:

$$\begin{aligned} A_0 &= \begin{bmatrix} 1 & 0 \\ 0 & -1 \end{bmatrix}, & A_1 &= \begin{bmatrix} \cos\frac{2\theta}{3} & -\sin\frac{2\theta}{3} \\ \sin\frac{2\theta}{3} & \cos\frac{2\theta}{3} \end{bmatrix} \\ B_0 &= \begin{bmatrix} \cos\theta & -\sin\theta \\ \sin\theta & \cos\theta \end{bmatrix}, & B_1 &= \begin{bmatrix} \cos\frac{\theta}{3} & -\sin\frac{\theta}{3} \\ \sin\frac{\theta}{3} & \cos\frac{\theta}{3} \end{bmatrix}, \end{aligned} \tag{6.20}$$

while the observables of Charlie (E_0, E_1) are the same as Bob's but acting in a different Hilbert space. All of the aforementioned observables have eigenvalues $a_i, b_i, e_i \in \{-1, +1\}$ and follow the commutativity conditions as shown in Fig. 6.3.

For the set of observables given in Eq. (6.20), the maximum violation of the Alice-Bob entropic CHSH inequality $H_{K1} = 0.237$ bits is found to be at $\theta = 0.457$ radians when the parties share the state $|\psi_1\rangle$. The same also holds for Alice-Charlie entropic CHSH inequality when the parties share the state $|\psi_2\rangle$.

We experimentally implemented the monogamy relation given in Eq. (6.17) on an eight-dimensional quantum system. We used a molecule of ^{13}C -labeled diethyl fluoromalonate dissolved in acetone-D6 (for more details see Chapter 2). Experiments were performed on a Bruker Avance III 600-MHz FT-NMR spectrometer equipped with a QXI probe. Local unitary operations were achieved by RF pulses of suitable amplitude, phase, and duration and nonlocal unitary operations were achieved by free evolution under the system Hamiltonian.

The system is initialized in the PPS state i.e. $|000\rangle$ using the spatial averaging technique [111], which is based on dividing the system in sub-ensembles which can be accessed independently in NMR by using a combination of RF pulses and pulsed magnetic gradients. The state tomography was performed using the least square optimization technique [206] with an experimental state fidelity of 0.98.

We began by preparing the mixed tripartite state given in Eq. (6.18) for different values of p. In order to achieve this, we utilized the temporal averaging technique [9, 207]. Using this technique, it is possible to prepare arbitrary mixed states on an NMR quantum information processor, by applying suitable unitary transformations on some common initial PPS. The different experiments are performed on common initial states, the results of which are independently stored. Finally, these results are combined to produce an average state which simulates the behavior of a mixed state.

In our case, we prepared the mixed state given in Eq. (6.18), which is a mixture of two pure states $|\psi_1\rangle$, $|\psi_2\rangle$. We first prepared these two states by applying suitable unitaries on the initial state $|000\rangle\langle 000|$ in two different and independent experiments [208]. The states of these two experiments are then added with appropriate probabilities to achieve the desired mixed state given in Eq. (6.18). To demonstrate

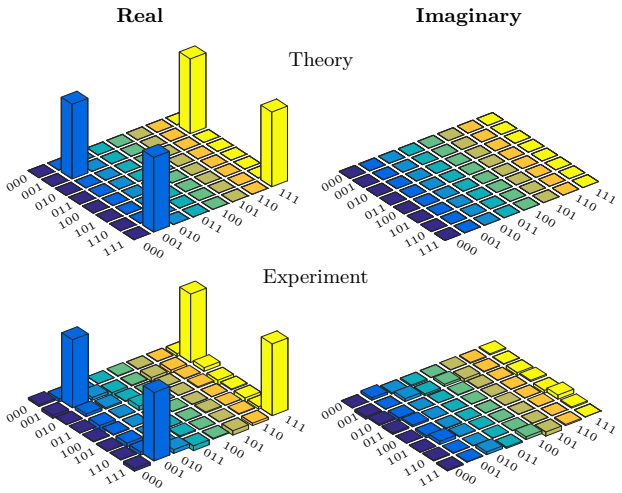

Figure 6.4: The theoretical and experimental tomographs of the tripartite state ρ, with an experimental state fidelity of 0.97 corresponding to $p = 1$.

the monogamy relation, we chose different values of p to experimentally prepare the desired mixed state with experimental state fidelities ≥ 0.956. The tomograph of one such experimentally prepared state with $p = 1$ is shown in Fig. 6.4.

After experimentally preparing the states, we measured the desired probabilities in order to calculate the entropies involved in the inequality given in Eq. (6.17). In order to calculate the probabilities, we transformed the required probabilities in terms of expectation values. This is necessary because experiments on an NMR quantum information processor yield only expectation values of the observables. These expectation values are evaluated by decomposing the observables in terms of linear combinations of Pauli operators which can be mapped to the single-qubit Pauli Z operator. This mapping is particularly useful in the context of an NMR experimental setup where the expectation value of the Z operator is easily accessible and corresponds to the observed z magnetization of a nuclear spin in a particular quantum state. The normalized experimental intensities of the NMR signal then provide an estimate of the expectation value of the Pauli Z operator in that quantum state [209].

The probabilities can be written as $P(A_i = a_i, B_j = b_j) = \text{tr}(\rho |a_i\rangle\langle a_i| \otimes |b_j\rangle\langle b_j| \otimes I)$ and $P(A_i = a_i, E_j = e_j) = \text{tr}(\rho |a_i\rangle\langle a_i| \otimes I \otimes |e_j\rangle\langle e_j|)$ where $|a_i\rangle$, $|b_j\rangle$, $|e_j\rangle$ are the eigenvector of the observables corresponding to Alice, Bob and Charlie, respectively. The observables $(|a_i\rangle\langle a_i| \otimes |b_j\rangle\langle b_j| \otimes I)$, $(|a_i\rangle\langle a_i| \otimes I \otimes |e_i\rangle\langle e_i|)$ are decomposed in terms of linear combinations of Pauli operators and details are given in Appendix-A. The idea is to unitarily map the state ρ to another state ρ', such that $\langle X\rangle_\rho = \langle I_{iz}\rangle_{\rho'}$ where X is the observable to be measured in the state ρ and I_{iz} is the z-spin angular momentum of the qubit. This can be achieved by measuring the I_{iz} on the state ρ'. For

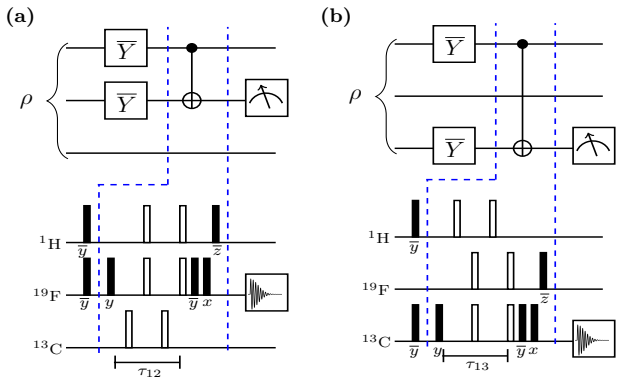

Figure 6.5: Representation of quantum circuit and associated NMR pulse sequence that are used to map the state ρ to the state ρ' such that (a) $\langle \sigma_x \otimes \sigma_x \otimes I \rangle_\rho = \langle I_{2z} \rangle_{\rho'}$, (b) $\langle \sigma_x \otimes I \otimes \sigma_x \rangle_\rho = \langle I_{3z} \rangle_{\rho'}$. The black and white rectangles represent the $\frac{\pi}{2}$ and π RF pulses. The τ_{12}, τ_{13} represent the free evolutions.

example, one can find the expectation values of $\langle \sigma_x \otimes \sigma_x \otimes I \rangle_\rho$ and $\langle \sigma_x \otimes I \otimes \sigma_x \rangle_\rho$ which are involved in the evaluation of probabilities, by using the quantum circuit and corresponding NMR pulse sequence given in Fig.6.5(a) and Fig.6.5(b) respectively, where the implementation is followed by a measurement of the spin magnetization of the second and third qubits, respectively.

We experimentally calculated the ENC inequalities H_{K1}, H_{K2} and the ENC monogamy relation $H_{K1}+H_{K2}$ for the tripartite mixed state given in Eq. (6.18) for different values of p. Experimental values of H_{K1}, H_{K2}, $H_{K1} + H_{K2}$ with respect to various values of p are plotted in Fig. 6.6. It can be seen that H_{K1} is violated for the tripartite state with $p = 1$, while H_{K2} is violated for the state with $p = 0$. The monogamy relation $H_{K1} + H_{K2}$ is never violated for any value of p and the results are in good agreement with the theoretical predictions.

It is seen that the experimental values are always lower than the corresponding theoretical values. This is due to the fact that the maximum value of the inequality is always achieved for a pure state and any addition of noise makes it a mixed state. Therefore, the value is always observed to be lower than the theoretical one. The difference between them also increases with increasing values of p upto $p = 0.5$. For this region, the state prepared for $p = 0.0$ is the dominant one which is shown to violate H_{K_1}. Furthermore, the corresponding inequalities are logarithmic in nature, which also compounds the errors for states till $p = 0.5$. However, after this value the state prepared for $p = 1.0$ dominates and the errors again follow a similar trend. It should be noted that the experimental curve follows the same trend as the theoretical curve.

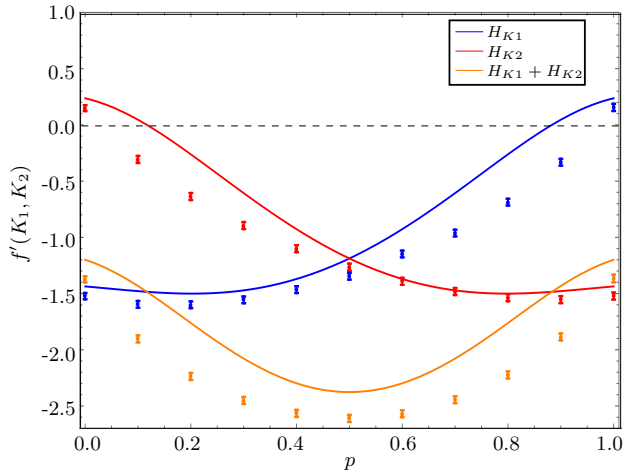

Figure 6.6: Plot showing the experimentally determined values ($f'(K_1, K_2)$) of the monogamy inequality monogamy inequality Eq. (6.17) for the tripartite mixed states corresponding to various p values. The black dotted line represents the highest non-contextual value that inequalities H_{K1}, H_{K2} and $H_{K1}+H_{K2}$ can achieve. Red points with error bars and a red line show the experimental and theoretical computed values for the inequality H_{K1}. The inequalities H_{K2} and $H_{K1}+H_{K2}$ are represented in a similar way.

6.3.2 Implementation using a pure tripartite state

In this subsection, we experimentally test the monogamy relation Eq. (6.17) for a pure tripartite state, having two parameters which we can vary. We show that the monogamy relation holds and is in good agreement with theoretical predictions.

We take a pure tripartite state of the form,

$$|\phi\rangle = N(p_1|001\rangle + p_2|010\rangle + (p_1+p_2)|111\rangle), \tag{6.21}$$

where $N = \frac{1}{\sqrt{p_1^2+p_2^2+(p_1+p_2)^2}}$ is the normalization factor. We experimentally prepared five different states corresponding to various values of p_1 and p_2. The quantum circuit and the corresponding NMR pulse sequence is given in Fig. 6.7(a), (b). Different pure states corresponding to various values of p_1 and p_2 were generated by suitably choosing the values of θ_1, θ_2 and θ_3. Tomograph of one such experimentally prepared state with $p_1 = 0.25$ and $p_2 = 0.50$ is depicted in Fig. 6.8, with an experimental state fidelity of 0.93. After preparing the states, we measured the desired probabilities by mapping the state onto the Pauli basis operators in order to calculate the entropies involved in the inequality Eq. (6.17) as discussed earlier in Sec. 6.3.1.

We experimentally evaluate H_{K_1}, H_{K_2} and $H_{K_1}+H_{K_2}$ with respect to the different values of p_1 and p_2 and the results are given in Table-6.1. We see that the inequality

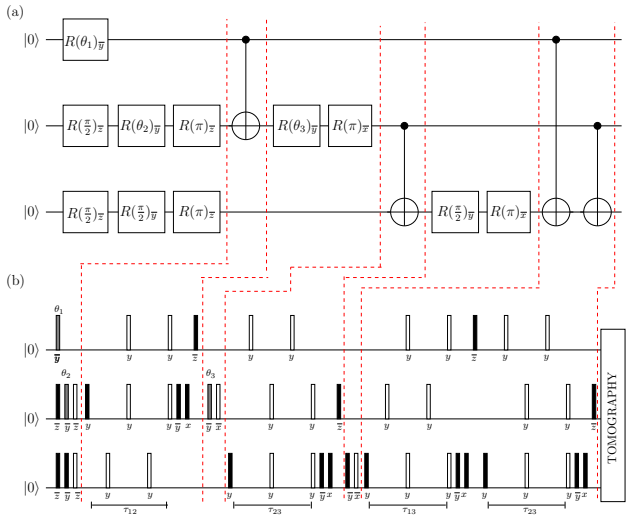

Figure 6.7: (a) Representation of quantum circuit and corresponding (b) NMR pulse sequence of state preparation for the tripartite pure state $|\phi\rangle$. The black and white rectangles denote $\frac{\pi}{2}$ and π RF pulses. The free evolutions are denoted by $\tau_{12}, \tau_{23}, \tau_{13}$.

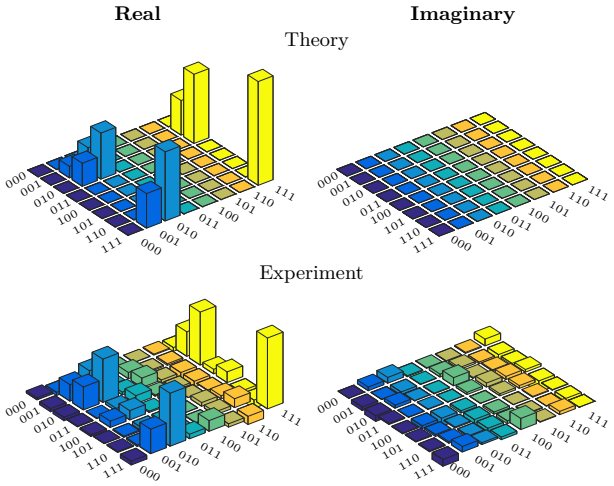

Figure 6.8: Tomograph of theoretically computed and experimentally reconstructed of the tripartite pure state $\rho' = |\phi\rangle\langle\phi|$ with $p_1 = 0.25, p_2 = 0.50$.

Table 6.1: Theoretically computed and experimentally measured values of the monogamy inequalities for a pure state.

		H_{K_1}		H_{K_2}		$H_{K_1} + H_{K_2}$	
p_1	p_2	Theory	Experiment	Theory	Experiment	Theory	Experiment
1.00	0.00	0.236	0.156±0.032	-1.436	-1.522±0.035	-1.200	-1.366±0.034
0.50	0.25	-0.492	-0.606±0.021	-1.338	-1.413±0.027	-1.830	-2.019±0.024
0.50	0.50	-1.017	-1.103±0.022	-1.017	-1.082±0.030	-2.034	-2.185±0.026
0.25	0.50	-1.338	-1.397±0.021	-0.492	-0.598±0.024	-1.830	-1.995±0.023
0.00	1.00	-1.436	-1.523±0.028	0.236	0.149±0.025	-1.200	-1.374±0.027

H_{K_1} is violated for $p_1 = 1$ and $p_2 = 0$ and H_{K_2} is violated for $p_1 = 0$ and $p_2 = 1$, while the monogamy relationship $H_{K_1} + H_{K_2}$ is never violated for any value of p_1 and p_2. This shows that the monogamy relation between the ENC inequalities is obeyed for all such possible states.

6.4 Concluding Remarks

In this chapter, we develop a theoretical framework to analyze when a scenario will exhibit a monogamous relationship. We perform our analysis of the monogamy relations expected in a general tripartite scenario for the entropic Bell-CHSH inequality and give the first theoretical study of the monogamy of entropic inequalities based on the graph theoretic formalism. We also give the first experimental demonstration of monogamy of entropic correlations using three NMR qubits. Evaluating entropy on an NMR quantum processor is quite hard and has not been performed earlier. We are able to obtain information about entropies using measurements of only the expectation values of observables. We experimentally show the monogamy of entropic inequality for a pure tripartite state as well as for the mixed state. This indicates with certainty that our formalism holds in general.

It should be noted that due to limitations of access to individual events, the NMR implementation of such scenarios involves use of Born rule to interpret the results of measurements. This is not the ideal way of carrying out such experiments and a more

refined test would evaluate the requisite probabilities without assuming the Born rule. This is possible on optical systems [202, 203], where the probabilities are calculated by estimating the frequency clicks of the photodetectors rather than the Born rule.

The experimental implementation of monogamy inequalities is important for quantum information processing tasks and our results are a step forward in this direction. The results described in this chapter are available in arXiv:2201.02330.

Chapter 7

NMR implementation of variational quantum algorithms to calculate the ground and excited state energies of H_2 molecule

7.1 Introduction

In the 21^{st} century, the second quantum revolution is taking place and it has been led by quantum computing [210]. It has been discovered in recent years that there are a large number of problems that a quantum algorithm would be able to resolve much more efficiently than its corresponding classical algorithm [1]. One such class of problems is the quantum simulation, introduced by Feynman [211]. The goal of quantum simulation is to efficiently simulate a quantum system and obtain information about the system.

Finding the eigenstates of a given system's Hamiltonian is one of the key problems coming under the hood of quantum simulation[212]. Such problems involve the calculation of energies of molecules and have been a prime focus in the field of quantum chemistry [213]. Finding the ground and excited state energies of a molecule gives enormous information about its properties like stability, rate of reactions, and orbitals involved [214]. Calculation of energies of molecules becomes a challenging task for a classical computer as the complexity of the molecules grows. The first thing to realize when working with these problems is that there is no analytical way to solve them; the only solution is a numerical one. However, because of the enormous number of degrees

of freedom involved, even this becomes a difficult task for molecules with a significant number of atoms and electrons. This is where a quantum algorithm proves superior to its classical counterpart. On a quantum computer, a variety of quantum algorithms are being created to effectively calculate the energy of the molecules [215, 216, 217].

Quantum algorithms may, however, become exceedingly error-prone and require quantum error correction in the near future because we are still very far from creating an error-free quantum computer. Given that we are in the NISQ age [218], a novel class of algorithms that are partially classical and partially quantum has been devised. These algorithms can minimize the necessary gate depth and help to mitigate errors to a certain extent. One such algorithm, the Variational Quantum Eigensolver (VQE), has been developed to compute the Hamiltonians' ground state on a quantum computer [219, 220, 221, 222]. Due to the low circuit depth of the VQE algorithm, the quantum-enhanced computation may be possible in the near future [223].

The excited state energies of the molecules have various crucial applications in addition to the ground state energy. There have been some attempts to create an algorithm for a molecular Hamiltonian's excited states determination. There have been two proposals proposed for the same: a method that minimizes the Von Neumann entropy [224] and the quantum subspace expansion method [225]. Variational quantum deflation (VQD), an algorithm that is an extension of the VQE algorithm, has recently been developed to determine the excited state energies of molecules. [226]. VQD typically detects excited states for almost no additional cost compared to Ref. [224, 225]. In this algorithm, the excited states are obtained by applying the VQE algorithm to a modified Hamiltonian which has the excited states as its ground state. Using VQE techniques, several experiments have been carried out to show the energy spectrum of molecules [223, 225, 227, 228].

In this chapter, we have used the VQE and VQD algorithms to simulate the ground state energy and excited state energies of H_2 molecule, respectively. On an NMR quantum computer, the simulation results are validated. In order to identify the state that minimised the energy expectation value, we changed the states in the qubit space in accordance with the variational principle. This is accomplished by using the Unitary Coupled Cluster Singles and Doubles approach (UCCSD) [229]. For the experimental verification, the expectation values, involved in the H_2 molecule Hamiltonian, is determined experimentally using two NMR qubits. The expectation values for the required state are experimentally calculated by measuring the single-qubit Pauli Z operator of experimentally prepared states. We also simulated of the energies of the H_2 molecule for the reduced Hamiltonian, on a single-qubit system and verified the results on an NMR quantum computer. This is the first experimental example of the H_2 molecule's energy calculation using just one qubit (less resource compared to other works). Finally, we demonstrate how a similar approach can be used to cut down on the resources

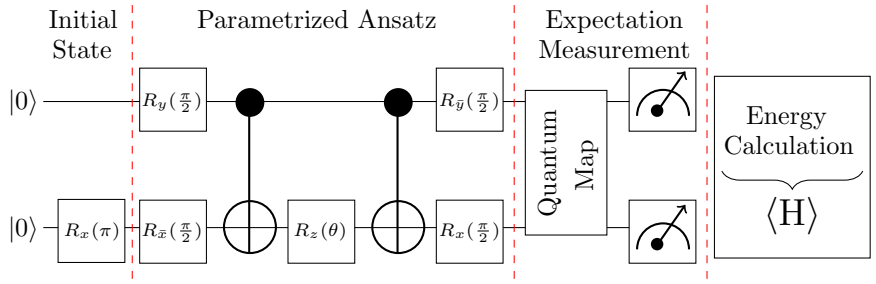

Figure 7.1: Scheme used to simulate the ground state energy of H_2 molecule.

needed to calculate the LiH molecule's ground state energy. The scheme used to simulate the ground state energy of H_2 molecule is depicted in Fig. 7.1.

7.2 Energy calculation of H_2 molecule using quantum hybrid algorithms

7.2.1 Variational quantum eigensolver

Finding the eigenstates and eigenvalues is unarguably a crucial step in analyzing a Hamiltonian system. Given that the quantum systems are described by Hamiltonians, the matter of finding their spectra becomes increasingly difficult as their size grows. This means that a fully classical method will not be a viable option for large systems and hence its a task that falls into the bucket of quantum computer. Variational quantum eigensolver (VQE) is one of the hybrid methods that can be used to solve a given quantum many-body Hamiltonian to obtain its ground state and its energy.

The basic principle of VQE is the same as the variational principle used in quantum mechanics to find the ground state of a Hamiltonian. The procedure is as follows.

1. Given a Hamiltonian H, choose an ansatz, a state with at least one free parameter, say $|\psi(\theta)\rangle$.

2. Take an initial value for the parameter and obtain the expectation value of the Hamiltonian, $\epsilon_\theta = \langle\psi(\theta)|H|\psi(\theta)\rangle$

3. Now, varying θ try to iteratively minimize the energy expectation value.

Notice, if $|E_i\rangle$ are the energy eigenkets of the Hamiltonian (such that $E_0 < E_1 <$

E_2...,) then we can write

$$|\psi(\theta)\rangle = \sum_i \alpha_i(\theta)\,|E_i\rangle \tag{7.1}$$

$$\epsilon_\theta = \sum_i |\alpha_i(\theta)|^2 E_i \tag{7.2}$$

Therefore, the least expectation value that can be obtained is the ground state energy of the Hamiltonian itself. In that case, the state $|\psi(\theta)\rangle$ will be the ground state of the given Hamiltonian. But this depends on the choice of the initial ansatz state as it might not explore enough space to pass through the ground state. However, a clever choice of the ansatz can give a very good approximation to the ground state of the Hamiltonian.

The main crux of using a quantum computer is in using an actual quantum system to store the quantum state instead of using a classical computer. This is of course resource efficient than doing a fully classical calculation. The VQE algorithm is however hybrid because we will use a classical computer to update the value of the parameter θ so as to arrive at the right parameter value that minimizes the energy expectation.

7.2.2 Variational quantum deflation

As was introduced in [226], the excited states of a Hamiltonian can be obtained from the variational principle using a method called Variational Quantum Deflation (VQD). The procedure is that, after getting the ground state from VQE, the Hamiltonian is modified such that the global minimum expectation value of the Hamiltonian only lies in the space orthogonal to the ground state and it is minimized specifically by the excited state of the Hamiltonian. So, if VQE is now applied to minimize the expectation of this new Hamiltonian, the excited state and its energy can be obtained.

If $|\phi_0\rangle$ is the ground state of the original Hamiltonian H, the VQD Hamiltonian for the first excited state is given by,

$$H_1 = H + \beta_0 |\phi_0\rangle\langle\phi_0| \tag{7.3}$$

where β_0 is a parameter that is useful to obtain the excited state in a self correcting manner. It means, if we have an arbitrary state $|\psi(\theta)\rangle$, which can be expanded as,

$$|\psi(\theta)\rangle = \sum_i \alpha_i\,|\phi_i\rangle \tag{7.4}$$

$$\langle\psi(\theta)|H_1|\psi(\theta) = |\alpha_0|^2(\beta_0 + E_0) + \sum_{i=1} |\alpha_i|^2 E_i \tag{7.5}$$

So notice, if we choose β_0 such that $\beta_0 + E_0 > E_1$, then the minimum value of the expectation will be equal to E_1, the first excited state energy. Or in other words, if we redefine β_0 to be $\gamma - E_0$, then

$$\langle\psi(\theta)|H_1|\psi(\theta) = |\alpha_0|^2\gamma + \sum_{i=1} |\alpha_i|^2 E_i \tag{7.6}$$

So, the condition for getting the excited state energy will be that $\gamma > E_1$. This acts as a self-correcting method in the sense that, if VQE is performed on H_1 with $\gamma < E_1$, then VQE gives minimum energy as γ. Thus if we keep on repeating VQE with an increasing value of γ in each step, the point where VQE gives the minimum energy to be less than γ can be taken to be the first excited state energy, E_1.

This can be generalized to get the n^{th} excited state by taking the VQD Hamiltonian as,

$$H_n = H + \sum_{i=0}^{n-1} (\gamma - E_i)|\phi_i\rangle\langle\psi_i| \tag{7.7}$$

where $|\phi_i\rangle$ for $i = 1$ to n are the first n energy eigenstates of H. The condition to obtain the n^{th} excited state in this case is that, $\gamma > E_n$ for which the minimum expectation value of H_n will be equal to E_n.

In this work, we will apply the VQD to obtain the energy spectrum of the H2 molecule using an NMR quantum computer.

7.2.3 H_2 molecule structure

Since many of the chemical properties of a molecule are determined by its ground state and the immediate excited states, it becomes extremely important to accurately measure the energies of these states. The Hamiltonian of the H_2 molecule in the first quantized form (in atomic units) is given by [225, 228],

$$\begin{aligned} H = &- \sum_i \frac{\nabla_{R_i}}{2M_i} - \sum_i \frac{\nabla_{r_i}}{2} + \sum_{i,j>i} \frac{Z_i Z_j}{|R_i - R_j|} \\ &- \sum_{i,j>i} \frac{Z_i}{|R_i - r_j|} + \sum_{i,j>i} \frac{1}{|r_i - r_j|} \end{aligned} \tag{7.8}$$

where R_i, M_i, Z_i stands for the position, mass and charge of the i^{th} nuclei respectively and r_i stands for the position of the i^{th} electron. In the above Hamiltonian, the first two terms correspond to the kinetic energy of the nuclei and the electrons, the third

term corresponds to the inter-nuclear Coulombic repulsion, 4th term to the nucleus-electron Coulombic attraction, and the last term to the inter-electronic Coulombic repulsion. This Hamiltonian is generally solved first by using the Born-Oppenheimer approximation where the nuclei are assumed to be at rest and only electrons are mobile. Then, the Hamiltonian is cast into the second quantized form using a specific choice of N particle basis functions ϕ_i. The second quantized form of this Hamiltonian will be given by [225, 228],

$$H = \sum_{\mu,\nu} t_{\mu,\nu} c_\mu^\dagger c_\nu + \sum_{\mu,\nu,\mu'\nu'} V_{\mu,\nu,\mu'\nu'} c_\mu^\dagger c_\nu^\dagger c_{\nu'} c_{\mu'}$$

where,

$$t_{\mu,\nu} = \int d\sigma \phi_\mu^*(\sigma) \left(-\frac{\nabla_r}{2} - \sum_i \frac{Z_i}{|R_i - r|} \right) \phi_\mu(\sigma)$$

$$V_{\mu,\nu,\mu'\nu'} = \int d\sigma_1 d\sigma_2 \frac{\phi_\mu^*(\sigma_1)\phi_\nu^*(\sigma_2)\phi_{\mu'}(\sigma_1)\phi_{\nu'}(\sigma_2)}{|r_1 - r_2|}$$

where we have used $\sigma_i = (r_i, s_i)$ with r_i the position index and s_i the spin index.

To solve the above Hamiltonian on a quantum computer using the VQD algorithm, the Hamiltonian has to be mapped onto the Pauli operators acting on the qubits that simulate the states of the H_2 molecule. In this work, we will make use of the Parity transformation [230] for this purpose although transformations like Bravyi-Kitaev or Jordan-Wigner can be used.

Using the Parity transformation, the 2 qubit reduced form of the H_2 Hamiltonian is given by [231],

$$H = a_0 II + a_1 ZI + a_2 IZ + a_3 ZZ + a_4 XX \tag{7.9}$$

The values of the coefficients a_i for different internuclear distance can be obtained from the qiskit.chemistry module.

7.2.4 Solving the H_2 Hamiltonian using two-qubit system

To use the variational principle, we will have to vary the states in the qubit space so as to find the state which minimized the energy expectation value. This can be done using the technique of Unitary Coupled Cluster Singles and Doubles (UCCSD). The parametrized ansatz state using UCCSD is given by,

$$|\psi(\theta)\rangle = U(\theta) |\psi_0\rangle \tag{7.10}$$

where, $|\psi_0\rangle$ is an initial reference state and $U(\theta)$ is the UCCSD evolution operator. For the case of H_2 molecule, the UCCSD operator is given by [227],

$$U(\theta) = \exp(\theta(c_2^\dagger c_3^\dagger c_1 c_0 - c_0^\dagger c_1^\dagger c_3 c_2)) \tag{7.11}$$

The choice of the reference state is the Hartree-Fock (HF) state which definitely has support on the ground state of the Hamiltonian. After writing the HF state on the Parity basis, the symmetry in the action of UCCSD operator and the HF state can be exploited to give a 2 qubit UCCSD operator,

$$U(\theta) = \exp(i\theta XY) \tag{7.12}$$

with the HF state given by $|01\rangle$

The action of $U(\theta)$ on $|01\rangle$ can be easily seen to be,

$$\begin{aligned} U(\theta)\,|01\rangle &= \exp(i\theta XY)\,|01\rangle \\ &= \cos\theta\,|01\rangle + \sin\theta\,|10\rangle \end{aligned} \tag{7.13}$$

So the UCCSD ansatz only explores a 2D subspace of the 2 qubit space. The numerical implementation of the VQD with this UCCSD ansatz is shown in the next section. The action of $U(\theta)$ on $|01\rangle$ and then minimization of the energy expectation leads to the ground state of the Hamiltonian. The classical minimization process is done using the Nelder-Mead method given by the minimize function of scipy.optimize module. For the excited state, we have used the VQD modified Hamiltonian and the same ansatz circuit leads to an excited state of the H_2 molecule.

Given that we obtained 2 energy eigenstates of the Hamiltonian in the space spanned by the vectors $|01\rangle, |10\rangle$, to ensure the orthogonality of the eigenstates, it follows that the other two eigenstates must live in the space spanned by the other two computational basis vectors. So to explore this subspace, we use the initial state to be $|00\rangle$ and apply the ansatz circuit which performs the evolution $U(\theta)$, same as in the previous case, given by,

$$\begin{aligned} U(\theta) &= \exp(i\theta XY) \\ U(\theta)\,|00\rangle &= \cos\theta\,|00\rangle - \sin\theta\,|11\rangle \end{aligned} \tag{7.14}$$

The reason this has to give the remaining two eigenvectors is that the H_2 Hamiltonian of Eqn. (7.9) is real on a computational basis and since it is also Hermitian, it follows from theorems of linear algebra that there exists a real eigenbasis for the Hamiltonian. This means, that the coefficients of the computational basis in the expansion of the eigenvectors are real. This implies we don't have to explore the space where the relative phase between the two computational basis vectors is complex.

Like in the previous case, we can obtain the other two eigenstates of the Hamiltonian using the VQD algorithm. Notice, however, that we will not need to utilize the full power of VQD in this case, in the sense that the modified VQD Hamiltonian need not have to include both the eigenstates that were obtained in the previous case. Instead, the two eigenstates lying in the space of $\{|01\rangle, |10\rangle\}$ can be obtained just by treating it as a new problem of diagonalization i.e. finding the ground and the first excited state within this subspace. The reason is that any vector in this subspace is already orthogonal to the two eigenstates obtained earlier and hence the purpose of the modified Hamiltonian of VQD is already satisfied. The numerical results obtained from this method are given in the next section. It turns out, that the excited state obtained from the HF state is actually the third excited state while the excited states obtained starting from $|00\rangle$ are the first and the second excited states.

7.2.5 Solving the H_2 Hamiltonian on a single-qubit system

As was mentioned above, the UCC ansatz only explores a 2D subspace of the 4D space. This creates a possibility of mapping the 2D subspace to a single qubit space such that the whole problem of diagonalization in a subspace of a 2 qubit space is transformed into a diagonalization problem in a single qubit space. This can be achieved as follows.

In the first case, we saw that the parametrized state was given by $\cos\theta\,|01\rangle + \sin\theta\,|10\rangle$ where, the initial state was $|01\rangle$ and the UCC operator was $\exp(i\theta XY)$. Now if we map $|01\rangle$ to $|0\rangle$ and $|10\rangle$ to $|1\rangle$, the UCC operator can be mapped to $\exp(-i\theta Y)$. That is, under the above mapping, we can write

$$\exp(i\theta XY)\,|01\rangle = \exp(-i\theta Y)\,|0\rangle \tag{7.15}$$

Now that the basis and the ansatz are mapped in a consistent manner, it remains to map the Hamiltonian in the 2 qubit space to a single qubit space. This can be done by noting the action of the individual terms of the Hamiltonian on the states $|01\rangle$ and $|10\rangle$.

From the above table, we can directly identify,

$$\begin{gathered} II \longrightarrow I \;\;\&\;\; ZZ \longrightarrow -I \\ ZI \longrightarrow Z \;\;\&\;\; IZ \longrightarrow -Z \\ XX \longrightarrow X \end{gathered}$$

Thus, the diagonalization of the Hamiltonian in the 2D subspace of the 2 qubit space reduces to the diagonalization of the 1D Hamiltonian given by,

$$H = (a_0 - a_3)I + (a_1 - a_2)Z + a_4X \tag{7.16}$$

Table 7.1: The action of the individual terms of the Hamiltonian on the states $|01\rangle$ and $|10\rangle$.

$II\,\|01\rangle$	=	$\|01\rangle$	$II\,\|10\rangle$	=	$\|10\rangle$
$ZI\,\|01\rangle$	=	$\|01\rangle$	$ZI\,\|10\rangle$	=	$-\|10\rangle$
$IZ\,\|01\rangle$	=	$-\|01\rangle$	$IZ\,\|10\rangle$	=	$\|10\rangle$
$ZZ\,\|01\rangle$	=	$-\|01\rangle$	$ZZ\,\|10\rangle$	=	$-\|10\rangle$
$XX\,\|01\rangle$	=	$\|10\rangle$	$XX\,\|10\rangle$	=	$\|01\rangle$

Table 7.2: The action of the individual terms of the Hamiltonian on the states $|00\rangle$ and $|10\rangle$.

$II\,\|00\rangle$	=	$\|00\rangle$	$II\,\|11\rangle$	=	$\|11\rangle$
$ZI\,\|00\rangle$	=	$\|00\rangle$	$ZI\,\|11\rangle$	=	$-\|11\rangle$
$IZ\,\|00\rangle$	=	$\|00\rangle$	$IZ\,\|11\rangle$	=	$-\|11\rangle$
$ZZ\,\|00\rangle$	=	$\|00\rangle$	$ZZ\,\|11\rangle$	=	$\|11\rangle$
$XX\,\|00\rangle$	=	$\|11\rangle$	$XX\,\|11\rangle$	=	$\|00\rangle$

with the UCC ansatz $\exp(-i\theta Y)$ and the initial state $|0\rangle$.

For the remaining two eigenstates we had, the initial state = $|00\rangle$, UCC operator = $\exp(i\theta XY)$. Here, we will map $|00\rangle$ to $|0\rangle$ and $|11\rangle$ to $|1\rangle$. Then the action of the UCC operator can be mapped to $\exp(i\theta Y)$ such that, under the above mapping,

$$\exp(i\theta XY)\,|00\rangle = \exp(i\theta Y)\,|0\rangle \tag{7.17}$$

To map the Hamiltonian, we will again look at the action of its elements on the basis vectors $|00\rangle$ and $|11\rangle$.

Then we can clearly identify,

$$II \longrightarrow I \ \& \ ZZ \longrightarrow I$$
$$ZI \longrightarrow Z \ \& \ IZ \longrightarrow Z$$
$$XX \longrightarrow X$$

Thus the Hamiltonian in the single qubit can be written as,

$$H = (a_0 + a_3)I + (a_1 + a_2)Z + a_4X \tag{7.18}$$

with the UCC ansatz $\exp(i\theta Y)$ and the initial state $|0\rangle$.

Thus, diagonalizing these two Hamiltonians will give all four excited states of the original 2 qubit H_2 Hamiltonian. The reduction of the problem to a single qubit is of course resource efficient for experimental implementation. Also, since it contains only 3 terms in the Hamiltonian, the calculation of energy expectation becomes a lot simpler. Additionally, the UCC ansatz, unlike in the 2 qubit case, is just a rotation about the Y-axis which is trivial to implement on any quantum computer. Last but not least, the initial state can be directly taken to be the pseudo-pure state instead of any requirement to prepare a reference state. With all these advantages, we have shown that the whole problem of diagonalization of the 2 qubit H_2 molecule can be simply recast into a problem of diagonalization in a single qubit space.

7.3 NMR implementation

7.3.1 NMR implementation of energy spectra of H_2 molecule using a two-qubit system

To experimentally calculate the energies simulated by variation quantum algorithms of H_2 molecule on a four-dimensional quantum system, the molecule of ^{13}C enriched chloroform dissolved in acetone-D6 was used, with the ^{13}C and ^{1}H spins being labeled as qubit 1 and qubit 2, respectively(see Fig. 7.2(a)). NMR experiments are only sensitive to the deviation density matrix and the initial state is prepared from the thermal equilibrium into a pseudo pure state (PPS) which can mimic the evolution and observations of true pure states [9];

$$\rho_{00} = \frac{1-\epsilon}{2^3} I_4 + \epsilon |00\rangle\langle 00| \tag{7.19}$$

where $\epsilon \approx 10^{-6}$ and I_4 is 4×4 identity operator. We initialized system in the pseudo pure state (PPS) $|00\rangle$ using the spatial averaging technique [9]. The spatial

averaging technique is implemented in NMR by using a combination of RF pulses and pulsed magnetic gradients and the NMR pulse sequence for the PPS is given in Fig. 7.2(b).

Experiments were performed on a Bruker Avance III 600-MHz FT-NMR spectrometer equipped with a TXI probe. Quantum gates, required for the NMR implementation, were achieved by using the suitable RF pulses of suitable amplitude, phase, and duration and nonlocal unitary operations were achieved by free evolution under the system Hamiltonian. The $T1$ and $T2$ relaxation times of ^{1}H spin-1/2 nuclei are ≈ 8 sec and ≈ 3 sec, respectively. While the $T1$ and $T2$ relaxation times of ^{13}C spin-1/2 nuclei are ≈ 17 sec and ≈ 0.5 sec, respectively. The duration of the $\frac{\pi}{2}$ pulses for ^{1}H and ^{13}C nuclei are $7.14\ s$ at 19.9 W power level, and $12.4\ s$ at a power level of 237.3 W, respectively.

In order to experimentally calculate the energies of the H_2 molecule, we need to calculate the expectation values of $\langle ZI\rangle$, $\langle IZ\rangle$, $\langle ZZ\rangle$, $\langle XX\rangle$. In NMR experiment these expectation values can be calculated experimentally by mapping the $\langle ZI\rangle$, $\langle IZ\rangle$, $\langle ZZ\rangle$, $\langle XX\rangle$ into the single-qubit Pauli Z operator. This mapping is particularly useful in the context of an NMR experimental measurement as in NMR experiment the observed z magnetization of a nuclear spin in a particular quantum state is proportional to the expectation value of the Pauli-Z operator of the spin in that state [107, 209]. For example, in order to determine the expectation value $\langle ZZ\rangle$ for the state, say $\rho = |\psi\rangle\langle\psi|$, we map the state ρ to $\rho_1 = U_1\rho U_1^\dagger$, where $U_1 = CNOT_{12}$ followed by observing $\langle Z_2\rangle$ for the state ρ_1. The expectation value of $\langle Z_2\rangle$ for the state ρ_1 is equivalent to observing the expectation value of $\langle ZZ\rangle$ for the state ρ.

The quantum circuit and corresponding NMR pulse sequence for the experimental calculation of required expectation values are given in Fig. 7.2(c). The circuit contains three parts. The first part is initializing the state in the HF state $|01\rangle$ that can be achieved by applying the single qubit rotation on $|00\rangle$ state. The second part is to apply the parametrized ansatz $U(\theta)$ on the initial state which is achieved by optimizing the value θ and the optimization is done by using the Nelder-Mead method given by the minimize function of scipy.optimize module. The third part is to calculate the expectation values $\langle ZI\rangle$, $\langle IZ\rangle$, $\langle ZZ\rangle$, $\langle XX\rangle$ for the parametrized ansatz, and this is achieved by mapping $\langle ZI\rangle$, $\langle IZ\rangle$, $\langle ZZ\rangle$, $\langle XX\rangle$ into the single-qubit Pauli Z operator. In the end, we will get experimentally calculated energies by adding these expectation values with respective electronic constants ($a_i, i = 0, 1, 2, 3, 4$). The values of the electronic constants is is tabulated in Table 7.3 for the different values of internuclear separations (R).

We have experimentally calculated the ground state and the excited state energies using VQE and VQD algorithms, respectively, for the sixteen internuclear separations (in angstroms) $0.30A^\circ$ - $1.80A^\circ$. For each of the internuclear separations, we have different electronic constant a_0, a_1, a_2, a_3, a_4 the given in H_2 molecule Hamiltonian

7. NMR implementation of variational quantum algorithms to calculate the ground and excited state energies of H_2 molecule

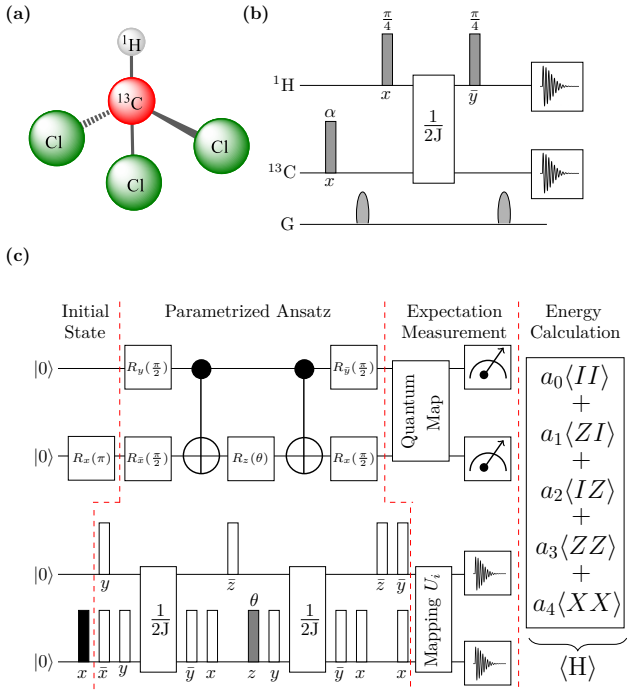

Figure 7.2: (a) Molecular structure of ^{13}C-labeled chloroform used as a two-qubit quantum system. (b) NMR pulse sequence for the PPS $|00\rangle$state where the value of the flip angle α is kept fixed at $59.69°$, while J represents the coupling between the ^{1}H and ^{13}C. $\frac{1}{2\mathrm{J}}$ represents the total time evolution. (c) Quantum circuit for the required state, generated with the optimized value of θ w.r.t. different intermolecular distances. The white rectangles denote π pulses and the black rectangle represents the $\frac{\pi}{2}$ pulse. The flip angles and phases of the other pulses are written below each pulse. Bar over the phase represents the negative phase.

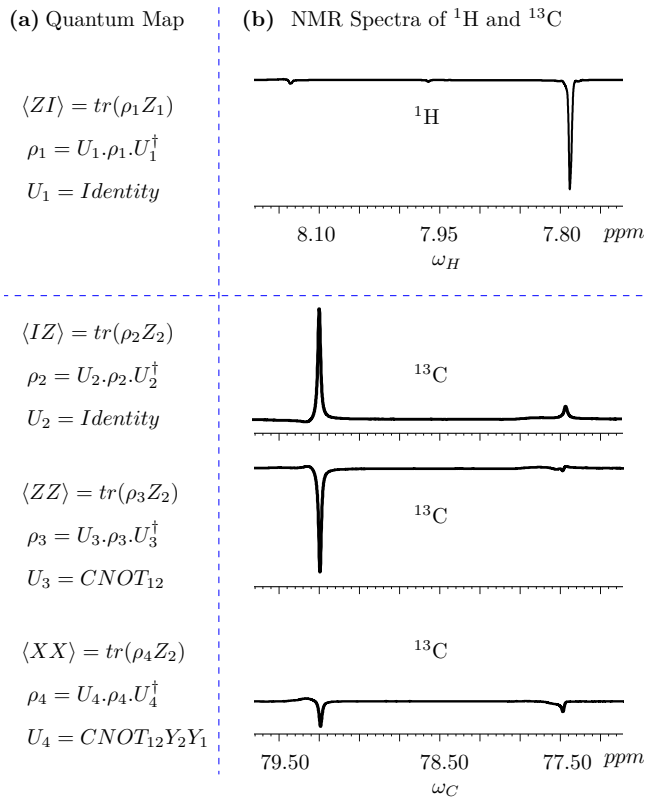

Figure 7.3: (a)Mapping details for the measurement of the expectation values $\langle ZI\rangle$, $\langle IZ\rangle$, $\langle ZZ\rangle$, $\langle XX\rangle$. $Identity$ represents no unitary operation. (b) NMR spectra of ^{1}H, showing the experimentally measured expectation values of $\langle ZI\rangle$ and NMR spectra of ^{13}C, showing the experimentally measured expectation values of $\langle IZ\rangle$, $\langle ZZ\rangle$, $\langle XX\rangle$ respectively for the ground state energy for intermolecular distance $R = 0.70A^\circ$.

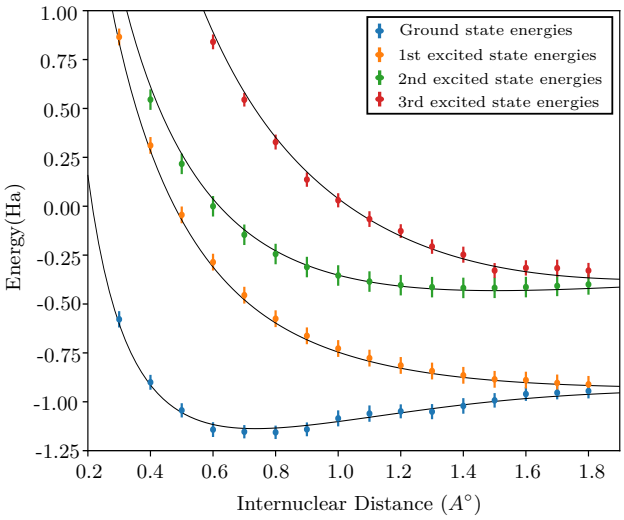

Figure 7.4: All ground and excited state energy levels of H_2 molecule calculated using VQE and VQD algorithms over a range of internuclear separations. Simulated results are represented by joined lines and experimentally calculated values are represented by different points with error bars.

Eqn. (7.9). Fig. 7.3(a) contains the details of mapping that we have used in NMR experiment for the calculation of expectation values required for the experimentally prepared states. Fig. 7.3(b) contains the NMR spectra of $\langle ZI \rangle$, $\langle IZ \rangle$, $\langle ZZ \rangle$, $\langle XX \rangle$ for the ground state energy for the internuclear separation $R = 0.70A^\circ$, obtained after the $\frac{\pi}{2}$ detection RF pulses. In a similar fashion, we have experimentally calculated the ground and excited state energies for the H_2 molecule for other thirteen different internuclear separations. The ground and excited state energies w.r.t. the internuclear separations have been plotted in Fig. 7.4. As can be seen from the graph Fig. 7.4, the simulated values and experimentally measured values agree well with the experimental errors.

7.3.2 NMR implementation of energy spectra of H_2 molecule using a one-qubit system

To experimentally calculate the energies simulated by variation quantum algorithms of H_2 molecule on a two-dimensional quantum system, the molecule of chloroform dissolved in acetone-D6 was used, with ^{1}H spin as a qubit (see Fig. 7.5(a)). This time, we need to calculate the only two expectation values $\langle Z \rangle$, $\langle X \rangle$ for the calculation of energy spectra of H_2 molecule. The mapping details for the experimental calculation

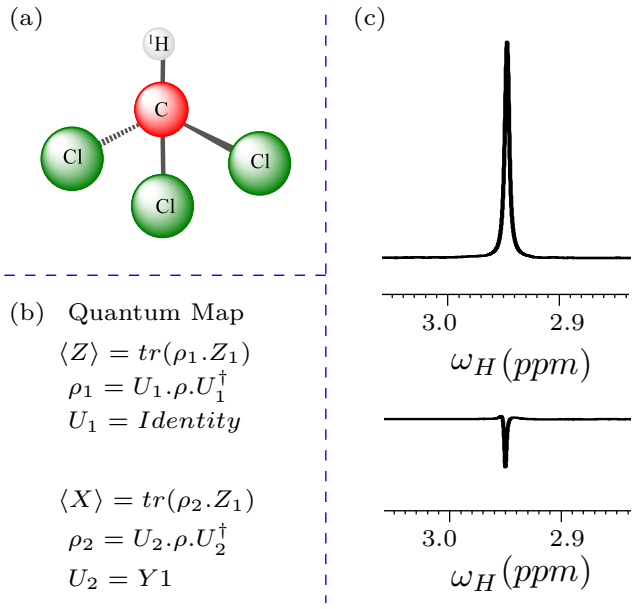

Figure 7.5: (a) Molecular structure of chloroform used as a one-qubit quantum system. (b) Mapping details for the measurement of the expectation values $\langle Z\rangle$, $\langle X\rangle$. $Identity$ represents no unitary operation. (c) NMR spectra of ^{1}H, showing the experimentally measured expectation values of $\langle Z\rangle$ and $\langle X\rangle$

that we used are given in Fig. 7.5(b). Fig. 7.5(c), represents the NMR spectra the expectation values of $\langle Z\rangle$, $\langle X\rangle$ for ground state energy of the H_2 molecule for the internuclear separation $R = 0.70$.

We have experimentally calculated the ground and excited state energies for the H_2 molecule for sixteen different internuclear separations. The ground and excited state energies w.r.t. the internuclear separations have been plotted in Fig. 7.6. The red line curve color denotes the energy calculation corresponding to the reduced single qubit Hamiltonian Eqn. (7.16). The green line curve color denotes the energy calculation corresponding to the reduced single qubit Hamiltonian Eqn. (7.18). As can be seen from the graph Fig. 7.6, the simulated values and experimentally measured values agree well with experimental errors.

The experimental complexity is reduced due to the reduction of the two-qubit system to one qubit system. We are able to calculate the energy spectra of H_2 molecule by measuring the only two expectation values $\langle Z\rangle$, $\langle X\rangle$ and in NMR experiments these can be calculated by a single RF pulse for the experimentally prepared one state. This is the first experimental demonstration on an NMR quantum computer of energy calculation of H_2 molecule that requires only one qubit system.

Table 7.3: Hamiltonian coefficients for Eqn. (7.9) for the different internuclear separation(R).

R (A°)	a_0	a_1	a_2	a_3	a_4
0.30	-0.75374	0.80864	-0.80864	-0.01328	0.16081
0.40	-0.86257	0.68881	-0.68881	-0.01291	0.16451
0.50	-0.94770	0.58307	-0.58307	-0.01251	0.16887
0.60	-1.00712	0.49401	-0.49401	-0.01206	0.17373
0.70	-1.04391	0.42045	-0.42045	-0.01150	0.179005
0.80	-1.06321	0.35995	-0.35995	-0.01080	0.18462
0.90	-1.07028	0.30978	-0.30978	-0.00996	0.19057
1.00	-1.06924	0.26752	-0.26752	-0.00901	0.19679
1.10	-1.06281	0.23139	-0.23139	-0.00799	0.20322
1.20	-1.05267	0.20018	-0.20018	-0.00696	0.20979
1.30	-1.03991	0.17310	-0.17310	-0.00596	0.21641
1.40	-1.02535	0.14956	-0.14956	-0.00503	0.22302
1.50	-1.00964	0.12910	-0.12910	-0.00418	0.22953
1.60	-0.99329	0.11130	-0.11130	-0.00344	0.23590
1.70	-0.97673	0.09584	-0.09584	-0.00280	0.24207
1.80	-0.96028	0.08240	-0.08240	-0.00226	0.24801

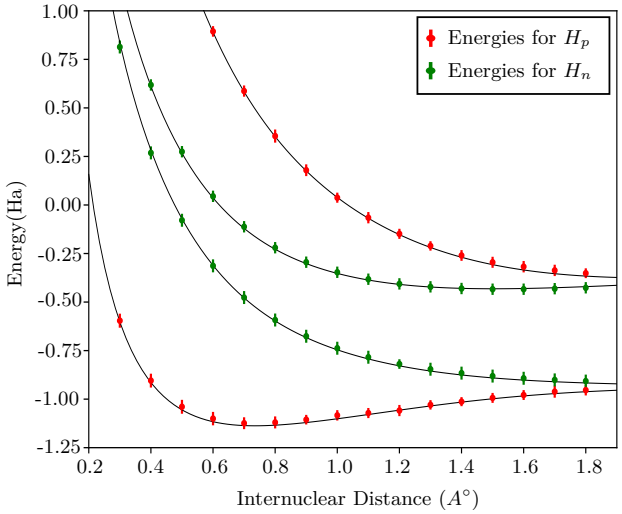

Figure 7.6: All ground and excited state energy levels of H_2 molecule are simulated and experimentally demonstrated over a range of internuclear separations. Simulated results are represented by joined lines and experimentally calculated values are represented by different points with error bars.

7.4 Reducing the three-qubit approximated LiH diagonalization to a single-qubit

Like the case of H_2, the ground state of Lithium hydride (LiH) can also be obtained variationally on a quantum computer. After a few judicious assumptions and reductions, an approximate 3 qubit Hamiltonian for LiH under the BK transformation is given by [227],

$$\begin{aligned} H =& c_0 I + c_1 Z_0 + c_2 Z_1 + c_3 Z_2 + c_4 Z_1 Z_0 + c_5 Z_2 Z_0 \\ &+ c_6 Z_2 Z_1 + c_7 X_1 X_0 + c_8 Y_1 Y_0 + c_9 X_2 X_0 + c_{10} Y_2 Y_0 \\ &+ c_{11} X_2 X_1 + c_{12} Y_2 Y_1 \end{aligned} \tag{7.20}$$

With the UCC operator:

$$U(\alpha, \beta) = e^{-i\alpha X_0 Y_1} e^{-i\beta X_0 Y_2} \tag{7.21}$$

Where the Hartree-Fock state is given by $|111\rangle$. Notice, like in the case of H_2, the action of the above UCC operator just explores a 4-dimensional subspace of the 8-dimensional 3 qubit space. Thus, we see this can be mapped to a 2 qubit system using simple mappings like in the previous case. To explicitly write the mapping, first

consider the exact action of the UCC operator on the Hartree-Fock state.

$$\begin{aligned} U(\alpha,\beta)\,|111\rangle &= e^{-i\alpha X_0 Y_1}(\cos\beta\,|111\rangle - \sin\beta\,|010\rangle) \\ &= \cos\beta(\cos\alpha\,|111\rangle - \sin\alpha\,|001\rangle) \\ &\quad - \sin\beta(\cos\alpha\,|010\rangle - \sin\alpha\,|100\rangle) \end{aligned} \tag{7.22}$$

Now we will map $|111\rangle$ to $|11\rangle$, $|001\rangle$ to $|01\rangle$, $|010\rangle$ to $|10\rangle$ and $|100\rangle$ to $|00\rangle$. Under this mapping, the UCC operator can be transformed as follows.

$$\begin{aligned} &e^{-i\alpha X_0 Y_1} e^{-i\beta X_0 Y_2}\,|111\rangle \\ &= \cos\beta(\cos\alpha\,|111\rangle - \sin\alpha\,|001\rangle) - \sin\beta(\cos\alpha\,|010\rangle \\ &- \sin\alpha\,|100\rangle) \\ &\equiv \cos\beta(\cos\alpha\,|11\rangle - \sin\alpha\,|01\rangle) - \sin\beta(\cos\alpha\,|10\rangle \\ &- \sin\alpha\,|00\rangle) \\ &= \cos\beta(\cos\alpha\,|1\rangle - \sin\alpha\,|0\rangle) \otimes |1\rangle - \sin\beta(\cos\alpha\,|1\rangle \\ &- \sin\alpha\,|0\rangle) \otimes |0\rangle \\ &= (\cos\alpha\,|1\rangle - \sin\alpha\,|0\rangle) \otimes (\cos\beta\,|1\rangle - \sin\beta\,|0\rangle) \\ &= e^{-i\alpha Y_0}\,|1\rangle \otimes e^{-i\beta Y_1}\,|1\rangle \end{aligned} \tag{7.23}$$

Notice, under the above mapping, the ansatz not just reduces to a two-qubit space but also becomes separable in the two-qubit space. This in fact reduces the 3 qubit problem to a single qubit problem as once the states are separable, the process of taking averages of the Hamiltonian can be done independently of each other. Now, the 3 qubit Hamiltonian can also be mapped to a 2 qubit form by noting the action of each of its terms like in the case of H_2, as follows.

$$\begin{gathered} Z_0 \longrightarrow -Z_1Z_0, \quad Z_1 \longrightarrow I_1Z_0, \quad Z_2 \longrightarrow Z_1I_0 \\ Z_1Z_0 \longrightarrow -Z_1I_0, \quad Z_2Z_0 \longrightarrow -I_1Z_0, \quad Z_2Z_1 \longrightarrow Z_1Z_0 \\ X_1X_0 \longrightarrow I_1X_0, \quad X_2X_0 \longrightarrow X_1I_0, \quad X_2X_1 \longrightarrow X_1X_0 \\ Y_1Y_0 \longrightarrow Z_1X_0, \quad Y_2Y_0 \longrightarrow X_1Z_0, \quad Y_2Y_1 \longrightarrow Y_1Y_0 \end{gathered}$$

While of course the identity remains identity. Under this transformation, the Hamiltonian becomes,

$$\begin{aligned} H = {} & c_0I_1I_0 + (-c_1 + c_5)Z_1Z_0 + (c_2 - c_6)I_1Z_0 \\ & + (c_3 - c_4)Z_1I_0 + c_7I_1X_0 + c_8X_1X_0 + c_9X_1I_0 \\ & + c_{10}Z_1X_0 + c_{11}Y_2Y_1 + c_{12}X_1Z_0 \end{aligned} \tag{7.24}$$

So now notice, as the ansatz is a separable state in the 2 qubit space, the problem of finding the expectation value of the above Hamiltonian reduces to just finding the expectation value of the individual Pauli operators $\{I, X, Y, Z\}$ in the single qubit space w.r.t. the state $\exp -i\theta Y \left|1\right\rangle$ where $\theta \in \{\alpha, \beta\}$ and then adding their appropriate combination of products to produce the above Hamiltonian. Hence, the 3 qubit problem is reduced to an effective single qubit problem. Notice, however, that the energy minimization should still be done in a two-parameter space and not one.

7.5 Conclusions

In this chapter, we have obtained the ground and excited states of the H_2 Hamiltonian in the Parity basis using the VQE and VQD algorithms. The corresponding results have been verified on an NMR quantum computer for the first time. Following this, we have shown a simple method to reduce the problem of H_2 to a single qubit problem and have also verified the results on the NMR quantum computer. For the experimental verification, we have used two NMR qubits and the expectation values, involved in the Hamiltonian are calculated experimentally by measuring the single qubit Pauli Z operator of the experimentally prepared state. A similar method has been applied to an approximate Hamiltonian of LiH as given in [225] and has been shown that it can be reduced to a single qubit problem from a three-qubit problem.

The experimental implementation of variational quantum algorithms to calculate the energies of the molecules is important for quantum information processing tasks in the field of quantum chemistry and our results are a step forward in this direction.

7. NMR implementation of variational quantum algorithms to calculate the ground and excited state energies of H_2 molecule

Chapter 8

Summary and future outlook

The thesis focuses on the experimental investigation of quantum contextuality and nonlocality, including their monogamous relationships, on an NMR quantum information processor.

The first two projects describe the experimental study of quantum contextual correlations. The first project focuses on the experimental violation of state-dependent contextuality in which we experimentally demonstrate the violation of two different noncontextual inequalities capable of revealing fully contextual correlations. By decomposing all of the observables in terms of Pauli operators, the expectation values of the involved observables have been calculated, to reduce the need for quantum state tomography. Further, the behavior of both the inequalities is analyzed when the underlying quantum state undergoes a rotation and the results suggest the non-linear nature of the inequality values with respect to the rotation angle of the underlying state. The second project describes the generalized scattering quantum circuit that can carry out non-invasive measurements. We use our generalized quantum circuit to experimentally demonstrate the state-independent contextual inequality, so-called temporal PM inequality. Further, the violation of Bell-type inequality is demonstrated using the quantum scattering circuit.

The next project describes the experimental construction of a symmetric three-qubit entangled state. We use this state to experimentally simulate the tight Bell-type inequality in the (3,2,2) scenario. The presence of entanglement is validated by two entanglement measures, named negativity, and concurrence. Additionally, a theoretical study is conducted to demonstrate how the Bell-type inequality can be employed as a witness for entanglement.

The next two projects describe the study of monogamy of quantum correlations. We first performed the experimental demonstration of the monogamous relationship between contextuality and nonlocality using the ququart-qubit system. Ququart-qubit

system is physically realized in NMR experiments via three NMR qubits, where the first two qubits are clubbed together into a single ququart system. Next, we have developed a theoretical model to derive the monogamy relation between the ENC inequalities using a graph theoretical approach. Then we apply our model to the tripartite Bell-CHSH scenario and derive the monogamy relation between ENC inequalities. Further, we experimentally verify the theoretical results for pure as well as mixed states. Our results show that the monogamy relationship of ENC inequalities is satisfied for both states.

The last project of the thesis describes study of various quantum algorithms and their NMR implementation. We have simulated the ground state energy of the H_2 molecule using the VQE algorithm and verified it experimentally. Further, excited state energies of the H_2 molecule are calculated using the VQD algorithm which is the extension of VQE algorithm. Utilizing the UCCSD method, states are modified in order to identify the one that minimised the energy expectation value. The simulation and experimental demonstration of the energy calculation of the H_2 molecule are presented where the reduced one-qubit system is used instead of a two-qubit system.

In this thesis, we have used an NMR quantum processor as an experimental test bed for the demonstration of foundational concepts of quantum theory. We have constructed a generalized quantum circuit that can perform non-invasive measurements which is hardware-independent i.e. this circuit can be used for other quantum hardwares. Additionally, a theoretical protocol has been established utilizing a graph theoretical approach to derive the monogamous relation between ENC inequalities. Also, we explored the potential applications of hybrid quantum algorithms in the field of quantum chemistry and their NMR experimental implementations. Several non-trivial tasks have been performed experimentally using an NMR quantum information processor, such as calculation of correlation function involving the non-invasive measurements, calculation of entropies, and implementation of hybrid algorithms. The results discussed on this thesis are a step forward in the field of experimental quantum computation.

In general, the thesis explores the experimental demonstration of foundational concepts of quantum theory, including quantum contextuality, nonlocality, and entanglement. These quantum properties have immense applications in the field of secure communication and information theory. Quantum contextuality and nonlocality were investigated separately for many years; however, the development of the monogamy relation between them provides study of these quantum properties simultaneously. A common ground of most quantum applications such as including self-testing, quantum key distribution, device-independent quantum key distribution, and randomness certification, is that they utilize the property of monogamy of correlations. An experimental implementation of such quantum correlations is an important step towards

achieving information processing tasks, for which no classical theory can do better. The loophole free experimental test of such quantum correlations on an NMR quantum processor seems like an unexplored territory and needs to be brought into more focus.

References

[1] M. A. Nielsen and I. L. Chuang, *Quantum Computation and Quantum Information*, Cambridge University Press, Cambridge UK, 2010. 1, 2, 3, 5, 16, 103

[2] P. Benioff, The computer as a physical system: A microscopic quantum mechanical Hamiltonian model of computers as represented by Turing machines, J. Stat. Phys. **22**(5), 563–591 (May 1980). 1

[3] R. P. Feynman, Simulating physics with computers, Int. J. Theor. Phys. **21**(6), 467–488 (Jun 1982). 1

[4] D. Deutsch and R. Penrose, Quantum theory, the church-turing principle and the universal quantum computer, Proc. Royal Soc. A **400**(1818), 97–117 (1985). 1

[5] P. W. Shor, Polynomial-Time Algorithms for Prime Factorization and Discrete Logarithms on a Quantum Computer, SIAM J. Comput. **26**(5), 1484–1509 (1997). 1, 2

[6] L. K. Grover, Quantum mechanics helps in searching for a needle in a haystack, Phys. Rev. Lett. **79**, 325–328 (Jul 1997). 1, 2

[7] R. Shankar, *Principles of Quantum Mechanics*, Springer, USA, 1980. 1

[8] A. Montanaro, Quantum algorithms: an overview, Npj Quant. Inf. **2**(1), 15023 (Jan 2016). 1, 2

[9] I. S. Oliveira, T. J. Bonagamba, R. S. Sarthour, J. C. C. Freitas, and E. R. deAzevedo, *NMR Quantum Information Processing*, Elsevier, Linacre House, Jordan Hill, Oxford OX2 8DP, UK, 2007. 1, 2, 3, 8, 12, 13, 71, 96, 112

[10] T. D. Ladd, F. Jelezko, R. Laflamme, Y. Nakamura, C. Monroe, and J. L. O'Brien, Quantum computers, Nature **464**(7285), 45–53 (Mar 2010). 1

[11] R. Horodecki, P. Horodecki, M. Horodecki, and K. Horodecki, Quantum entanglement, Rev. Mod. Phys. **81**, 865–942 (Jun 2009). 2, 16, 17, 18, 67

[12] R. Demkowicz-Dobrzański, A. Sen(De), U. Sen, and M. Lewenstein, Entanglement enhances security in quantum communication, Phys. Rev. A **80**, 012311 (Jul 2009). 2

[13] D. P. DiVincenzo, The Physical Implementation of Quantum Computation, Fortschritte der Physik **48**(9-11), 771–783 (2000). 7, 11

[14] J. Clarke and F. K. Wilhelm, Superconducting quantum bits, Nature **453**(7198), 1031–1042 (Jun 2008). 7

[15] D. Joy, M. Sabir, B. K. Behera, and P. K. Panigrahi, Implementation of quantum secret sharing and quantum binary voting protocol in the IBM quantum computer, Quantum Inf. Process. **19**(1), 33 (Dec 2019). 7

[16] K. S. Shenoy, D. Y. Sheth, B. K. Behera, and P. K. Panigrahi, Demonstration of a measurement-based adaptation protocol with quantum reinforcement learning on the IBM Q experience platform, Quantum Inf. Process. **19**(5), 161 (Apr 2020). 7

[17] K. Joarder, D. Saha, D. Home, and U. Sinha, Loophole-Free Interferometric Test of Macrorealism Using Heralded Single Photons, PRX Quantum **3**, 010307 (Jan 2022). 7

[18] R. Chatterjee, K. Joarder, S. Chatterjee, B. C. Sanders, and U. Sinha, qkdSim, a Simulation Toolkit for Quantum Key Distribution Including Imperfections: Performance Analysis and Demonstration of the B92 Protocol Using Heralded Photons, Phys. Rev. Applied **14**, 024036 (Aug 2020). 7

[19] E. Knill, R. Laflamme, and G. J. Milburn, A scheme for efficient quantum computation with linear optics, Nature **409**(6816), 46–52 (Jan 2001). 7

[20] A. Biswas, A. Banerji, N. Lal, P. Chandravanshi, R. Kumar, and R. P. Singh, Quantum key distribution with multiphoton pulses: an advantage, Opt. Continuum **1**(1), 68–79 (Jan 2022). 7

[21] A. Anwar, S. Prabhakar, and R. P. Singh, Size-invariant twisted optical modes for the efficient generation of higher-dimensional quantum states, J. Opt. Soc. Am. B **38**(10), 2976–2983 (Oct 2021). 7

[22] P. Neumann, N. Mizuochi, F. Rempp, P. Hemmer, H. Watanabe, S. Yamasaki, V. Jacques, T. Gaebel, F. Jelezko, and J. Wrachtrup, Multipartite Entanglement Among Single Spins in Diamond, Science **320**(5881), 1326–1329 (2008). 7

[23] M. Khokhar, N. Singh, and R. V. Nair, Stacked metasurfaces for enhancing the emission and extraction rate of single nitrogen-vacancy centers in nanodiamond, J. Opt. **24**(2), 024008 (jan 2022). 7

[24] S. Sharma and R. V. Nair, Charge-state conversion in nitrogen-vacancy centers mediated by an engineered photonic environment, Phys. Rev. A **101**, 043420 (Apr 2020). 7

[25] D. G. Cory, A. F. Fahmy, and T. F. Havel, Ensemble quantum computing by NMR spectroscopy, Proc. Nat. Acad. Sci. **94**(5), 1634–1639 (1997). 7, 11, 12

[26] K. Dorai, Arvind, and A. Kumar, Implementing quantum-logic operations, pseudopure states, and the Deutsch-Jozsa algorithm using noncommuting selective pulses in NMR, Phys. Rev. A **61**, 042306 (Mar 2000). 7, 11

[27] A. Chakrabarti and R. Bhattacharyya, Non-Bloch decay of Rabi oscillations in liquid state NMR, EPL (Euro. Phys. Lett.) **121**(5), 57002 (mar 2018). 7

[28] A. Chakrabarti, I. Chakraborty, and R. Bhattacharyya, Dynamic decoupling in the presence of 1D random walk, J. Stat. Mech.: Theory Exp. **2016**(5), 053210 (may 2016). 7

[29] C. D. Bruzewicz, J. Chiaverini, R. McConnell, and J. M. Sage, Trapped-ion quantum computing: Progress and challenges, Appl. Phys. Rev. **6**(2), 021314 (2019). 7

[30] K. Krane, *Introductory Nuclear Physics*, John Wiley & Sons, New York, 1988. 8

[31] J. A. Jones, Quantum computing with NMR, Prog. Nucl. Magn. Reson. Spectrosc. **59**(2), 91–120 (2011). 8

[32] N. A. Gershenfeld and I. L. Chuang, Bulk Spin-Resonance Quantum Computation, Science **275**(5298), 350–356 (1997). 11, 12, 13

[33] L. M. K. Vandersypen and I. L. Chuang, NMR techniques for quantum control and computation, Rev. Mod. Phys. **76**, 1037–1069 (Jan 2005). 11

[34] J. A. Jones, M. Mosca, and R. H. Hansen, Implementation of a quantum search algorithm on a quantum computer, Nature **393**(6683), 344–346 (May 1998). 11

[35] L. M. K. Vandersypen, M. Steffen, G. Breyta, C. S. Yannoni, M. H. Sherwood, and I. L. Chuang, Experimental realization of Shor's quantum factoring algorithm using nuclear magnetic resonance, Nature **414**(6866), 883–887 (Dec 2001). 11

[36] M. Steffen, W. van Dam, T. Hogg, G. Breyta, and I. Chuang, Experimental Implementation of an Adiabatic Quantum Optimization Algorithm, Phys. Rev. Lett. **90**, 067903 (Feb 2003). 11

[37] W. S. Warren, The Usefulness of NMR Quantum Computing, Science **277**(5332), 1688–1690 (1997). 13

[38] E. Knill and R. Laflamme, Power of One Bit of Quantum Information, Phys. Rev. Lett. **81**, 5672–5675 (Dec 1998). 13

[39] D. G. Cory, M. D. Price, and T. F. Havel, Nuclear magnetic resonance spectroscopy: An experimentally accessible paradigm for quantum computing, Physica D **120**(1), 82–101 (1998), Proceedings of the Fourth Workshop on Physics and Consumption. 13, 71

[40] S. S. Roy and T. S. Mahesh, Initialization of NMR quantum registers using long-lived singlet states, Phys. Rev. A **82**, 052302 (Nov 2010). 13

[41] X. Peng, X. Zhu, X. Fang, M. Feng, K. Gao, X. Yang, and M. Liu, Preparation of pseudo-pure states by line-selective pulses in nuclear magnetic resonance, Chem. Phys. Lett. **340**(5), 509–516 (2001). 13

[42] G. M. Leskowitz and L. J. Mueller, State interrogation in nuclear magnetic resonance quantum-information processing, Phys. Rev. A **69**, 052302 (May 2004). 15, 16, 34

[43] G. L. Long, H. Y. Yan, and Y. Sun, Analysis of density matrix reconstruction in NMR quantum computing, J. Opt. B: Quan. Sem. Opt. **3**(6), 376–381 (nov 2001). 16

[44] J. Sakurai, *Modern Quantum Mechanics*, Addison-Wesley, USA, 1994. 16

[45] I. L. Chuang, N. A. Gershenfeld, M. Kubinec, and D. W. Leung, Bulk quantum computation with nuclear magnetic resonance: theory and experiment, Proceedings of the Royal Society of London. Series A: Mathematical, Physical and Engineering Sciences **454**, 447 – 467 (1998). 16

[46] A. Uhlmann, Transition Probability (Fidelity) and Its Relatives, Found. Phys. **41**(3), 288–298 (Mar 2011). 16

[47] R. Jozsa, Fidelity for Mixed Quantum States, J. Mod. Opt. **41**(12), 2315–2323 (1994). 16

[48] E. Schrödinger, Die gegenwärtige Situation in der Quantenmechanik, Naturwissenschaften **23**(48), 807–812 (Nov 1935). 16

[49] O. Guhne and G. Toth, Entanglement detection, Phys. Rep. **474**(1), 1–75 (2009). 17, 67

[50] M. Horodecki, P. Horodecki, and R. Horodecki, Separability of mixed states: necessary and sufficient conditions, Phys. Lett. A **223**(1), 1–8 (1996). 17

[51] U. T. Bhosale and A. Lakshminarayan, Simple permutation-based measure of quantum correlations and maximally-3-tangled states, Phys. Rev. A **94**, 022344 (Aug 2016). 17

[52] N. Ganguly, S. Adhikari, and A. S. Majumdar, Common entanglement witnesses and their characteristics, Quant. Inf. Proc. **12**(1), 425–436 (Jan 2013). 17

[53] W. K. Wootters, Entanglement of Formation of an Arbitrary State of Two Qubits, Phys. Rev. Lett. **80**, 2245–2248 (Mar 1998). 17, 74

[54] G. Vidal and R. F. Werner, Computable measure of entanglement, Phys. Rev. A **65**, 032314 (Feb 2002). 17, 73

[55] J. S. Bell, On the Einstein Podolsky Rosen paradox, Physics **1**, 195–200 (Nov 1964). 18, 21, 49, 68

[56] J. S. BELL, On the Problem of Hidden Variables in Quantum Mechanics, Rev. Mod. Phys. **38**, 447–452 (Jul 1966). 18, 27

[57] D. Home, D. Saha, and S. Das, Multipartite Bell-type inequality by generalizing Wigner's argument, Phys. Rev. A **91**, 012102 (Jan 2015). 18, 68

[58] S. Kochen and E. P. Specker, The Problem of Hidden Variables in Quantum Mechanics, J. Math. Mech. **17**, 59–87 (1967). 18, 27, 49

[59] R. Raussendorf, Contextuality in measurement-based quantum computation, Phys. Rev. A **88**, 022322 (Aug 2013). 18, 27

[60] Y.-C. Liang, R. W. Spekkens, and H. M. Wiseman, Specker's parable of the overprotective seer: A road to contextuality, nonlocality and complementarity, Phys. Rep. **506**(1), 1–39 (2011). 18, 27

[61] A. A. Klyachko, M. A. Can, S. Binicioğlu, and A. S. Shumovsky, Simple Test for Hidden Variables in Spin-1 Systems, Phys. Rev. Lett. **101**, 020403 (Jul 2008). 18, 19, 27, 28, 50

[62] J. F. Clauser, M. A. Horne, A. Shimony, and R. A. Holt, Proposed Experiment to Test Local Hidden-Variable Theories, Phys. Rev. Lett. **23**, 880–884 (Oct 1969). 18, 21

[63] S. Popescu and D. Rohrlich, Which states violate Bell's inequality maximally?, Phys. Lett. A **169**(6), 411–414 (1992). 18

[64] S. L. Braunstein, A. Mann, and M. Revzen, Maximal violation of Bell inequalities for mixed states, Phys. Rev. Lett. **68**, 3259–3261 (Jun 1992). 18

[65] E. Diamanti, H.-K. Lo, B. Qi, and Z. Yuan, Practical challenges in quantum key distribution, Npj. Quant. Inf. **2**(1), 16025 (Nov 2016). 18

[66] R. Ramanathan, A. Soeda, P. Kurzyński, and D. Kaszlikowski, Generalized Monogamy of Contextual Inequalities from the No-Disturbance Principle, Phys. Rev. Lett. **109**, 050404 (Aug 2012). 18, 77, 92

[67] D. Saha and R. Ramanathan, Activation of monogamy in nonlocality using local contextuality, Phys. Rev. A **95**, 030104 (Mar 2017). 18, 78

[68] E. Nagali, V. D'Ambrosio, F. Sciarrino, and A. Cabello, Experimental Observation of Impossible-to-Beat Quantum Advantage on a Hybrid Photonic System, Phys. Rev. Lett. **108**, 090501 (Feb 2012). 18, 27, 28, 29, 30, 50

[69] S. Dogra, K. Dorai, and Arvind, Experimental demonstration of quantum contextuality on an NMR qutrit, Phys. Lett. A **380**(22), 1941–1946 (2016). 18, 28, 50

[70] D. L. Moehring, M. J. Madsen, B. B. Blinov, and C. Monroe, Experimental Bell Inequality Violation with an Atom and a Photon, Phys. Rev. Lett. **93**, 090410 (Aug 2004). 18

[71] X. Zhan, X. Zhang, J. Li, Y. Zhang, B. C. Sanders, and P. Xue, Realization of the Contextuality-Nonlocality Tradeoff with a Qubit-Qutrit Photon Pair, Phys. Rev. Lett. **116**, 090401 (Feb 2016). 18, 78, 85

[72] S. Haldar, S. Roy, T. Chanda, A. Sen(De), and U. Sen, Multipartite entanglement at dynamical quantum phase transitions with nonuniformly spaced criticalities, Phys. Rev. B **101**, 224304 (Jun 2020). 18

[73] A. Bera, S. Mal, A. Sen(De), and U. Sen, Witnessing bipartite entanglement sequentially by multiple observers, Phys. Rev. A **98**, 062304 (Dec 2018). 18

[74] B. Jonnadula, P. Mandayam, K. Życzkowski, and A. Lakshminarayan, Entanglement measures of bipartite quantum gates and their thermalization under arbitrary interaction strength, Phys. Rev. Research **2**, 043126 (Oct 2020). 18

[75] A. Seshadri, V. Madhok, and A. Lakshminarayan, Tripartite mutual information, entanglement, and scrambling in permutation symmetric systems with an application to quantum chaos, Phys. Rev. E **98**, 052205 (Nov 2018). 18

[76] S. López-Rosa, Z.-P. Xu, and A. Cabello, Maximum nonlocality in the (3,2,2) scenario, Phys. Rev. A **94**, 062121 (Dec 2016). 18, 68, 69, 70

[77] A. Cabello, M. Kleinmann, and C. Budroni, Necessary and Sufficient Condition for Quantum State-Independent Contextuality, Phys. Rev. Lett. **114**, 250402 (Jun 2015). 20, 27, 28, 50

[78] S. Yu and C. H. Oh, State-Independent Proof of Kochen-Specker Theorem with 13 Rays, Phys. Rev. Lett. **108**, 030402 (Jan 2012). 20

[79] A. Peres, Incompatible results of quantum measurements, Phys. Lett. A **151**(3), 107–108 (1990). 20, 50

[80] O. Gühne, C. Budroni, A. Cabello, M. Kleinmann, and J.-A. Larsson, Bounding the quantum dimension with contextuality, Phys. Rev. A **89**, 062107 (Jun 2014). 20, 21, 50, 58

[81] A. Cabello, Experimentally Testable State-Independent Quantum Contextuality, Phys. Rev. Lett. **101**, 210401 (Nov 2008). 21, 58

[82] A. Einstein, B. Podolsky, and N. Rosen, Can Quantum-Mechanical Description of Physical Reality Be Considered Complete?, Phys. Rev. **47**, 777–780 (May 1935). 21

[83] M. Howard, J. Wallman, V. Veitch, and J. Emerson, Contextuality supplies the 'magic' for quantum computation, Nat. **510**(7505), 351–355 (Jun 2014). 27

[84] J. Singh, K. Bharti, and Arvind, Quantum key distribution protocol based on contextuality monogamy, Phys. Rev. A **95**, 062333 (Jun 2017). 27, 50

[85] A. Acín, T. Fritz, A. Leverrier, and A. B. Sainz, A Combinatorial Approach to Nonlocality and Contextuality, Commun. Math. Phys. **334**(2), 533–628 (Mar 2015). 27

[86] M. Araújo, M. T. Quintino, C. Budroni, M. T. Cunha, and A. Cabello, All noncontextuality inequalities for the n-cycle scenario, Phys. Rev. A **88**, 022118 (Aug 2013). 27

[87] P. Kurzyński and D. Kaszlikowski, Contextuality of almost all qutrit states can be revealed with nine observables, Phys. Rev. A **86**, 042125 (Oct 2012). 27, 50

[88] P. Lisoněk, P. Badziąg, J. R. Portillo, and A. Cabello, Kochen-Specker set with seven contexts, Phys. Rev. A **89**, 042101 (Apr 2014). 27

[89] A. Cabello, Correlations without parts, Nature **474**(7352), 456–458 (Jun 2011). 27

[90] A. Cabello, Twin inequality for fully contextual quantum correlations, Phys. Rev. A **87**, 010104 (Jan 2013). 27, 28, 38, 50

[91] G. Chiribella, G. M. D'Ariano, and P. Perinotti, Informational derivation of quantum theory, Phys. Rev. A **84**, 012311 (Jul 2011). 27

[92] H. Barnum, S. Beigi, S. Boixo, M. B. Elliott, and S. Wehner, Local Quantum Measurement and No-Signaling Imply Quantum Correlations, Phys. Rev. Lett. **104**, 140401 (Apr 2010). 27

[93] A. Peres, Two simple proofs of the Kochen-Specker theorem, J. Phys. A: Math. Gen. **24**(4), L175–L178 (feb 1991). 28

[94] A. R. Plastino and A. Cabello, State-independent quantum contextuality for continuous variables, Phys. Rev. A **82**, 022114 (Aug 2010). 28

[95] P. Badziąg, I. Bengtsson, A. Cabello, and I. Pitowsky, Universality of State-Independent Violation of Correlation Inequalities for Noncontextual Theories, Phys. Rev. Lett. **103**, 050401 (Jul 2009). 28

[96] P. Kurzyński and D. Kaszlikowski, Contextuality of almost all qutrit states can be revealed with nine observables, Phys. Rev. A **86**, 042125 (Oct 2012). 28

[97] E. Amselem, M. Rådmark, M. Bourennane, and A. Cabello, State-Independent Quantum Contextuality with Single Photons, Phys. Rev. Lett. **103**, 160405 (Oct 2009). 28, 50

[98] C. Zu, Y.-X. Wang, D.-L. Deng, X.-Y. Chang, K. Liu, P.-Y. Hou, H.-X. Yang, and L.-M. Duan, State-Independent Experimental Test of Quantum Contextuality in an Indivisible System, Phys. Rev. Lett. **109**, 150401 (Oct 2012). 28, 50

[99] V. D'Ambrosio, I. Herbauts, E. Amselem, E. Nagali, M. Bourennane, F. Sciarrino, and A. Cabello, Experimental Implementation of a Kochen-Specker Set of Quantum Tests, Phys. Rev. X **3**, 011012 (Feb 2013). 28, 50

[100] Y.-F. Huang, M. Li, D.-Y. Cao, C. Zhang, Y.-S. Zhang, B.-H. Liu, C.-F. Li, and G.-C. Guo, Experimental test of state-independent quantum contextuality of an indivisible quantum system, Phys. Rev. A **87**, 052133 (May 2013). 28, 50

[101] X. Zhang, M. Um, J. Zhang, S. An, Y. Wang, D.-l. Deng, C. Shen, L.-M. Duan, and K. Kim, State-Independent Experimental Test of Quantum Contextuality with a Single Trapped Ion, Phys. Rev. Lett. **110**, 070401 (Feb 2013). 28, 50

[102] F. M. Leupold, M. Malinowski, C. Zhang, V. Negnevitsky, A. Cabello, J. Alonso, and J. P. Home, Sustained State-Independent Quantum Contextual Correlations from a Single Ion, Phys. Rev. Lett. **120**, 180401 (May 2018). 28, 50

[103] H. Bartosik, J. Klepp, C. Schmitzer, S. Sponar, A. Cabello, H. Rauch, and Y. Hasegawa, Experimental Test of Quantum Contextuality in Neutron Interferometry, Phys. Rev. Lett. **103**, 040403 (Jul 2009). 28, 50

[104] O. Moussa, C. A. Ryan, D. G. Cory, and R. Laflamme, Testing Contextuality on Quantum Ensembles with One Clean Qubit, Phys. Rev. Lett. **104**, 160501 (Apr 2010). 28, 50

[105] E. Amselem, L. E. Danielsen, A. J. López-Tarrida, J. R. Portillo, M. Bourennane, and A. Cabello, Experimental Fully Contextual Correlations, Phys. Rev. Lett. **108**, 200405 (May 2012). 30

[106] A. Singh, H. Singh, K. Dorai, and Arvind, Experimental classification of entanglement in arbitrary three-qubit pure states on an NMR quantum information processor, Phys. Rev. A **98**, 032301 (Sep 2018). 32, 84

[107] A. Gaikwad, D. Rehal, A. Singh, Arvind, and K. Dorai, Experimental demonstration of selective quantum process tomography on an NMR quantum information processor, Phys. Rev. A **97**, 022311 (Feb 2018). 32, 33, 113

[108] H. Singh, Arvind, and K. Dorai, Experimental protection of arbitrary states in a two-qubit subspace by nested Uhrig dynamical decoupling, Phys. Rev. A **95**, 052337 (May 2017). 34

[109] J. Zhang, A. M. Souza, F. D. Brandao, and D. Suter, Protected Quantum Computing: Interleaving Gate Operations with Dynamical Decoupling Sequences, Phys. Rev. Lett. **112**, 050502 (Feb 2014). 34

[110] H. Singh, Arvind, and K. Dorai, Constructing valid density matrices on an NMR quantum information processor via maximum likelihood estimation, Phys. Lett. A **380**(38), 3051–3056 (2016). 34

[111] A. Mitra, K. Sivapriya, and A. Kumar, Experimental implementation of a three qubit quantum game with corrupt source using nuclear magnetic resonance quantum information processor, J. Magn. Reson. **187**(2), 306–313 (2007). 43, 96

[112] A. Einstein, B. Podolsky, and N. Rosen, Can Quantum-Mechanical Description of Physical Reality Be Considered Complete?, Phys. Rev. **47**, 777–780 (May 1935). 49, 67

[113] J.-Å. Larsson, A Kochen-Specker inequality, Europhys. Lett. (EPL) **58**(6), 799–805 (jun 2002). 49

[114] C. Simon, i. c. v. Brukner, and A. Zeilinger, Hidden-Variable Theorems for Real Experiments, Phys. Rev. Lett. **86**, 4427–4430 (May 2001). 49

[115] Z.-P. Xu, J.-L. Chen, and O. Gühne, Proof of the Peres Conjecture for Contextuality, Phys. Rev. Lett. **124**, 230401 (Jun 2020). 49

[116] A. S. Arora, K. Bharti, and Arvind, Revisiting the admissibility of non-contextual hidden variable models in quantum mechanics, Phys. Lett. A **383**(9), 833–837 (2019). 49

[117] A. Sohbi, I. Zaquine, E. Diamanti, and D. Markham, Logical and inequality-based contextuality for qudits, Phys. Rev. A **94**, 032114 (Sep 2016). 50

[118] N. D. Mermin, Simple unified form for the major no-hidden-variables theorems, Phys. Rev. Lett. **65**, 3373–3376 (Dec 1990). 50, 68

[119] A. J. Leggett and A. Garg, Quantum mechanics versus macroscopic realism: Is the flux there when nobody looks?, Phys. Rev. Lett. **54**, 857–860 (Mar 1985). 50

[120] D. Avis, P. Hayden, and M. M. Wilde, Leggett-Garg inequalities and the geometry of the cut polytope, Phys. Rev. A **82**, 030102 (Sep 2010). 50, 56

[121] F. Costa, M. Ringbauer, M. E. Goggin, A. G. White, and A. Fedrizzi, Unifying framework for spatial and temporal quantum correlations, Phys. Rev. A **98**, 012328 (Jul 2018). 50

[122] A. Rai, D. Home, and A. S. Majumdar, Leggett-type nonlocal realistic inequalities without any constraint on the geometrical alignment of measurement settings, Phys. Rev. A **84**, 052115 (Nov 2011). 50

[123] D. Saha, S. Mal, P. K. Panigrahi, and D. Home, Wigner's form of the Leggett-Garg inequality, the no-signaling-in-time condition, and unsharp measurements, Phys. Rev. A **91**, 032117 (Mar 2015). 50

[124] G.-Z. Pan, G. Zhang, and Q.-H. Sun, Testing Temporal Contextuality with Quantum Entangled Histories, Int. J. Theor. Phys. **58**(8), 2550–2555 (Aug 2019). 50

[125] M. Ringbauer, F. Costa, M. E. Goggin, A. G. White, and A. Fedrizzi, Multitime quantum correlations with no spatial analog, Npj. Quant. Inf. **4**(1), 37 (Aug 2018). 50

[126] B. S. Tsirel'son, Quantum analogues of the Bell inequalities. The case of two spatially separated domains, J. Sov. Math. **36**(4), 557–570 (Feb 1987). 50, 59

[127] M. Navascués, S. Pironio, and A. Acín, Bounding the Set of Quantum Correlations, Phys. Rev. Lett. **98**, 010401 (Jan 2007). 50, 59

[128] T. Fritz, Quantum correlations in the temporal Clauser–Horne–Shimony–Holt (CHSH) scenario, New J. Phys. **12**(8), 083055 (aug 2010). 50, 56, 59

[129] S. Mal and A. Majumdar, Optimal violation of the Leggett-Garg inequality for arbitrary spin and emergence of classicality through unsharp measurements, Phys. Lett. A **380**(29), 2265–2270 (2016). 50

[130] C. Budroni and C. Emary, Temporal Quantum Correlations and Leggett-Garg Inequalities in Multilevel Systems, Phys. Rev. Lett. **113**, 050401 (Jul 2014). 50

[131] M. Markiewicz, P. Kurzyński, J. Thompson, S.-Y. Lee, A. Soeda, T. Paterek, and D. Kaszlikowski, Unified approach to contextuality, nonlocality, and temporal correlations, Phys. Rev. A **89**, 042109 (Apr 2014). 50, 56, 60

[132] M. E. Goggin, M. P. Almeida, M. Barbieri, B. P. Lanyon, J. L. O'Brien, A. G. White, and G. J. Pryde, Violation of the Leggett-Garg inequality with weak measurements of photons, Proc. Natl. Acad. Sci. **108**(4), 1256–1261 (2011). 50

[133] J. Dressel, C. J. Broadbent, J. C. Howell, and A. N. Jordan, Experimental Violation of Two-Party Leggett-Garg Inequalities with Semiweak Measurements, Phys. Rev. Lett. **106**, 040402 (Jan 2011). 50

[134] C. Budroni, G. Vitagliano, G. Colangelo, R. J. Sewell, O. Gühne, G. Tóth, and M. W. Mitchell, Quantum Nondemolition Measurement Enables Macroscopic Leggett-Garg Tests, Phys. Rev. Lett. **115**, 200403 (Nov 2015). 50

[135] M. Marchese, H. McAleese, A. Bassi, and M. Paternostro, A macrorealistic test in hybrid quantum optomechanics, J. Phys. B: At. Mol. Opt. Phys. **53**(7), 075401 (mar 2020). 50

[136] A. M. Souza, I. S. Oliveira, and R. S. Sarthour, A scattering quantum circuit for measuring Bell's time inequality: a nuclear magnetic resonance demonstration using maximally mixed states, New J. Phys. **13**(5), 053023 (may 2011). 50, 51

[137] V. Athalye, S. S. Roy, and T. S. Mahesh, Investigation of the Leggett-Garg Inequality for Precessing Nuclear Spins, Phys. Rev. Lett. **107**, 130402 (Sep 2011). 50

[138] H. Katiyar, A. Shukla, K. R. K. Rao, and T. S. Mahesh, Violation of entropic Leggett-Garg inequality in nuclear spins, Phys. Rev. A **87**, 052102 (May 2013). 50, 87

[139] H. Katiyar, A. Brodutch, D. Lu, and R. Laflamme, Experimental violation of the Leggett–Garg inequality in a three-level system, New J. Phys. **19**(2), 023033 (feb 2017). 50

[140] S.-S. Majidy, H. Katiyar, G. Anikeeva, J. Halliwell, and R. Laflamme, Exploration of an augmented set of Leggett-Garg inequalities using a noninvasive continuous-in-time velocity measurement, Phys. Rev. A **100**, 042325 (Oct 2019). 50

[141] L. Rosales-Zárate, B. Opanchuk, Q. Y. He, and M. D. Reid, Leggett-Garg tests of macrorealism for bosonic systems including double-well Bose-Einstein condensates and atom interferometers, Phys. Rev. A **97**, 042114 (Apr 2018). 50

[142] E. Huffman and A. Mizel, Violation of noninvasive macrorealism by a superconducting qubit: Implementation of a Leggett-Garg test that addresses the clumsiness loophole, Phys. Rev. A **95**, 032131 (Mar 2017). 50

[143] S.-S. Majidy, H. Katiyar, G. Anikeeva, J. Halliwell, and R. Laflamme, Exploration of an augmented set of Leggett-Garg inequalities using a noninvasive continuous-in-time velocity measurement, Phys. Rev. A **100**, 042325 (Oct 2019). 55

[144] A. Uhlmann, The "transition probability" in the state space of a star-algebra, Rep. Math.l Phys. **9**(2), 273–279 (1976).

[145] M. Huber, H. Schimpf, A. Gabriel, C. Spengler, D. Bruß, and B. C. Hiesmayr, Experimentally implementable criteria revealing substructures of genuine multipartite entanglement, Phys. Rev. A **83**, 022328 (Feb 2011). 67

[146] R. T. Thew, K. Nemoto, A. G. White, and W. J. Munro, Qudit quantum-state tomography, Phys. Rev. A **66**, 012303 (Jul 2002). 67

[147] J. M. Arrazola, O. Gittsovich, and N. Lütkenhaus, Accessible nonlinear entanglement witnesses, Phys. Rev. A **85**, 062327 (Jun 2012). 67

[148] W. Dür, G. Vidal, and J. I. Cirac, Three qubits can be entangled in two inequivalent ways, Phys. Rev. A **62**, 062314 (Nov 2000). 67, 70

[149] C. Sabín and G. García-Alcaine, A classification of entanglement in three-qubit systems, Eur. Phys. J. D **48**(3), 435–442 (Jul 2008). 67

[150] J. K. Stockton, J. M. Geremia, A. C. Doherty, and H. Mabuchi, Characterizing the entanglement of symmetric many-particle spin-$\frac{1}{2}$ systems, Phys. Rev. A **67**, 022112 (Feb 2003). 67

[151] M. Hayashi, D. Markham, M. Murao, M. Owari, and S. Virmani, Entanglement of multiparty-stabilizer, symmetric, and antisymmetric states, Phys. Rev. A **77**, 012104 (Jan 2008). 67

[152] G. Tóth and O. Gühne, Entanglement and Permutational Symmetry, Phys. Rev. Lett. **102**, 170503 (May 2009). 67

[153] P. Mathonet, S. Krins, M. Godefroid, L. Lamata, E. Solano, and T. Bastin, Entanglement equivalence of N-qubit symmetric states, Phys. Rev. A **81**, 052315 (May 2010). 67

[154] M. Aulbach, D. Markham, and M. Murao, The maximally entangled symmetric state in terms of the geometric measure, New J. Phys. **12**(7), 073025 (jul 2010). 67

[155] M. Aulbach, Classification of Entanglement in Symmetric States, Int. J. Quant. Inf. **10**(07), 1230004 (2012). 67

[156] A. Burchardt, J. Czartowski, and K. Życzkowski, Entanglement in highly symmetric multipartite quantum states, Phys. Rev. A **104**, 022426 (Aug 2021). 67

[157] S. Dogra, K. Dorai, and Arvind, Experimental construction of generic three-qubit states and their reconstruction from two-party reduced states on an NMR quantum information processor, Phys. Rev. A **91**, 022312 (Feb 2015). 68

[158] D. Das, S. Dogra, K. Dorai, and Arvind, Experimental construction of a W superposition state and its equivalence to the Greenberger-Horne-Zeilinger state under local filtration, Phys. Rev. A **92**, 022307 (Aug 2015). 68

[159] H. Singh, Arvind, and K. Dorai, Evolution of tripartite entangled states in a decohering environment and their experimental protection using dynamical decoupling, Phys. Rev. A **97**, 022302 (Feb 2018). 68, 70, 71

[160] A. Peres, All the Bell Inequalities, Found. Phys. **29**(4), 589–614 (Apr 1999). 68, 69

[161] H. Buhrman, R. Cleve, S. Massar, and R. de Wolf, Nonlocality and communication complexity, Rev. Mod. Phys. **82**, 665–698 (Mar 2010). 68

[162] B. Reznik, Y. Aharonov, and B. Groisman, Remote operations and interactions for systems of arbitrary-dimensional Hilbert space: State-operator approach, Phys. Rev. A **65**, 032312 (Feb 2002). 68

[163] H. Ozeki and S. Ishizaka, Quantum limit of genuine tripartite correlations by bipartite extremality, Int. J. Quant. Inf. **18**(04), 2050014 (2020). 68

[164] K. Anjali, A. S. Hejamadi, H. S. Karthik, S. Sahu, Sudha, and A. R. U. Devi, Characterizing nonlocality of pure symmetric three-qubit states, Quant. Inf. Process. **20**(5), 187 (May 2021). 68

[165] L. Tendick, H. Kampermann, and D. Bruß, Quantifying necessary quantum resources for nonlocality, Phys. Rev. Research **4**, L012002 (Jan 2022). 68

[166] Y.-C. Liang, T. Vértesi, and N. Brunner, Semi-device-independent bounds on entanglement, Phys. Rev. A **83**, 022108 (Feb 2011). 68

[167] R. F. Werner, Quantum states with Einstein-Podolsky-Rosen correlations admitting a hidden-variable model, Phys. Rev. A **40**, 4277–4281 (Oct 1989). 68

[168] A. Acín, N. Gisin, and B. Toner, Grothendieck's constant and local models for noisy entangled quantum states, Phys. Rev. A **73**, 062105 (Jun 2006). 68

[169] D. Cavalcanti, L. Guerini, R. Rabelo, and P. Skrzypczyk, General Method for Constructing Local Hidden Variable Models for Entangled Quantum States, Phys. Rev. Lett. **117**, 190401 (Nov 2016). 68

[170] T. Heinosaari, J. Kiukas, and D. Reitzner, Noise robustness of the incompatibility of quantum measurements, Phys. Rev. A **92**, 022115 (Aug 2015). 68

[171] R. Uola, T. Moroder, and O. Gühne, Joint Measurability of Generalized Measurements Implies Classicality, Phys. Rev. Lett. **113**, 160403 (Oct 2014). 68

[172] M. T. Quintino, J. Bowles, F. Hirsch, and N. Brunner, Incompatible quantum measurements admitting a local-hidden-variable model, Phys. Rev. A **93**, 052115 (May 2016). 68

[173] E. Bene and T. Vértesi, Measurement incompatibility does not give rise to Bell violation in general, New J. Phys. **20**(1), 013021 (jan 2018). 68

[174] S.-L. Chen, N. Miklin, C. Budroni, and Y.-N. Chen, Device-independent quantification of measurement incompatibility, Phys. Rev. Research **3**, 023143 (May 2021). 68

[175] A. Acín, T. Durt, N. Gisin, and J. I. Latorre, Quantum nonlocality in two three-level systems, Phys. Rev. A **65**, 052325 (May 2002). 68

[176] C. Erven, E. Meyer-Scott, K. Fisher, J. Lavoie, B. L. Higgins, Z. Yan, C. J. Pugh, J.-P. Bourgoin, R. Prevedel, L. K. Shalm, L. Richards, N. Gigov, R. Laflamme, G. Weihs, T. Jennewein, and K. J. Resch, Experimental three-photon quantum nonlocality under strict locality conditions, Nat. Photon. **8**(4), 292–296 (Apr 2014). 68

[177] H. S. Poh, S. K. Joshi, A. Cerè, A. Cabello, and C. Kurtsiefer, Approaching Tsirelson's Bound in a Photon Pair Experiment, Phys. Rev. Lett. **115**, 180408 (Oct 2015). 68

[178] H. Anwer, M. Nawareg, A. Cabello, and M. Bourennane, Experimental test of maximal tripartite nonlocality using an entangled state and local measurements that are maximally incompatible, Phys. Rev. A **100**, 022104 (Aug 2019). 68, 70

[179] B. P. Lanyon, M. Zwerger, P. Jurcevic, C. Hempel, W. Dür, H. J. Briegel, R. Blatt, and C. F. Roos, Experimental Violation of Multipartite Bell Inequalities with Trapped Ions, Phys. Rev. Lett. **112**, 100403 (Mar 2014). 68

[180] D. Singh, Arvind, and K. Dorai, Experimental simulation of a monogamy relation between quantum contextuality and nonlocality on an NMR quantum processor, J. Mag. Reson. Open **10-11**, 100058 (2022). 69

[181] C. Sliwa, Symmetries of the Bell correlation inequalities, Phys. Lett. A **317**(3), 165–168 (2003). 70

[182] A. Singh, D. Singh, V. Gulati, K. Dorai, and Arvind, Experimental detection of non-local correlations using a local measurement-based hierarchy on an NMR quantum processor, Eur. Phys. J. D **74**(8), 168 (Aug 2020). 71

[183] Z. Tosner, T. Vosegaard, C. Kehlet, N. Khaneja, S. J. Glaser, and N. C. Nielsen, Optimal control in NMR spectroscopy: Numerical implementation in SIMPSON, J. Mag. Reson. **197**(2), 120–134 (2009). 71

[184] T. Schulte-Herbruggen, R. Marx, A. Fahmy, L. Kauffman, S. Lomonaco, N. Khaneja, and S. J. Glaser, Control aspects of quantum computing using pure and mixed states, Proc. Roy. Soc. A **370**(1976), 4651–4670 (2012). 71

[185] A. Gaikwad, K. Shende, Arvind, and K. Dorai, Implementing efficient selective quantum process tomography of superconducting quantum gates on IBM quantum experience, Sci. Rep. **12**(1), 3688 (Mar 2022). 71

[186] T. Fritz and R. Chaves, Entropic Inequalities and Marginal Problems, IEEE Trans. Inf. Theor. **59**(2), 803–817 (2013). 77

[187] X.-M. Hu, B.-H. Liu, J.-S. Chen, Y. Guo, Y.-C. Wu, Y.-F. Huang, C.-F. Li, and G.-C. Guo, Simultaneous observation of quantum contextuality and quantum nonlocality, Sci. Bull. **63**(17), 1092–1095 (2018). 77

[188] Z.-H. Liu, H.-X. Meng, Z.-P. Xu, J. Zhou, S. Ye, Q. Li, K. Sun, H.-Y. Su, A. Cabello, J.-L. Chen, J.-S. Xu, C.-F. Li, and G.-C. Guo, Experimental observation of quantum contextuality beyond Bell nonlocality, Phys. Rev. A **100**, 042118 (Oct 2019). 77

[189] T. J. Osborne and F. Verstraete, General Monogamy Inequality for Bipartite Qubit Entanglement, Phys. Rev. Lett. **96**, 220503 (Jun 2006). 77

[190] P. Kurzyński, A. Cabello, and D. Kaszlikowski, Fundamental Monogamy Relation between Contextuality and Nonlocality, Phys. Rev. Lett. **112**, 100401 (Mar 2014). 77

[191] T. Li, X. Zhang, Q. Zeng, B. Wang, and X. Zhang, Experimental simulation of monogamy relation between contextuality and nonlocality in classical light, Opt. Express **26**(9), 11959–11975 (Apr 2018). 78

[192] J. Barrett, L. Hardy, and A. Kent, No Signaling and Quantum Key Distribution, Phys. Rev. Lett. **95**, 010503 (Jun 2005). 78

[193] R. Chaves, C. Majenz, and D. Gross, Information–theoretic implications of quantum causal structures, Nat. Commun. **6**(1), 5766 (Jan 2015). 78

[194] R. Ramanathan, T. Paterek, A. Kay, P. Kurzyński, and D. Kaszlikowski, Local Realism of Macroscopic Correlations, Phys. Rev. Lett. **107**, 060405 (Aug 2011). 78

[195] A. M. Souza, A. Magalhães, J. Teles, E. R. deAzevedo, T. J. Bonagamba, I. S. Oliveira, and R. S. Sarthour, NMR analog of Bell's inequalities violation test, New J. Phys. **10**(3), 033020 (mar 2008). 78

[196] P. Kurzyński, A. Cabello, and D. Kaszlikowski, Fundamental Monogamy Relation between Contextuality and Nonlocality, Phys. Rev. Lett. **112**, 100401 (Mar 2014). 78

[197] S. L. Braunstein and C. M. Caves, Information-Theoretic Bell Inequalities, Phys. Rev. Lett. **61**, 662–665 (Aug 1988). 87

[198] R. Chaves and C. Budroni, Entropic Nonsignaling Correlations, Phys. Rev. Lett. **116**, 240501 (Jun 2016). 87, 88, 95

[199] R. Chaves, Entropic inequalities as a necessary and sufficient condition to noncontextuality and locality, Phys. Rev. A **87**, 022102 (Feb 2013). 87

[200] R. Chaves and T. Fritz, Entropic approach to local realism and noncontextuality, Phys. Rev. A **85**, 032113 (Mar 2012). 87, 88

[201] L.-Z. Cao, J.-Q. Zhao, X. Liu, Y. Yang, Y.-D. Li, X.-Q. Wang, Z.-B. Chen, and H.-X. Lu, Experimental investigation of the information entropic Bell inequality, Sci. Rep. **6**(1), 23758 (Apr 2016). 87

[202] X. Zhan, P. Kurzyński, D. Kaszlikowski, K. Wang, Z. Bian, Y. Zhang, and P. Xue, Experimental Detection of Information Deficit in a Photonic Contextuality Scenario, Phys. Rev. Lett. **119**, 220403 (Dec 2017). 87, 102

[203] D. Qu, P. Kurzyński, D. Kaszlikowski, S. Raeisi, L. Xiao, K. Wang, X. Zhan, and P. Xue, Experimental entropic test of state-independent contextuality via single photons, Phys. Rev. A **101**, 060101 (Jun 2020). 87, 102

[204] A. Cabello, S. Severini, and A. Winter, Graph-Theoretic Approach to Quantum Correlations, Phys. Rev. Lett. **112**, 040401 (Jan 2014). 89

[205] P. Kurzyński, R. Ramanathan, and D. Kaszlikowski, Entropic Test of Quantum Contextuality, Phys. Rev. Lett. **109**, 020404 (Jul 2012). 89

[206] A. Gaikwad, Arvind, and K. Dorai, True experimental reconstruction of quantum states and processes via convex optimization, Quantum Inf. Process. **20**(1), 19 (Jan 2021). 96

[207] E. Knill, I. Chuang, and R. Laflamme, Effective pure states for bulk quantum computation, Phys. Rev. A **57**, 3348–3363 (May 1998). 96

[208] A. Singh, A. Gautam, Arvind, and K. Dorai, Experimental detection of qubit-ququart pseudo-bound entanglement using three nuclear spins, Phys. Lett. A **383**(14), 1549–1554 (2019). 96

[209] D. Singh, J. Singh, K. Dorai, and Arvind, Experimental demonstration of fully contextual quantum correlations on an NMR quantum information processor, Phys. Rev. A **100**, 022109 (Aug 2019). 97, 113

[210] A. G. J. MacFarlane, J. P. Dowling, and G. J. Milburn, Quantum technology: the second quantum revolution, Philos. Trans. R. Soc. London. Ser. A **361**(1809), 1655–1674 (2003). 103

[211] R. P. Feynman, Simulating physics with computers, Int. J. Theor. Phys. **21**(6), 467–488 (Jun 1982). 103

[212] S. Lloyd, Universal Quantum Simulators, Science **273**(5278), 1073–1078 (1996). 103

[213] Y. Cao, J. Romero, J. P. Olson, M. Degroote, P. D. Johnson, M. Kieferova, I. D. Kivlichan, T. Menke, B. Peropadre, N. P. D. Sawaya, S. Sim, L. Veis, and A. Aspuru-Guzik, Quantum Chemistry in the Age of Quantum Computing, Chem. Rev. **119**(19), 10856–10915 (2019), PMID: 31469277. 103

[214] A. Aspuru-Guzik, A. D. Dutoi, P. J. Love, and M. Head-Gordon, Simulated Quantum Computation of Molecular Energies, Science **309**(5741), 1704–1707 (2005). 103

[215] J. D. Whitfield, J. Biamonte, and A. Aspuru-Guzik, Simulation of electronic structure Hamiltonians using quantum computers, Mol. Phys. **109**(5), 735–750 (2011). 104

[216] I. Kassal, J. D. Whitfield, A. Perdomo-Ortiz, M.-H. Yung, and A. Aspuru-Guzik, Simulating Chemistry Using Quantum Computers, Annu. Rev. Phys. Chem. **62**(1), 185–207 (2011), PMID: 21166541. 104

[217] N. C. Jones, J. D. Whitfield, P. L. McMahon, M.-H. Yung, R. V. Meter, A. Aspuru-Guzik, and Y. Yamamoto, Faster quantum chemistry simulation on fault-tolerant quantum computers, New J. Phys. **14**(11), 115023 (nov 2012). 104

[218] J. Preskill, Quantum Computing in the NISQ era and beyond, Quantum **2**, 79 (Aug. 2018). 104

[219] J. R. McClean, J. Romero, R. Babbush, and A. Aspuru-Guzik, The theory of variational hybrid quantum-classical algorithms, New J. Phys. **18**(2), 023023 (feb 2016). 104

[220] N. Moll, P. Barkoutsos, L. S. Bishop, J. M. Chow, A. Cross, D. J. Egger, S. Filipp, A. Fuhrer, J. M. Gambetta, M. Ganzhorn, A. Kandala, A. Mezzacapo, P. Muller, W. Riess, G. Salis, J. Smolin, I. Tavernelli, and K. Temme, Quantum optimization using variational algorithms on near-term quantum devices, Quantum Sci. Technol. **3**(3), 030503 (jun 2018). 104

[221] T. Jones, S. Endo, S. McArdle, X. Yuan, and S. C. Benjamin, Variational quantum algorithms for discovering Hamiltonian spectra, Phys. Rev. A **99**, 062304 (Jun 2019). 104

[222] D. Wang, O. Higgott, and S. Brierley, Accelerated Variational Quantum Eigensolver, Phys. Rev. Lett. **122**, 140504 (Apr 2019). 104

[223] A. Peruzzo, J. McClean, P. Shadbolt, M.-H. Yung, X.-Q. Zhou, P. J. Love, A. Aspuru-Guzik, and J. L. O'Brien, A variational eigenvalue solver on a photonic quantum processor, Nat. Commun. **5**(1), 4213 (Jul 2014). 104

[224] R. Santagati, J. Wang, A. A. Gentile, S. Paesani, N. Wiebe, J. R. McClean, S. Morley-Short, P. J. Shadbolt, D. Bonneau, J. W. Silverstone, D. P. Tew, X. Zhou, J. L. O'Brien, and M. G. Thompson, Witnessing eigenstates for quantum simulation of Hamiltonian spectra, Sci. Adv. **4**(1), eaap9646 (2018). 104

[225] J. I. Colless, V. V. Ramasesh, D. Dahlen, M. S. Blok, M. E. Kimchi-Schwartz, J. R. McClean, J. Carter, W. A. de Jong, and I. Siddiqi, Computation of Molecular Spectra on a Quantum Processor with an Error-Resilient Algorithm, Phys. Rev. X **8**, 011021 (Feb 2018). 104, 107, 108, 121

[226] O. Higgott, D. Wang, and S. Brierley, Variational Quantum Computation of Excited States, Quantum **3**, 156 (July 2019). 104, 106

[227] C. Hempel, C. Maier, J. Romero, J. McClean, T. Monz, H. Shen, P. Jurcevic, B. P. Lanyon, P. Love, R. Babbush, A. Aspuru-Guzik, R. Blatt, and C. F. Roos, Quantum Chemistry Calculations on a Trapped-Ion Quantum Simulator, Phys. Rev. X **8**, 031022 (Jul 2018). 104, 109, 119

[228] P. J. J. O'Malley, R. Babbush, I. D. Kivlichan, J. Romero, J. R. McClean, R. Barends, J. Kelly, P. Roushan, A. Tranter, N. Ding, B. Campbell, Y. Chen, Z. Chen, B. Chiaro, A. Dunsworth, A. G. Fowler, E. Jeffrey, E. Lucero, A. Megrant, J. Y. Mutus, M. Neeley, C. Neill, C. Quintana, D. Sank, A. Vainsencher, J. Wenner, T. C. White, P. V. Coveney, P. J. Love, H. Neven, A. Aspuru-Guzik, and J. M. Martinis, Scalable Quantum Simulation of Molecular Energies, Phys. Rev. X **6**, 031007 (Jul 2016). 104, 107, 108

[229] R. Xia and S. Kais, Qubit coupled cluster singles and doubles variational quantum eigensolver ansatz for electronic structure calculations, Quantum Sci. Technol. **6**(1), 015001 (oct 2020). 104

[230] J. T. Seeley, M. J. Richard, and P. J. Love, The Bravyi-Kitaev transformation for quantum computation of electronic structure, J. Chem. Phys. **137**(22), 224109 (2012). 108

[231] M. Ganzhorn, D. Egger, P. Barkoutsos, P. Ollitrault, G. Salis, N. Moll, M. Roth, A. Fuhrer, P. Mueller, S. Woerner, I. Tavernelli, and S. Filipp, Gate-Efficient Simulation of Molecular Eigenstates on a Quantum Computer, Phys. Rev. Applied **11**, 044092 (Apr 2019). 108